12-2006

Severe Plastic Deformation using Friction Stir Processing, and the Characterization of Microstructure and Mechanical Behavior using Neutron Diffraction

Wanchuck Woo
University of Tennessee - Knoxville

To the Graduate Council:

I am submitting herewith a dissertation written by Wanchuck Woo entitled "*Severe Plastic Deformation using Friction Stir Processing, and the Characterization of Microstructure and Mechanical Behavior using Neutron Diffraction*." I have examined the final electronic copy of this dissertation for form and content and recommend that it be accepted in partial fulfillment of the requirements for the degree of Doctor of Philosophy, with a major in Materials Science and Engineering.

Hahn Choo, Major Professor

We have read this dissertation and recommend its acceptance:

Peter K. Liaw, George M. Pharr, David C. Joy, Camden R. Hubbard

Accepted for the Council:

Carolyn R. Hodges

Vice Provost and Dean of the Graduate School

(Original signatures are on file with official student records.)

To the Graduate Council:

I am submitting herewith a dissertation written by Wanchuck Woo entitled "*Severe Plastic Deformation using Friction Stir Processing, and the Characterization of Microstructure and Mechanical Behavior using Neutron Diffraction*". I have examined the final electronic copy of this dissertation for form and content and recommend that it be accepted in partial fulfillment of the requirements for the degree of Doctor of Philosophy, with a major in Materials Science and Engineering.

Hahn Choo
Major Professor

We have read this dissertation and recommend its acceptance:

Peter K. Liaw

George M. Pharr

David C. Joy

Camden R. Hubbard

Accepted for the Council:

Anne Mayhew

Vice Chancellor and Dean of
Graduate Studies

(Original signatures are on file with official student records.)

Severe Plastic Deformation using Friction Stir Processing, and the Characterization of Microstructure and Mechanical Behavior using Neutron Diffraction

A Dissertation Presented for the

Doctor of Philosophy Degree

The University of Tennessee, Knoxville

Wanchuck Woo

December 2006

Dedication

I would like to dedicate this Doctoral dissertation to my wife, Yelia Kim, whose unending support and encouragement during the course of my graduate study. There is no doubt in my mind that without her heartful support I could not have completed this process. I also want to dedicate this work to my parents for their continuous love and support throughout my study. Dedication is also to my son, Hyunseo Woo, making me more thankful to God.

Acknowledgements

I appreciate many people for their guidance and help during my Ph.D. study. My advisors Dr. Hahn Choo and Dr. Peter K. Liaw have been always kindly helping me with my research throughout these years, creating environments for me to extend my potentials, and providing all kinds of opportunities for me to develop my academic capabilities and interpersonal relationship. Prof. George M. Pharr, Prof. David C. Joy, and Dr. Camden R. Hubbard, who kindly agreed to be on my committee, have been giving all kinds of help to finish my Ph.D. study. Dr. Donald W. Brown, Dr. Zhili Feng, Dr. Xun-Li Wang, Dr. Stan A. David, Dr. Mark A. M. Bourke have been giving me precious instructions on my research, providing all the necessary materials and experiments for my research project and giving suggestions on my paper writings. I'm thankful to Dr. Philip J. Withers, Dr. Tom Holden, Dr. Ronald Rogge, Dr. Mark Daymond, Dr. Sean Agnew, Dr. Yandong Wang, Dr. Mike Santella, and Dr. Aaron Krawitz for their kind and valuable suggestions/comments in this study.

In the process of my study, many people helped me on many aspects that are indispensable. I'm thankful to Dr. Bjorn Clausen, Dr. Sven Vogel, Dr. Mike Prime, Dr. Tarik A Saleh, Mr. Thomas A. Sisneros for the neutron experiments at Los Alamos National Laboratory; Dr. Oleg Barabash, Mr. A. Frederick, Dr. Ke An, Mr. William Bailey for the experiments at Oak Ridge National Laboratory; Mr. Scott M. Packer and Mr. Babb, Jonadan at the Megastir company; and Mr. John R. Dunlap, Mr. Gregory L. Jones, Mr. Frank Holiway, and Mr. Douglas Fielden at the University of Tennessee for their help in a timely manner. A great friendship made it possible to study and work

through my research projects. Many thanks to Dr. Ja-il Jang, Mr. Michael Benson, Dr. Sang-hoon Sim, Mr. Tim Wilson, Mr. Sang-jun Shon, Mr. Kaixiang Tao, Mr. Jin-woo Jeon, Mr. Ji-hoon Kim, Mr. Seung-ik Jun, Mr. Young-rong Choi, Mr. James Wall, Mr. Ben Lovell, Mrs. Elena Garlea, Ms. Zhenzhen Yu, Mr. Soo-yeol Lee, and Mr. E-Wen Huang for their kind help.

Grateful acknowledgements are due to the financial support for this research by the NSF International Materials Institutes (IMI) Program under contract DMR-0231320. This work has benefited from the use of the Los Alamos Neutron Science Center at the Los Alamos National Laboratory. This facility is funded by the US Department of Energy under Contract W-7405-ENG-36. The research was also sponsored by the Assistant Secretary for Energy Efficiency and Renewable Energy, Office of FreedomCAR and Vehicle Technologies, as part of the High Temperature Materials Laboratory User Program, Oak Ridge National Laboratory, managed by UT-Battelle, LLC, for the U.S. Department of Energy under contract number DE-AC05-00OR22725.

Abstract

Friction-stir welding (FSW) is a solid-state joining process, which utilizes a cylindrical rotating tool consisting of a concentric threaded tool pin and tool shoulder. The strong metallurgical bonding during the FSW is accomplished through: (1) the severe plastic deformation caused by the rotation of the tool pin that plunges into the material and travels along the joining line; and (2) the frictional heat generated mainly from the pressing tool shoulder. Recently, a number of variations of the FSW have been applied to modify the microstructure, for example, grain refinements and homogenization of precipitate particles, namely friction-stir processing (FSP). Applications of the FSP/FSW are widespread for the transportation industries. The microstructure and mechanical behavior of light-weight materials subjected to the FSW/FSP are being studied extensively. However, separating the effect of the frictional heat and severe plastic deformation on the residual stress and texture has been a standing problem for the fundamental understanding of FSW/FSP. The fundamental issues are: i) the heat- and plastic-deformation-induced internal stresses that may be detrimental to the integrity and performance of components; ii) the frictional heating that causes a microstructural softening due to the dissolution or growth of the precipitates in precipitation-hardenable Al alloys during the process; and iii) the crystallographic texture can be significantly altered from the original texture, which could affect the physical and mechanical properties. The understanding of the influences of the de-convoluted sources (e.g. frictional heat, severe plastic deformation, or their combination) on the residual stress, microstructural softening, and texture variations during FSW can be used for a physics-

based optimization of the processing parameters and new tool designs. Furthermore, the analyses and characterization of the natural aging behavior and the aging kinetics can be practically applied to the predictions of mechanical behavior and material selection for the FSW/FSP. Finally, the experimental results can be useful to develop more accurate computational simulations.

TABLE OF CONTENTS

List of Tables

List of Figures

Chapter I Introduction

1.1. Friction-stir welding (FSW)

Friction-stir welding (FSW) is a solid-state joining process, which utilizes a cylindrical rotating tool consisting of a concentric threaded tool pin and tool shoulder, Fig. 1.1. FSW is known to produce a strong metallurgical bond through: (1) the severe plastic deformation caused by the rotation of the tool pin that plunges into the material and travels along the joining line and; (2) the frictional heat generated mainly from the pressing tool shoulder, Fig. 1.2, [1,2]. FSW has many advantages over the traditional fusion-welding processes, which include nearly defect-free joints due to the absence of solidification/liquid cracking; fine grain structures associated with severe plastic deformation, and minimized angular distortion due to the relatively uniform through-thickness temperature distributions [3,4].

The FSW technique has generated tremendous interests in industries because of: (1) its simplified fabricating procedure with high-integrity products without need for the joint preparation, filler metal, or protection from the atmosphere and; (2) minimized health hazards, such as fume, spatter, and radiation. Current and potential applications of FSW are widespread for the transportation industries including engine support frames, liquefied-petroleum-gas storage vessels, and cryogenic tanks for the space launch system [5,6].

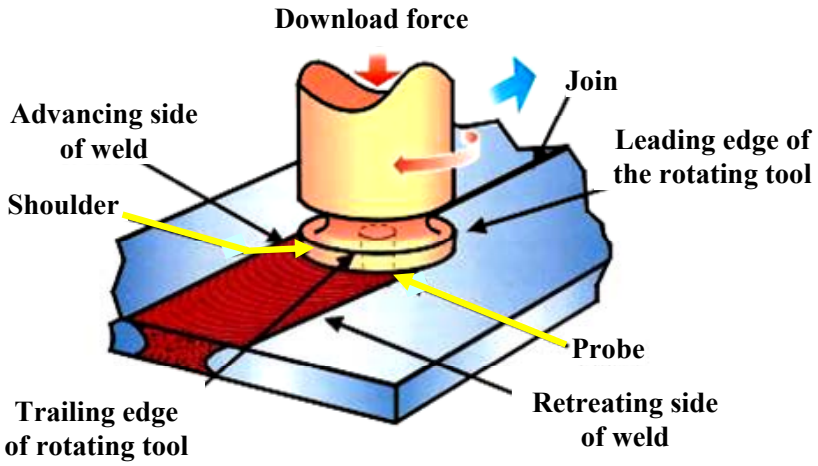

Fig. 1-1. Schematic of the friction-stir welding (FSW).

(Thomas WM *et al.*, GB Patent Application No. 9125978.8; Dec 1991.[1])

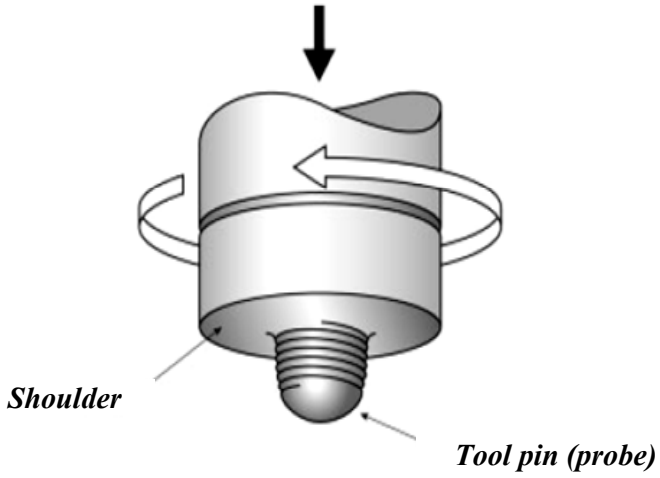

Fig. 1-2. Schematic of a cylindrical threaded pin used in Friction-stir welding (FSW).

(Thomas WM *et al.*, Mater Design 1997;18;269 [5])

1.2. Friction-stir processing (FSP)

Friction-stir processing (FSP) is a newly developed technique, which is a variation of the FSW method. The FSP method has been applied to microstructural modifications for enhanced mechanical properties via localized grain refinement, Fig. 1.3, [7]. The benefits of FSP also include homogenization of precipitates in various aluminum alloys and composites [8-11]. More recent applications of the FSP include the processing of the microstructure amenable to the high-strain-rate superplasticity. Ma *et al*. reported the superplasticity in aluminum alloys subjected to the grain-size refinements via FSP [9]. Furthermore, Su *et al.* reported that the FSP technique could be applied to produce bulk ultrafine-grained alloys [12,13], based on the principles of severe plastic deformation techniques [14].

1.3. Neutron diffraction characterization

The deep penetration capability of neutrons into most metallic materials makes neutron diffraction a unique and powerful tool in characterizing their microstructures and properties [15-17]. In particular, spatially-resolved neutron-diffraction studies can be used to determine stress , texture, and phase transformation [18-21]. The determination of residual strains using neutron diffraction is based on the volume-averaged measurement of interplanar spacings (*d*-spacings) in various crystallographic and geometric orientations, Fig. 1.4, [22,23]. In a neutron diffraction experiment, one measures the *d*-spacings of a crystalline material based on the Bragg's law.

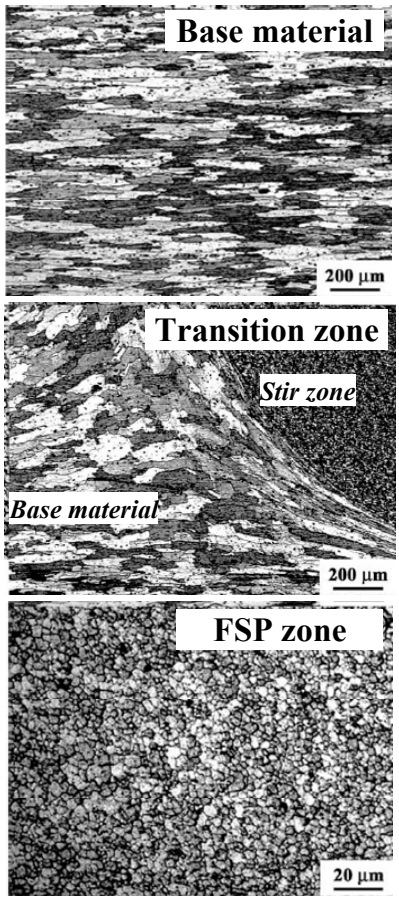

Fig. 1-3. Optical micrographs showing grain structures of commercial 7075 Al rolled plates subjected to the FSP. The results show grain refinements from about 150 μm to 4-9 μm via FSP.

(Mishra RS *et al*., Scripta Mater 2000;42;163 [7])

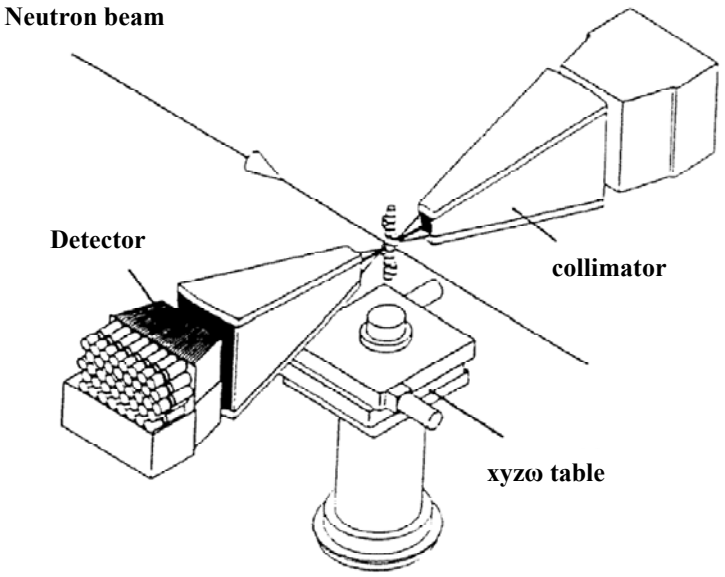

Fig. 1-4. A spallation source neutron diffraction instrument with the two detector systems including two focusing collimators

(Albertini G *et al*., Meas Sci Technol 1999;10;R56 [23])

The lattice strain (ε) is defined as the change of the *d*-spacing from its stress-free state [16]:

$$\varepsilon = (d - d_o) / d_o \tag{1}$$

where *d* is the *d*-spacing of diffracted plane under stress and temperature, and d_o is the stress-free *d*-spacing. Thus, the lattice strain can be measured using the expansion or contraction of the lattice plane of a material. The residual strain data are converted to the principal residual stresses (i.e., σ_x, σ_y, and σ_z) using Hooke's law [23]:

$$\sigma_{ii} = \frac{E}{1+\nu}\left[\varepsilon_{ii} + \frac{\nu}{1-2\nu}\left(\varepsilon_{xx} + \varepsilon_{yy} + \varepsilon_{zz}\right)\right] \tag{2}$$

where *i=x, y, z* corresponding to longitudinal, transverse, and normal direction, respectively; E, Young's modulus (GPa); *v*, Poissons ratio. Henceforth, LD, TD, and ND denote longitudinal, transverse, and normal directions.

Furthermore, neutron-diffraction measurements can provide insights to the texture variations. The intensity of a diffraction peak is related to the texture. The integrated intensity (I_τ) can be used for the texture studies [24]:

$$I_\tau \propto \left(\frac{\lambda^4 Z_\tau F(\tau)^2}{\sin^2\theta}\right)\left(\frac{N_s}{V_{cell}}\right) \tag{3}$$

where λ is the wavelength, Z_τ is the multiplicity of the reflection, $F(\tau)$ is the structure factor, 2θ is the scattering angle, N_s is the number of the scattering unit cells satisfying Bragg's law, and V_{cell} is the volume of scattering unit cell. Thus, the concept of integrated intensity can be used to analyze the preferred orientation and details will be described in Section 6.2.

1.4. Motivation and outline of the research

Friction-stir welding (FSW) of aluminum alloys has been used in practice to produce a strong and sound metallurgical joint. However, the heat and plastic deformation involved in the FSW can induce significant changes in residual stresses that may be detrimental to the integrity and performance of components [25-34]. For example, Reynolds *et al.* reported maximum longitudinal residual stresses approaching 100% of the yield strength (300 MPa) of the base material in a 304L stainless steel FSW [34]. Although the heat input is considered as the main source of internal stresses in a FSW, direct experimental evidence supporting this is not available in the literature to date.

Furthermore, the significant changes in the microstructure caused by the frictional heat and severe plastic deformation during FSW could also be detrimental to the integrity and performance of components [35-39]. The microstructural softening due to the dissolution and/or growth of strengthening precipitates in FSP-affected regions is a significant and a specific problem for precipitation-hardenable Al alloys. The reduction of precipitates deteriorates the tensile strength of the FSP-affected region [40-45]. Sato *et al*. showed the dissolution and growth sequences of precipitates as a function of temperature in 6063 Al alloys subjected to FSW [41-43]. The reduction of precipitates significantly deteriorates the tensile strength of the FSP-affected region and the mechanical properties can be significantly altered during the post-FSP natural aging [44,45]. Therefore, the effects of frictional heating and severe plastic deformation during FSP on the microstructural softening, the post-FSP natural aging, its long term kinetics,

and their influence on the residual strain profiles of a 6061-T6 Al alloy are important fundamental issues.

Finally, during the FSW the crystallographic texture can be significantly altered from the original rolling texture in aluminum-alloy [46-50] or magnesium-alloy [51,52] plates, which can significantly affect the physical and mechanical properties. Fonda *et al.* showed, based on the crystallographic texture analysis of a Al 2519 FSW, that the texture variation is significant across the boundary between the thermo-mechanically affected zone (TMAZ) and the heat-affected zone (HAZ) due to macroscopic rigid-body rotations of the grains around the stirring pin of the FSW tool [46,47]. Park *et al.* reported that the texture variation can strongly affect the tensile properties in the FSW AZ61 magnesium alloy [51,52]. In the current literature, severe plastic deformation is considered as the main source of texture alteration during the FSW, Fig. 1.5. However, direct experimental evidence is not available to date.

Thus, objectives of this study are: (i) separate possible sources (heat and plastic deformation) that develop internal strains, (ii) understand the effects of the stirring pin and the tool shoulder on the microstructural softening during the FSP and the post-FSP natural aging, (iii) investigate the asymmetric distribution of residual stress and the relationship between the residual stress and the angular distortion, and (iv) examine of the texture variation in the characteristic regions and the main cause of the changes in the initial recrystallized rolling texture of the plate summarized in Fig. 1.6. These fundamental issues/tasks were addressed using various experimental tools including the neutron diffraction technique, Figs. 1.5 and 1.6. The experimental results can be

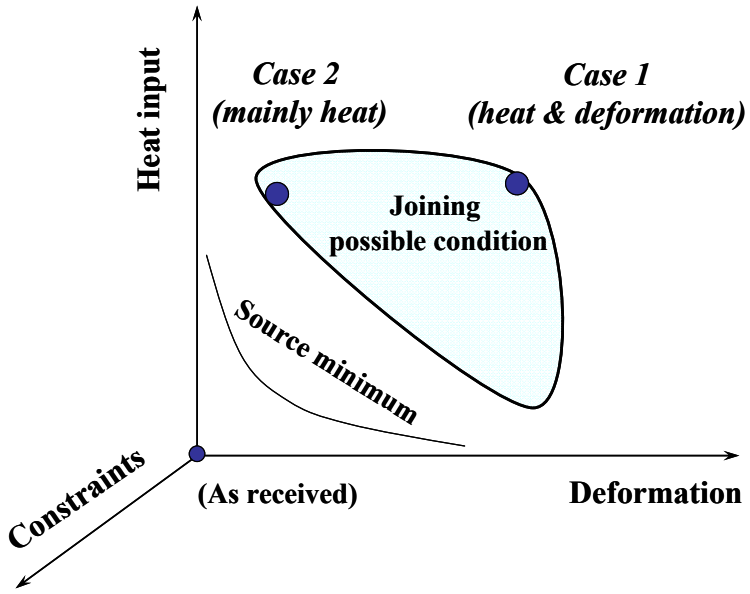

Fig. 1-5. Proposed potential sources of residual stress and sample preparation

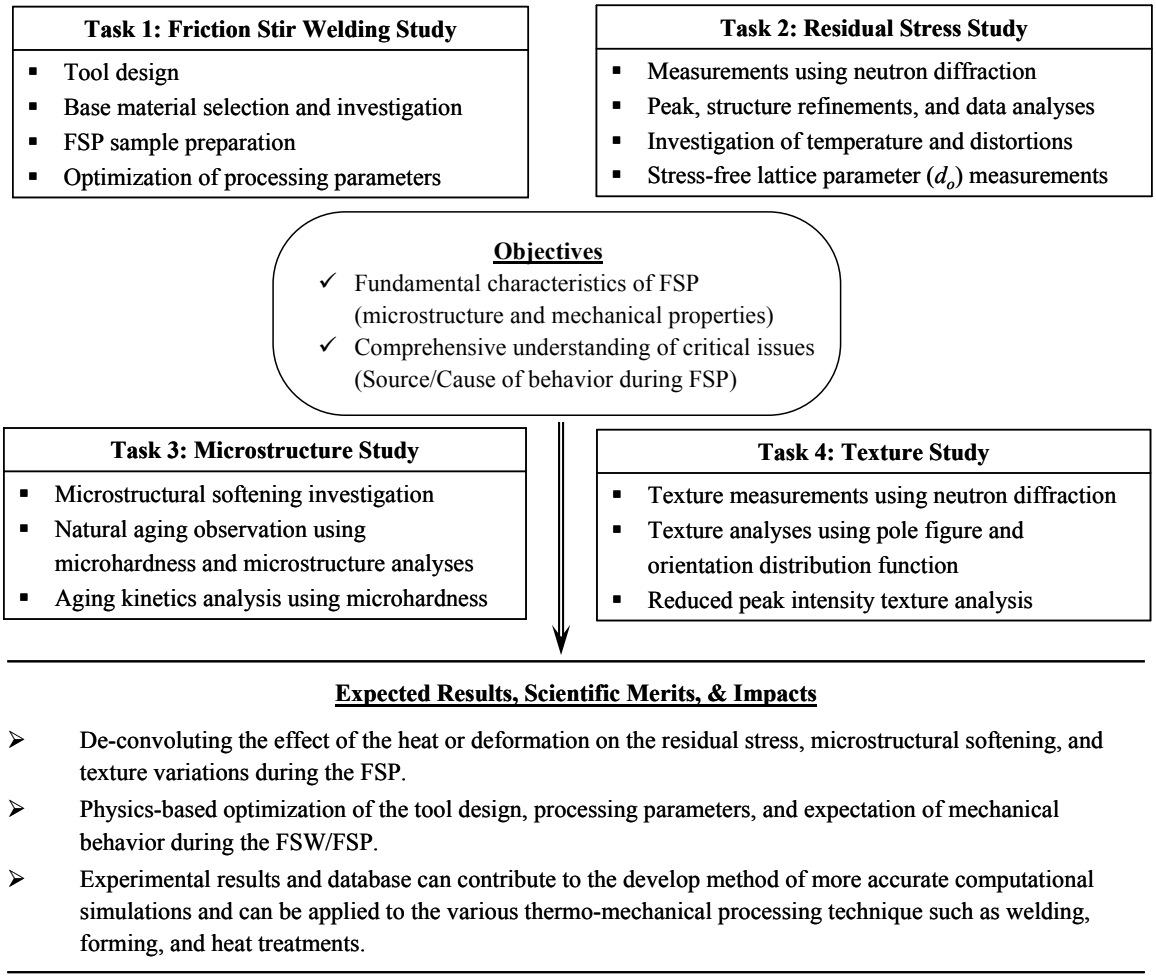

Figure 1.6. Objectives, tasks, and expected results of the current dissertation.

useful in developing more accurate computational simulations [53-59], leading to a physics-based optimization of the processing parameters and tool design [60-65].

Chapter II Literature review

2.1 Overview of friction-stir welding (FSW)

2.1.1. Background and methodology

The definition of friction-stir welding (FSW) is described as "*a solid state joining technique, in which a severe plastic deformation is used to plasticize in a confined region, which results in a strong metallurgical bond that creates intimate contact between materials on either side of the joint line* [1]." In detail, the welding is accomplished using inserting a threaded *pin*, also called as a *probe* or a *nib*, into the surface of plates which are to be butt-welded. The pin, which is typically slightly shorter than the thickness of the plate and its diameter is approximately the thickness of the work piece, is mounted on a shoulder that has a diameter three times that of the pin. The stirring pin and tool shoulder are pressed against the plates, rotated at hundreds revolutions per minute, and travels along the intended joining line [2-5].

In 1991, the Welding Institute (TWI), Cambridge, UK developed a novel welding method and called the process as friction-stir welding (FSW). The major researcher, Wayne M. Thomas enrolled the International Patent No. PCT/GB92/02203), US Patent No. 5,460,317, and GB Patent No. 9125978.8 [1]. Previously a solid-state process, friction welding, was developed and used from the 1950s; however, the method was usually restricted to a special condition of welding. The FSW technique, on the other hand, is a totally different joining process and is considered as one of the most advanced technologies in welding community [2,3]. The most important advantage of the FSW is

the ability to produces nearly defect-free welds at lower cost than conventional fusion welds in aluminum alloys [5]. During FSW, the maximum temperature produced by the tool is approximately 80% of the melting temperature of aluminum, which causes the base material to soften along the welding bead. The softened plasticized material is also forged by the pressing tool shoulder [3]. This benefits the ability to join materials such as 2xxx and 7xxx aluminum alloys, which are difficult to fusion weld. Furthermore, there are a number of advantages compared to the conventional fusion welding: (1) eliminates the liquidation or solidification cracking problems during the solidification of the welded metal that may occur during fusion welding,; (2) no loss of alloying elements and unchanged alloy composition; and (3) grain refinement resulting in an excellent mechanical properties such as enhanced fatigue, tensile, and bend properties. It was reported that fatigue resistance improved twice compared to that of fusion weld due to the minimized ranges of heat damage and angular distortion, Fig. 2.1 [2,3]. However, several disadvantages were also reported for the FSW technique such as; (1) limitation of the weld thickness based on the mechanical properties of the tool, (e.g., up to 50 mm for Al alloys, up to 25 mm for Ti alloys and Steels), (2) asymmetric microstructure between the advancing side and retreating side due to the relative direction of the rotation and travel of the tool, (3) difficulty in the plate fitting to minimize the gap variation within 10 % of the material thickness to prevent mismatch of the plates, (4) the deterioration of properties as a result of welding in the softened region and residual stress in the TMAZ/HAZ, and (5) the mechanism of the process is not fully understood [5,6].

FSW has been extensively used to join various aluminum alloys because solid state process does not melt aluminum alloys. The research and development efforts on

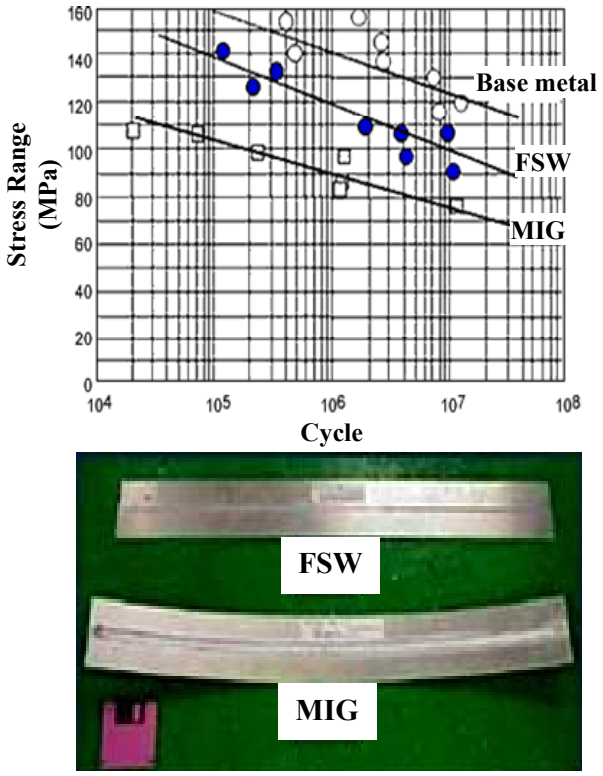

Fig. 2.1. Improved fatigue resistance and low deformation of the FSW compared to a Metal-inert-gas (MIG) arc fusion weld.

(Maddox SJ. Inter J Fatigue, 2003;25:1357 [2])

FSW has been mainly focused on Al alloy series 2000, 6000, and 7000, which are difficult to weld by the traditional fusion welding [2,5]. In particular, the microsturctural softening due to the dissolution of the strengthening precipitates of heat-treatable aluminum alloys subjected to the FSW process have been investigated, for example, 6061-T5/T6 (K N. Krishnan *et al*., 1997) [66,67], 7075-T651 (C. G. Rhodes e*t al*., 1997) [68,69], 2024-T6 (Y. Li *et al*., 1999) [70], 6063-T5 (Y. S. Sato et al., 1999) [42,43], 2195-T8 (J. Corral et al., 2000) [71], 7475- T76 (I. Charit *et al*., 2002) [44], 2024-T3 (M. A. Sutton *et al*., 2003) [72,73]. The microstructural softening can also be a problem in the FSW joints of non-heat-treatable alloys (strain-hardened alloys) due to the reduced dislocation density in the FSW-affected zone (stir zone and heat-affected zone). The examples of the FSW in the non-heat treatable aluminum alloys include 1100 (H. J. Liu et al., 2003) [74,75] and 1050 (Y. S. Sato et al., 2004) [76].

During FSW, the rotating (stirring) tool with a profiled pin penetrates the base material, causes plastic deformation and heating while the tool shoulder generates additional frictional heat. Together they make the base material soft while travels along the desired joint line. The rotating tool should be a harder material than the welded material. The plates to be joined are necessary constrained with pressure using clamps along the sides of the plates [1-3]. In detail, Fig. 2.2(a) describes the tool rotating at a high speed and positioned above the intended welding line of the plates. Fig. 2.2(b) shows the pin plunging into the welding line and generating frictional heat from the cylindrical shoulder surface and a small region of material underneath the tool pin (i.e., *initial tipping period*). Then, the rotating cylindrical shoulder presses the plate material along the direction normal to the plate which supplies most of the frictional heat.

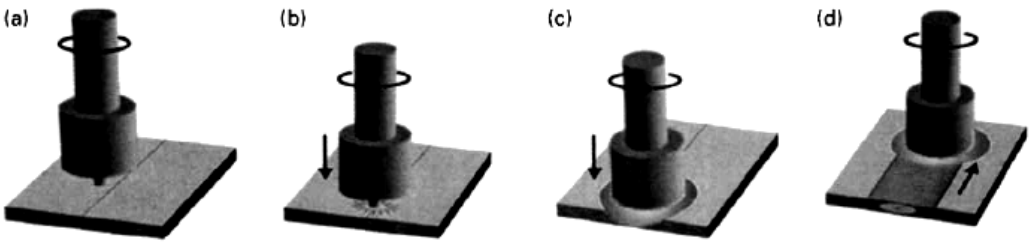

Fig. 2.2. Schematic diagram of the procedure of the FSW

(Mahoney MW *et al*., Mater Trans A 1998;29A;1955 [3])

The pressure supplies highly plasticized material and avoid overflowing the fluid material out of the welding pool (i.e., *transient plunging period*), Fig. 2.2(c). At this moment, the thermally softened region due to the frictional heat grows wider at the top surface, which is in direct contact with the shoulder, while inside of the welding pool, the plasticized materials are constantly produced in contact with the surface of the tool pin and pressing shoulder around the traveling tool (i.e., *steady state extrusion period*), Fig. 2.2(d). The amount of frictional heat produced by the shoulder can vary depends on the welding parameters (e.g., tool design, pressure, and rotation/translation speeds).

2.1.2. Applications and critical issues

The TWI has developed a number of FSW welding processes applicable to many kinds of the aluminum alloys, such as 2xxx, 5xxx, 6xxx, 7xxx, and 8xxx alloys, and reported high-integrity welds with good yield strengths [63-65]. Recently, they showed a possibility of welding up to 100-mm thick 6082 aluminum-alloy plate using two-pass FSW technique, Fig. 2.3, [77]. The speed of FSW for aluminum alloys is about 5 mm/s, which is three times faster than normal fusion welding such as metal inert gas (MIG) welding, with lower heat input without requiring shielding gases and costly filler materials. Thus, industry is currently using the FSW technology for joining aluminum alloys for many structural applications. The industrial applications range from small-scale components to large panels. Examples include cooling elements, electric engines, high speed rail ways, wagons, offshore structures, external fuel tanks of rockets, and bridge constructions. In particular, FSW has been widely applied in the transportation industries. Examples include engine support frames for the automotive industry; bulk carrier tanks

Fig. 2.3. Transverse section through double-sided friction stir weld in 75-mm thick 6082-aluminum alloy

(Sanderson A *et al*., Fusion Eng Design 2000;49:77 [77])

for the transportation industry; hulls, decks, and internal structures for high speed ferries; and liquefied-petroleum-gas storage vessels for the shipbuilding industry, Fig. 2.4. [78].

Meantime, academic and R&D communities focused on the unsolved problems of the FSW technique. One of the critical issues of the FSW is the lack of fundamental correlation between the processing, microstructure, and mechanical properties of the FSW products compared to the well-established theories of conventional welding/joining technologies. For example, for the FSW, issues related to the asymmetric microstructures, mechanical properties deterioration, the residual stress characteristics, softening of the welds, and texture development remain as critical research topics [70-75]. Initially the temperature distribution during the FSW was extensively investigated and its effect on the microstructural characteristics and mechanical properties has been studied using thermo-mechanical modeling of different types of aluminum alloy [53-59]. Secondly, the measurements and predictions of the mechanical behavior of materials after the FSW were performed. For example, influences of the residual stresses and texture on the mechanical properties were examined using neutron, synchrotron, and x-ray diffraction [61-63]. Webster *et al*. reported the mapping of the residual strain in combination with the finite element modeling (FEM), Fig. 2.5, [31].

Another critical issue is the broadening of the application of FSW to other kinds of material (i.e., not only to aluminum alloys). The potential immediate applications of the FSW process includes magnesium, magnesium alloys [51,52], copper, copper alloys [65], lead, titanium [79], zinc, and steel [6]. According to the report of Reynolds *et al.* [6], the microstructure of the hot-rolled steel such as DH36, Fig. 2.6(a), can contain “swirl zone”, known as a defect such as wormholes or tunnels due to the complex material flow

Fig. 2.4. Industrial applications; a high-speed train and airplane.

(Thomas WM. Advanced Eng Mat 2003;5:485 [78], courtesy of Hitachi Co., Ltd and Airbus Bremen Co., Ltd)

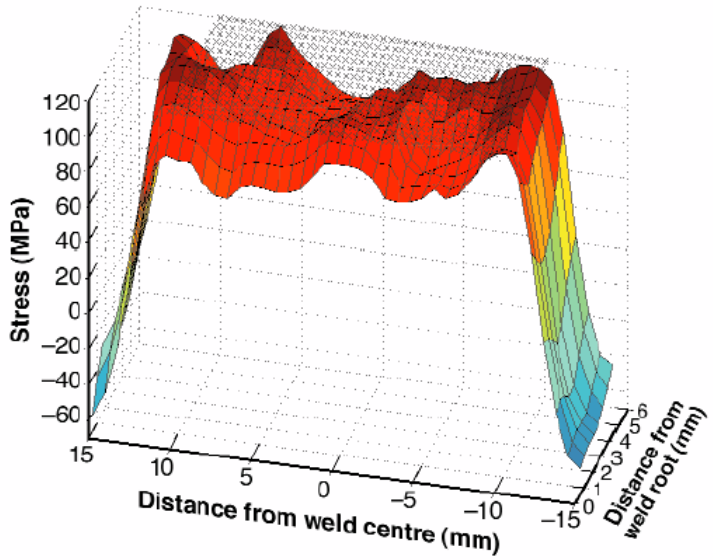

Fig. 2.5. Modeling of the longitudinal residual stress distribution of a FSW.

(Webster PJ *et al*., J strain analysis 2001;36:61 [31])

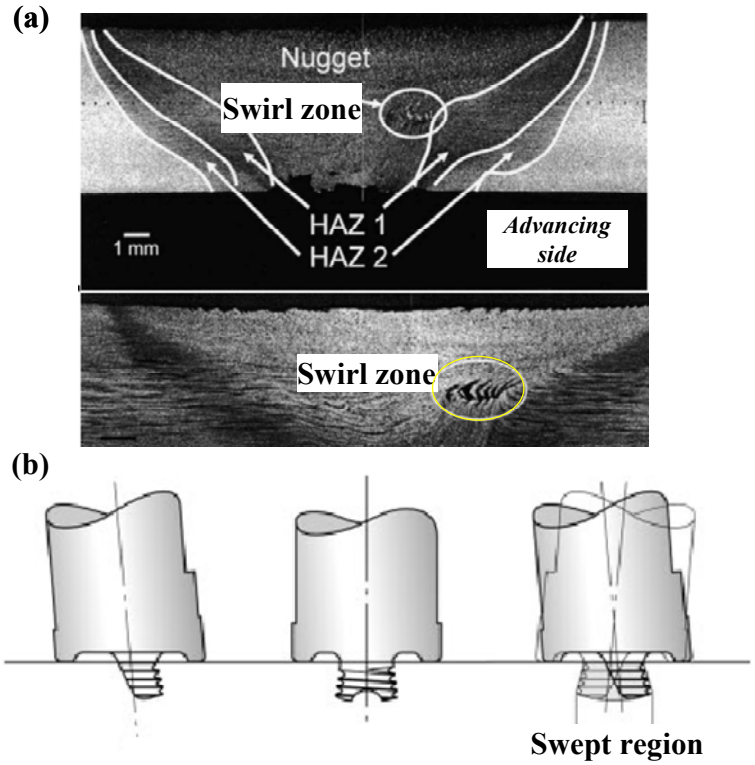

Fig. 2.6. (a) Microstructure of FSW DH36 and (b) basic principle of the skew-stir pin

(Reynolds AP *et al*., J Sci Tech Weld Join 2003;8:455 [6] and Thomas WM. Advanced Eng Mat 2003;5:485 [78])

and phase transformations in carbon steel welds, unlike aluminum alloys. Thomas *et al.*, at TWI, reported newly-developed tools, named skew-stir probe, to solve the microstructural issues in the ferrous alloys using the uniform flow of materials during the FSW, Fig. 2.6(b) [78].

2.1.3. Microstructure and mechanical properties

The microstructural evolution [68] and the mechanical properties of the FSW welds [75] will be briefly summarized here. Figure 2.7 shows a typical cross-section of a FSW 2024-T351 joint, which exhibits the recrystallized zone (DXZ), thermo-mechanically affected zone (TMAZ), and heat-affected zone (HAZ). The microstructural softening within the TMAZ and HAZ is a problem [42,43] similar to that in a fusion weld [25]. In metal inert gas (MIG) fusion welding, the microstructure of the weld has dendrite structures in the fusion zone, large recrystallized grains in the HAZ, and typical grains in the base material, Fig. 2.8. On the other hand, Fig. 2.9 shows the microstructure of a FSW showing DXZ, TMAZ, and the base material. It shows very fine crystallized grains in the DXZ, partially recrystallized/plastically deformed grains in the TMAZ, and the initial elongated grains in the base material [25,76].

Figure 2.10 shows the microstructural evolution of 6063 aluminum alloys during/after the FSW [42]. The 6063 base metal has Mg_2Si precipitates, which show two distinctly different morphologies categorized as the fine needle-shape precipitate and rod-shape precipitate. The fine needle precipitate is known as the main strengthening precipitate and coherent with the matrix, while rod-shape shape precipitates have a low coherency with the matrix. The fine needle precipitates were observed in the Al

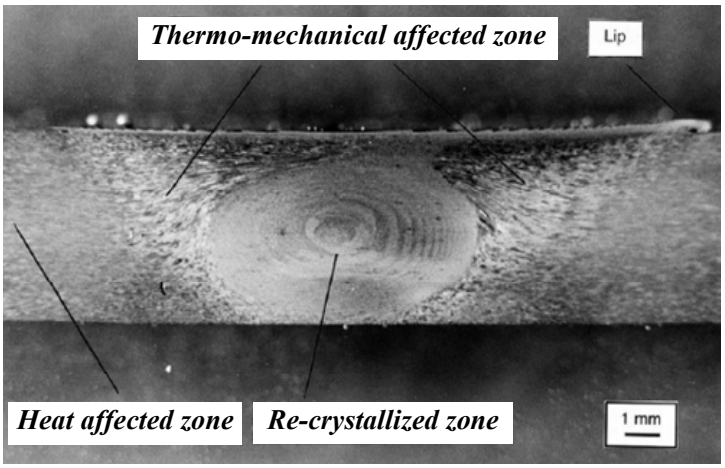

Fig. 2.7. Typical transverse cross section of an as-welded FSW 2024-T351 joint.

(Bussu. G *et al*., Inter J Fatigue, 2003;25;77 [26])

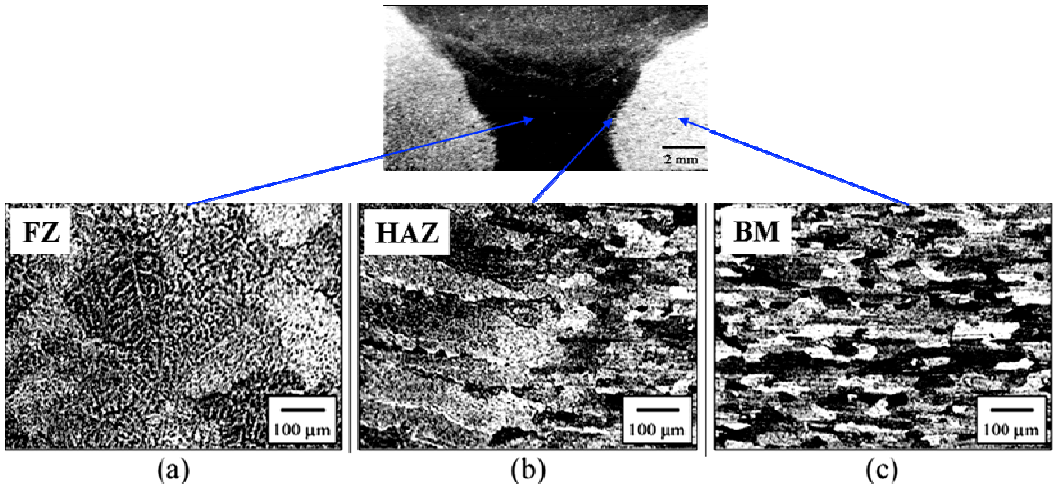

Fig. 2.8. Cross-section of a fusion weld and microstructure in three regions:

(a) fusion zone (FZ), (b) heat-affected zone (HAZ), and (c) base material (BM) of MIG AA5083.

(Thomas WM *et al*., Adv Eng Mat 2003;5:485 [25])

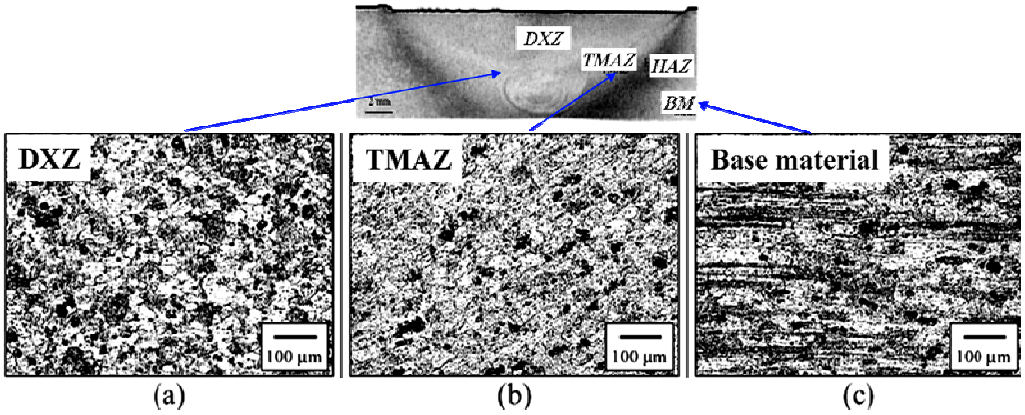

Fig. 2.9. Cross-section of a FSW and microstructure in three regions:

(a) Recrystallized zone (DXZ), (b) thermo-mechanical affected zone (TMAZ) and (c) base material of FSW AA5083.

(Thomas WM *et al*., Adv Eng Mat 2003;5:485 [25])

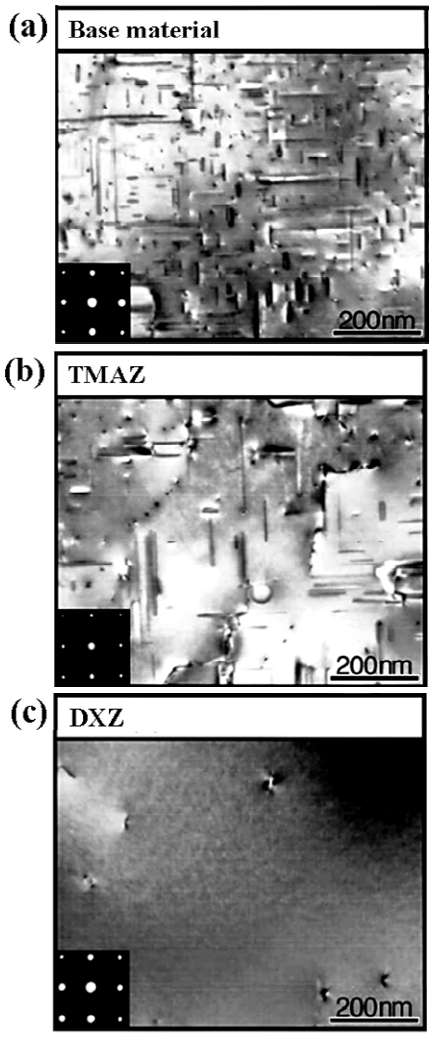

Fig. 2.10. TEM micrographs of an Al 6061 FSW: (a) base material; (b) TMAZ; and (c) DXZ.

(Sato YS *et al*., Metall Mater Trans A 1999;30;2429.[42])

matrix of the base material and there are several rod-shape precipitates in the base material (BM), Fig. 2.10(a). However, the precipitates disappeared in the FSW stir zone (DXZ), Fig. 2.10(c). This indicates that the temperature of the FSW-effected zone reached the solvus temperature of the precipitates. As a result the DXZ is mainly composed of the dynamic recrystallized grain structure. The transition region had a high density of the coarser rod-shape precipitates, Fig. 2.10(b), due to the slightly lower processing temperature [42].

Figure 2.11 shows a typical hardness profile across the FSW plate. The minimum hardness location was located at about 6 mm from the centerline suggesting that the DXZ was significantly harder than the TMAZ. The highest hardness was found about 22 mm from the centerline, and a small hardness decrease occurred at about 28 mm from the centerline [80]. Hardness profiles show that a distinct soft region is located at the boundary between the TMAZ and HAZ. Figure 2.12 shows the variation in the tensile properties of the joints with different revolutionary pitch, which is the ratio of the welding speed to rotation speed [75]. The 0.2% proof strength increases with the revolutionary pitch increase (decreased heat input), since the degree of softening decreases. Thus, there is an optimum revolutionary pitch in terms of the tensile strength under the different welding conditions.

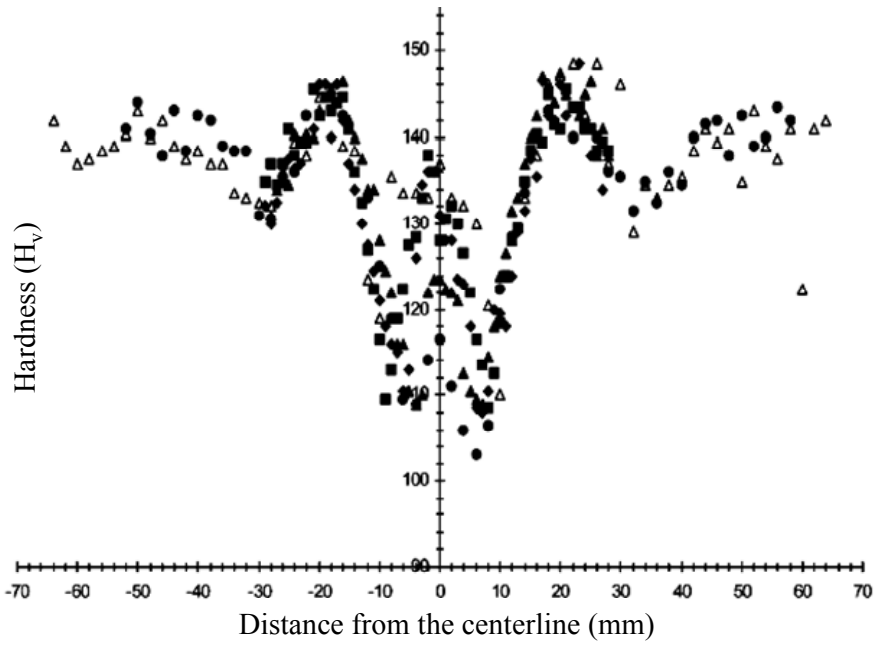

Fig. 2. 11. Microhardness traverse across the FSW at various positions.

(Bussu G *et al*., Inter J Fat 2003;25:77 [80])

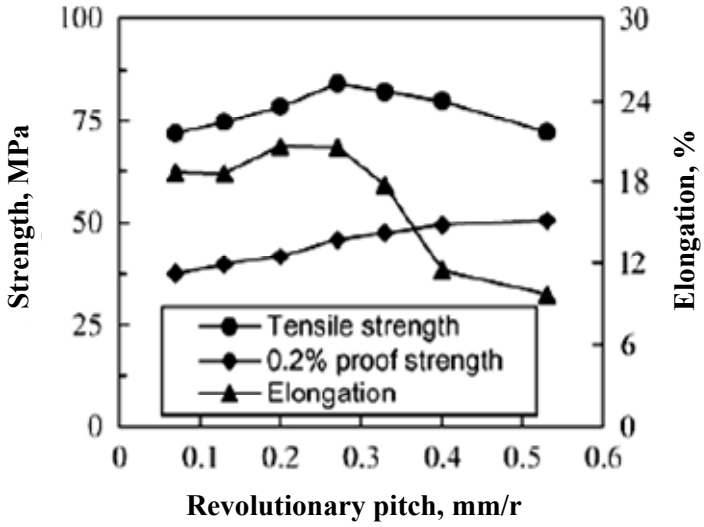

Fig. 2.12. Tensile properties of the joints welded at different revolutionary pitches.

(Liu HJ *et al*., Sci Tech Weld Joining 2003;8:450 [75])

2.2 Residual stress and modeling

2.2.1. Residual stress

The FSW is known to cause lower residual stresses compared to fusion welding techniques, but it still produces a considerable amount of residual stresses, which can significantly affect the mechanical properties of FSW components. Thus, accurate measurements and understanding of the residual stresses and their modeling are important. Recently, the minimization of the residual stresses became one of the most important objectives in FSW research. The residual stress measurements have been conducted using x-ray diffraction (including synchrotron), sectioning methods, strain gage hole-drilling methods, and neutron diffraction [81-84]. The results using neutron and synchrotron diffractions are reported for the FSW Al 7108-T78 (P. J. Webster *et al*., 2002) [27], Al 2024-T3 (M. A. Sutton *et al*., 2002) [67], AA5083 (M. Peel *et al.*, 2003) [63], and 304L Stainless Steel (A. P. Reynold et al, 2003) [34].

In general, compressive residual stress is considered to be beneficial, whereas tensile residual stress regions are susceptible to crack initiation and propagation, particularly near the surface and defects. Figure 2.13 shows a general distribution of residual stresses in a steel fusion weld [32]. The strain gage hole drilling methods and x-ray diffraction techniques are not quite suitable because welding residual stresses are distributed non-uniformly through the thickness of the plate as well as in the two in-plane direction. The neutron diffraction method is most useful for three-dimensional residual stress determination [84]. The main difference between the x-ray diffraction and neutron diffraction is the penetration depth the case of neutron diffraction) [81]. Thus, the neutron

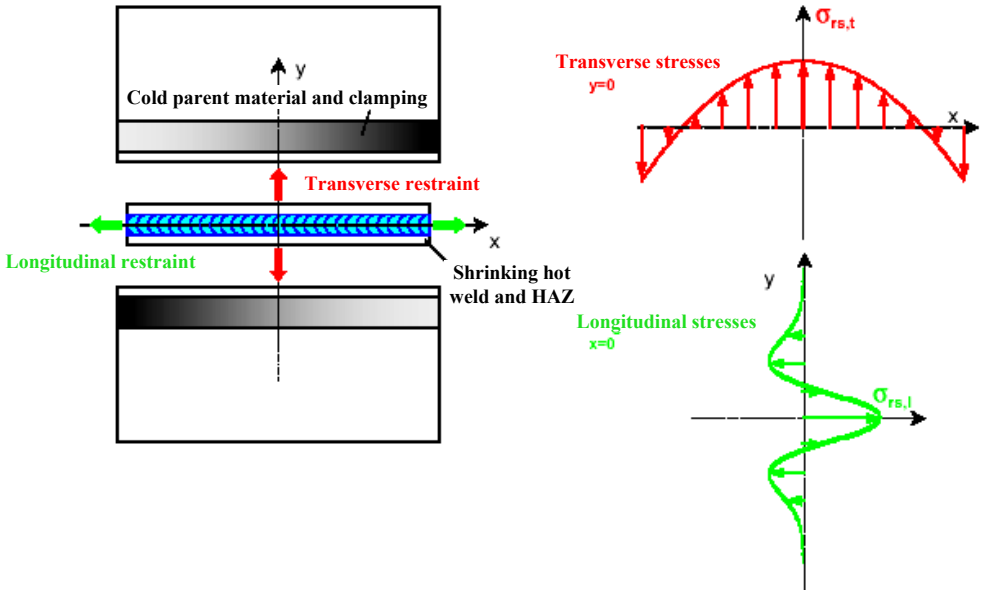

Fig. 2.13. Schematic of the restraints exerted by the cooler parts and the clamping of the plates.

(Webster PJ et al., J strain analysis 2001;36:61 [32])

diffraction measurements are quite suitable for the characterization of the residual stresses in a FSW.

Figure 2.14 shows the principles of strain measurements using neutron diffraction. A collimated neutron beam with the wavelength λ is diffracted by the polycrystalline sample with a diffraction angle of 2θ and passes through a second collimator to reach the detector [23]. The slits of the two collimators define the 'gauge' volume, which is normally more than 1 mm x 1 mm in the case of neutron–diffraction strain mapping. The neutron beam height is typically 1 to 20 mm. From the detected peak, the interplanar distance d_{hkl} (where *hkl*s are the Miller indices of the lattice planes) can be determined using the Bragg law:

$$\lambda = 2d_{hkl}\sin\theta \tag{4}$$

where the 2θ is the diffraction angle corresponds to the maximum of the Bragg-diffracted peak. The corresponding lattice strain is defined as:

$$\varepsilon_{hkl} = \frac{(d_{hkl} - d_o)}{d_o} \tag{5}$$

where d_o is the *hkl* stress-free interplanar distance. The direction of the measured lattice strain is related to the **Q** vector shown in Fig. 2.14. Note that $\mathbf{Q} = \mathbf{K}_H - \mathbf{K}_0$, where $\mathbf{K}_H$ and $\mathbf{K}_0$ are the wave vectors of the diffracted and incident beams, respectively. Basically, the relationship between strain and stress can be represented by 3 x 3 symmetric tensors $\boldsymbol{\varepsilon}$ and $\boldsymbol{\sigma}$, respectively.

Fig. 2.15 shows the arbitrarily chosen OXYZ reference frame in the sample. A generic strain $\varepsilon_{\varphi\psi}$ with direction defined by the φ and ψ angles is expressed [23]:

$$\varepsilon_{\varphi\psi} = \alpha_1^2\varepsilon_{xx} + \alpha_2^2\varepsilon_{yy} + \alpha_3^2\varepsilon_{zz} + 2\alpha_1\alpha_2\varepsilon_{xy} + 2\alpha_2\alpha_3\varepsilon_{yz} + 2\alpha_3\alpha_1\varepsilon_{zx} \tag{6}$$

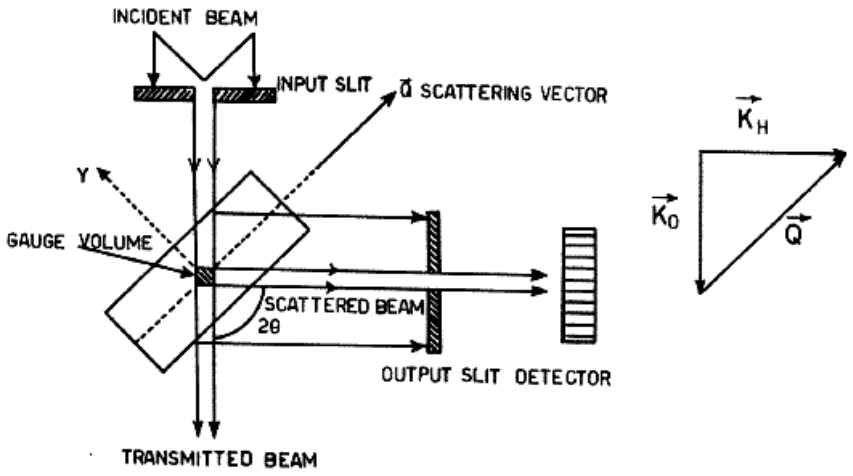

Fig. 2.14. A schematic representation of strain measurement using neutron diffraction

(Albertini G *et al*., Meas Sci Technol 1999;10;R56 [23]).

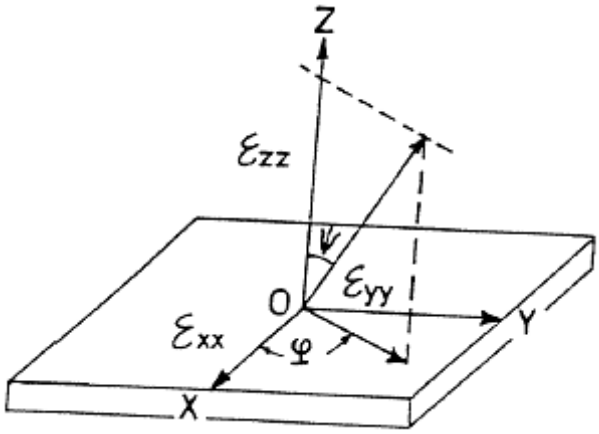

Fig. 2.15. The definition of the directions of the strain $\varepsilon_{\varphi\psi}$ with respect to an arbitrarily chosen reference system within the sample.

(Albertini G *et al*., Meas Sci Technol 1999;10;R56 [23]).

$$\alpha_1 = \sin\psi\cos\varphi\,,\quad \alpha_2 = \sin\psi\sin\varphi\,,\quad \alpha_3 = \cos\psi \tag{7}$$

The six unknowns ε_{xx}, ε_{yy}, ε_{zz}, ε_{xy}, ε_{yz} and ε_{zx} are all the elements of the $\boldsymbol{\varepsilon}$ tensor with symmetry, $\varepsilon_{ij} = \varepsilon_{ji}$. In principle, the strains $\varepsilon_{\varphi\psi}$ measured along six independent directions are required to solve the equation for the six strain components. In an elastically isotropic model E is Young's modulus and v is Poisson's ratio. The principal stresses σ_{xx}, σ_{yy}, σ_{zz} are related to the strains as below;

$$\sigma_{xx} = \frac{E}{(1+\nu)(1-2\nu)}\left[(1-\nu)\varepsilon_{xx} + \nu(\varepsilon_{yy} + \varepsilon_{zz})\right] \tag{8-a}$$

$$\sigma_{yy} = \frac{E}{(1+\nu)(1-2\nu)}\left[(1-\nu)\varepsilon_{yy} + \nu(\varepsilon_{xx} + \varepsilon_{zz})\right] \tag{8-b}$$

$$\sigma_{xx} = \frac{E}{(1+\nu)(1-2\nu)}\left[(1-\nu)\varepsilon_{zz} + \nu(\varepsilon_{yy} + \varepsilon_{xx})\right] \tag{8-c}$$

By diagonalizing the strain tensor, $\boldsymbol{\varepsilon}$, to the principal strain axes OX'Y'Z', the principal strains, ε, can be found. Recently, a number of neutron-diffraction results on the residual stresses in FSWs have been reported [34,45,65,67]. Reynolds *et al*. measured residual stresses in 3.2-mm thick, 305-mm wide and 102-mm long specimens of 304L stainless stee, Fig 2.16, [34]. They showed that the longitudinal residual stresses were higher than the transverse stresses in the thin specimens and found that the peak tensile value is around 300 MPa, which is similar to the yield strength of a parent material, Fig. 2.17. Sutton *et al*. measured the three principal components of the residual stresses through the thickness of the 2024-T3 aluminum alloy plate and reported maximum longitudinal residual stresses of about 105 MPa, Fig. 2.18, [67].

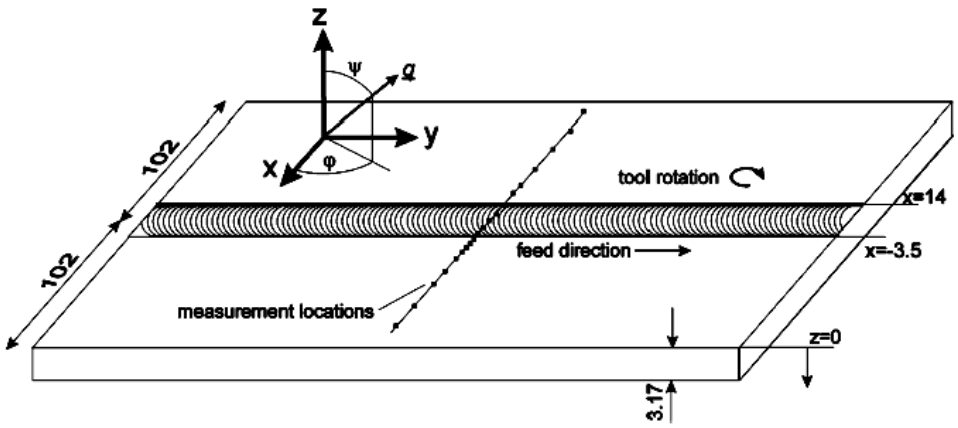

Fig. 2.16. Schematic of the weld dimensions and residual stress measurement locations.

(Reynolds AP *et al*., Scripta Mater. 2003;48;1289 [34])

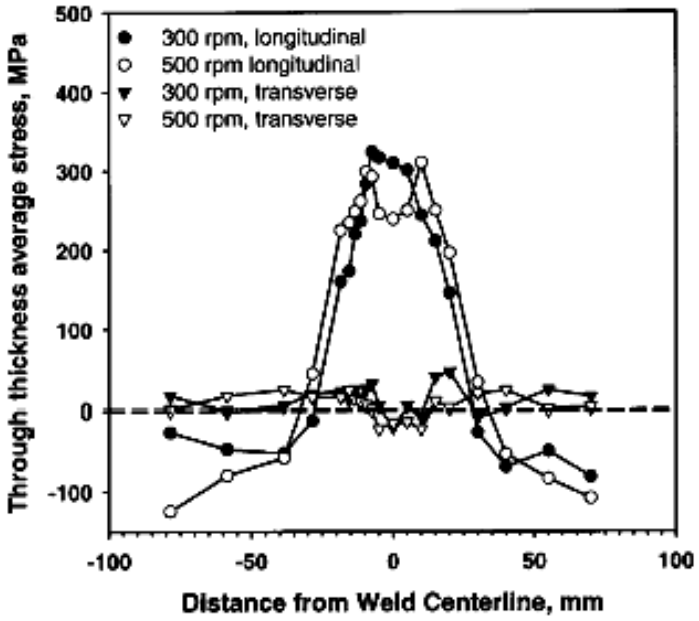

Fig. 2.17. Longitudinal and transverse residual stresses in a stainless steel FSW.

(Reynolds AP *et al*., Scripta Mater. 2003;48;1289 [34])

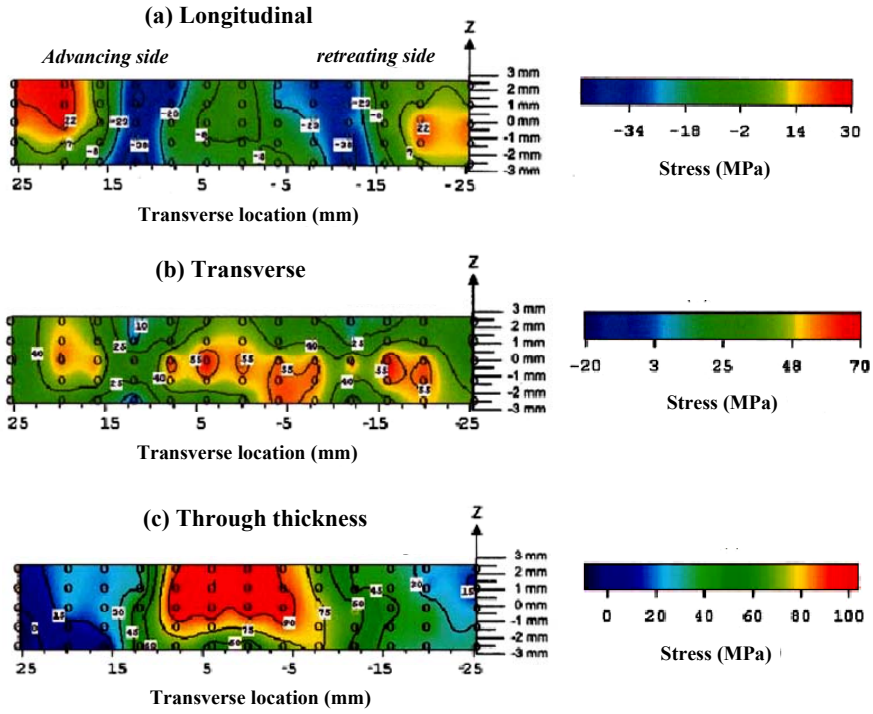

Fig. 2.18. Stress distribution through the thickness of the cross-sections

(Sutton MA *et al*., J Eng Mater Tech 2002;124:215 [67])

2.2.2. Analytical and finite-element modeling

Three kinds of modeling work on the FSW process have been reported. The first type is an analytical thermal modeling [56,58,59], the second type is a Finite Element Model (FEM) based on the solid thermal and thermo-mechanical modeling [54,57,84], and the last is a computational fluid dynamic model (CFD) [55,70]. Based on the heat generation and its flux distribution, a number of analytical thermal models have been proposed. For instance, M. J. Russell *et al*., J. E Gould *et al*., Z. Feng *et al.* presented at the 1st International Symposium on FSW (ISFSW) in 1998. Y. J. Chao *et al*. [56], at the 2nd ISFSW in 1999, P. Colegrove *et al*. in 2001, O. Frigaard *et al.*, and H. Schmidt *et al.* [59] in 2004.

Several CFD models using commercial packages have been developed, which address the influence of the plasticized material flow, with the analytical calculation such as C. B. Smith *et al*. (1999), T. U. Seidel (2001), and H. R. Shercliff *et al*. (2002). Recently, several papers presented two and three dimensional solid mechanical FE model using ABAQUS Explicit or the thermo-mechanical FE modeling program using the experimentally-observed mechanical data, e.g., M. Z. H. Khandkar *et al*. (2003) and M. Song *et al.* (2003) [84].

First, the analytical thermal model estimated the heat generation under the different contact conditions, e.g. sliding and/or sticking conditions between tool conical surfaces and materials in FSW joints [59]. The simplified tool design is presented in Fig. 2.19, where Q_1 is the heat generated under the tool shoulder, Q_2 at the tool pin side, and Q_3 at the tool pin bottom tip, hence the total heat generation, $Q_{total} = Q_1 + Q_2 + Q_3$. The

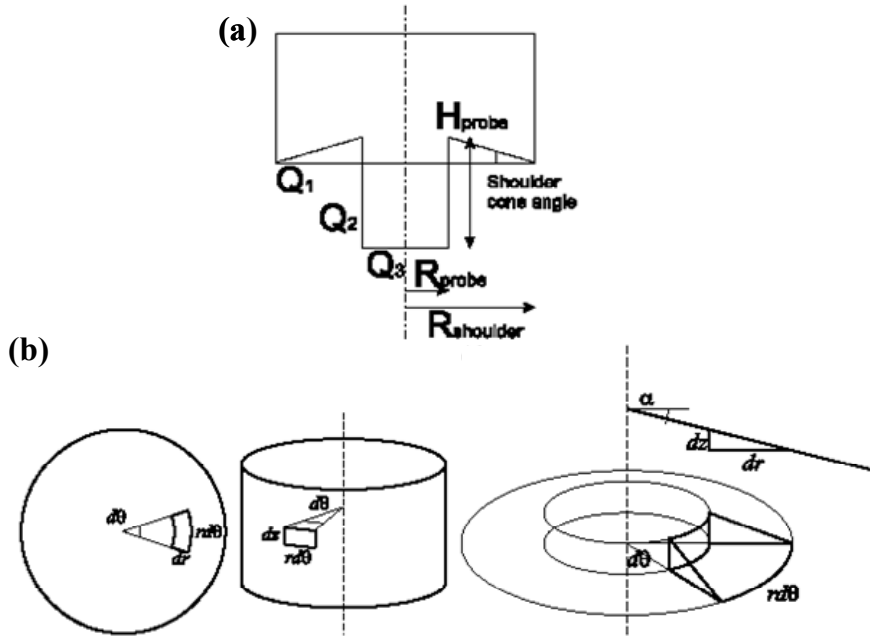

Fig. 2.19. Schematic drawings of surface orientations and infinitesimal segment areas used in analytical estimates of the heat from the three regions denoted by Q_1, Q_2, and Q_3. (a) Cross-section of a simplified tool design and (b) Horizontal, Vertical, Conical/tilted surface

(Schmidt H *et al*., Modelling Simul Mater Sci Eng 2004;12;143 [59])

surface was characterized by either being conical, vertical, or horizontal for the different quantities. The total heat generation from the each part of the shoulder/pin can be calculated, Table 2.1. In case of the shear stress for the sticking condition, since the yield shear stress is estimated to be the yield stress divided by $\sqrt{3}$, $\tau_{contact} = \tau_{yield} = \sigma_{yield}/\sqrt{3}$. The ratio of heat generation by the shoulder is presented as follows:

$$f_{shoulder} = \frac{Q_1}{Q_{total}} = \frac{(R^3_{shoulder} - R^3_{probe})(1+\tan\alpha)}{(R^3_{shoulder} - R^3_{probe})(1+\tan\alpha) + R^3_{probe} + 3R^3_{probe}H_{probe}} = 0.86 \quad (9)$$

Secondly, a finite element modeling of the FSW was used for the prediction of three orthogonal components of the residual stresses, σ_{xx}, σ_{yy}, and σ_{zz}. The model incorporates the mechanical reaction of the tool with the thermo-mechanical processing between the material and the pin/shoulder. For the quantitative understanding of the FSW dynamics, the thermal history and the evolution of longitudinal, transverse, and through-thickness stresses in the FSW are simulated numerically by Fourlier's equation [83]:

$$\rho c \frac{dT}{dt} = div(\kappa \cdot gradT) + q \ in\Omega \quad (10)$$

where q is the power generated by friction between the tool and the top of the work piece and by the plastic deformation work of the central weld zone, T is the temperature, κ is the conductivity, ρ is the material density, and c is the heat capacity. Khandkar *et al*. introduced a torque based heat input model, where the torque/power known from experiments is used in the expression for the heat source. Figure 2.20 shows the residual stress contours in three principal directions of the FSW. The longitudinal and transverse residual-stress contours show the predicted maximum stress and shows that the longitudinal residual stress is greater than the transverse residual stress at the top surface

Table 2.1. Analytical formulae for the heat generated by each part of the tool.

Heat Source	Analytical formulae
Heat generated by the shoulder	$Q_1 = \int_0^{2\pi} \int_{R_{probe}}^{R_{shoulder}} \omega \tau_{contact} r^2 (1 + \tan\alpha)\, dr\, d\theta$ $= \frac{2}{3}\pi\, \tau_{contact} \omega (R^3_{shoulder} - R^3_{probe})(1 + \tan\alpha)$
Heat generated by the pin	$Q_2 = \int_0^{2\pi} \int_0^{H_{probe}} \omega \tau_{contact} R^2_{probe}\, dz\, d\theta = 2\pi\, \tau_{contact}\, \omega\, R^2_{probe} H_{probe}$
	$Q_3 = \int_0^{2\pi} \int_0^{R_{probe}} \omega \tau_{contact} r^2\, dr\, d\theta = \frac{2}{3}\pi_{contact} \omega R^3_{probe}$
Total heat	$Q_{total} = Q_1 + Q_2 + Q_3$ $= \frac{2}{3}\pi\, \tau_{contact}\, \omega((R^3_{shoulder} - R^3_{probe})(1 + \tan\alpha) + R^3_{probe} + 3R^2_{probe} H_{probe})$

(Schmidt H et al., Modelling Simul Mater Sci Eng 2004;12;143 [59])

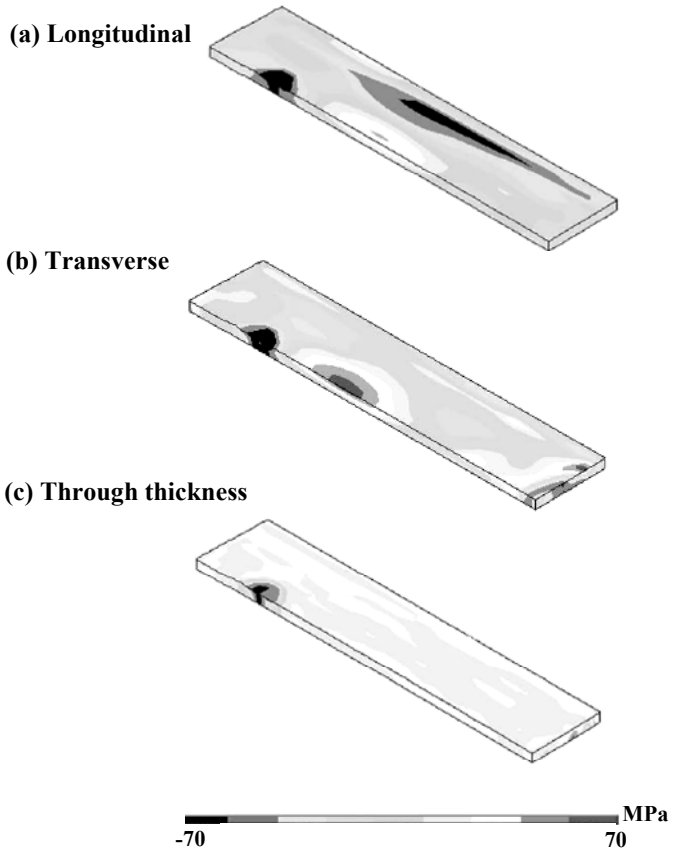

Fig. 2.20. Predicted three-dimensional residual stress distribution in the FSW plate

(Chen CM *et al*., Intern J Machine Tools & Manufacture 2003;43:1319 [54])

of the weld.

In the view of thermal/fluid dynamics, the flow visualization was firstly performed via the bimetals technique using inserted vortices of Cu into Al, Fig 2.21. Surrounding the pin (indicated by the arrows ***A***) there is an open space with no material, a nearly circular region outside this open region (indicated by the arrows ***B***), and a transition zone (marked as the arrow ***C***) outside of the rotational zone. The material on the retreating side of the pin is transferred into this transition zone and recrystallized/equiaxed entrained grains show near ***D***, Fig. 2.21(a) [55]. Besides, Fig. 2.21(b) shows that the material flow in the top one-third of the figure is determined by the tool shoulder rather than by the tool pin. It suggests that the upper part is stirred and plasticized by mainly the tool shoulder and is different from the middle and lower parts in microstructural characterization of the FSW. In summary, the extensive research in FSW has mainly focused on the characterization, analysis, evaluation, and modeling of the mechanical properties, particularly residual stresses and tensile behavior.

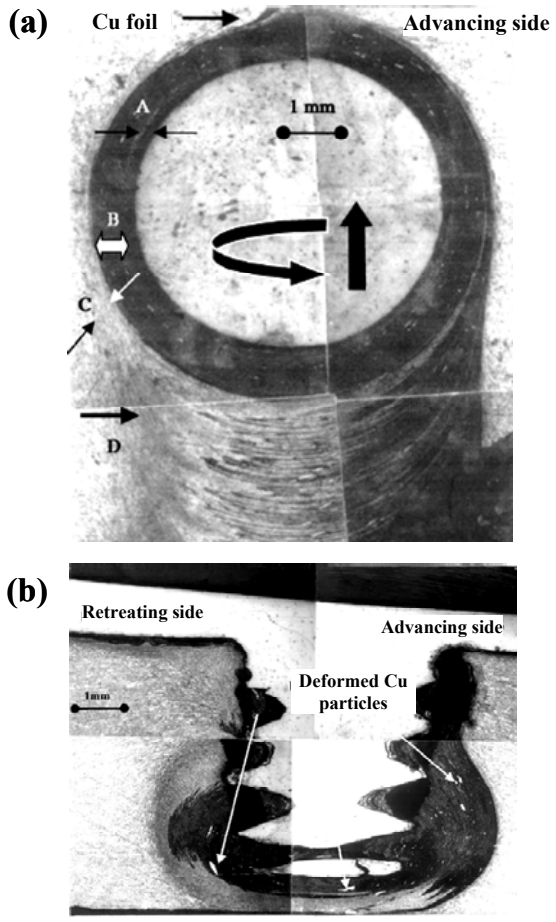

Fig. 2. 21. Materials flow experiment using a Cu foil marker of the frozen tool pin; (a) surface and (b) cross-section with the frozen pin.

(Guerra M et al., Mater Char 2003;49:95 [55])

Chapter III Residual strain in a FSP aluminum alloy

3.1. Materials, processing, and sample preparation

3.1.1. Objectives

Heat and plastic deformation involved in the friction-stir processing (FSP) can induce significant internal stresses that may be detrimental to the integrity and performance of components. For example, Synchrotron x-ray diffraction studies by Peel *et al.* suggested that the longitudinal residual stresses are dominated by the thermal input rather than the mechanical deformation by the tool pin [63]. Although the heat input is considered as the main source of internal stresses in the FSP, direct experimental evidence supporting this is not available in the literature to date. This chapter will present (i) a novel experimental approach used in the specimen preparation and (ii) neutron-diffraction measurement results to de-convolute the effects of heat and plastic deformation on the development of internal strains during the FSP.

3.1.2. Materials and specially designed processing

Al 6061 alloy was selected due to the extensive 6xxx series alloy's usage as a structural material. Commercial 6061-T6 aluminum-alloy rolled plates were solution heat treated and artificially aged for 6 hours at 185°C. The nominal chemical composition in weight percent is 1.0 Mg, 0.6 Si, 0.3 Cu, and balance Al. The dimensions of the two FSP specimens prepared at the Oak Ridge National Laboratory were 306 x 306 x 6.5 mm, Fig.

3.1. The four corners of the transverse sides (y-direction) were clamped during the processing. The clamping was removed after the plate was cooled to 25 °C after the processing. It should be noted that all samples were prepared by performing the "bead-on-plate" processing method, known as the friction-stir processing (FSP), to eliminate the complications from the gap variations. Two different plates were prepared to determine the effects of the frictional heating and severe plastic deformation on the internal-strain distribution in the plate. (i) *Case 1* (a typical FSP): a plate processed with both stirring pin and tool shoulder, i.e., a regular friction-stir processing plate subjected to both severe plastic deformation and frictional heating and (ii) *Case 2* was processed under the same conditions as *Case 1*, but utilizing a special tool without the pin and, hence, was subjected mainly to the frictional heating from the tool shoulder.

3.1.3. Tool design and processing parameters

Typical tool and specially designed tool will be prepared for the two different characteristic plates. Typical tool will be made of an H-13 tool steel using 19.05 mm shoulder diameter and 6.35 mm pin diameter with 6.23 mm pin depth for full penetration into the plates. On the other hand, the special tool had no stirring tool pin at the shoulder center to minimize the plastic deformation imposed on the sample as shown in Fig. 3.2. The processing parameters were decided by several preliminary experiments for the highest quality FSP bead. *Cases 1* and *2* were processed using the following parameters: 4.7 mm/sec traveling speed, 1,250 rpm clockwise rotatin g speed, and 12.4 MPa compressive pressure. Note that *Case 2* was processed under the same conditions as *Case 1*, but utilizing a special tool without the stirring pin, Fig. 3.2.

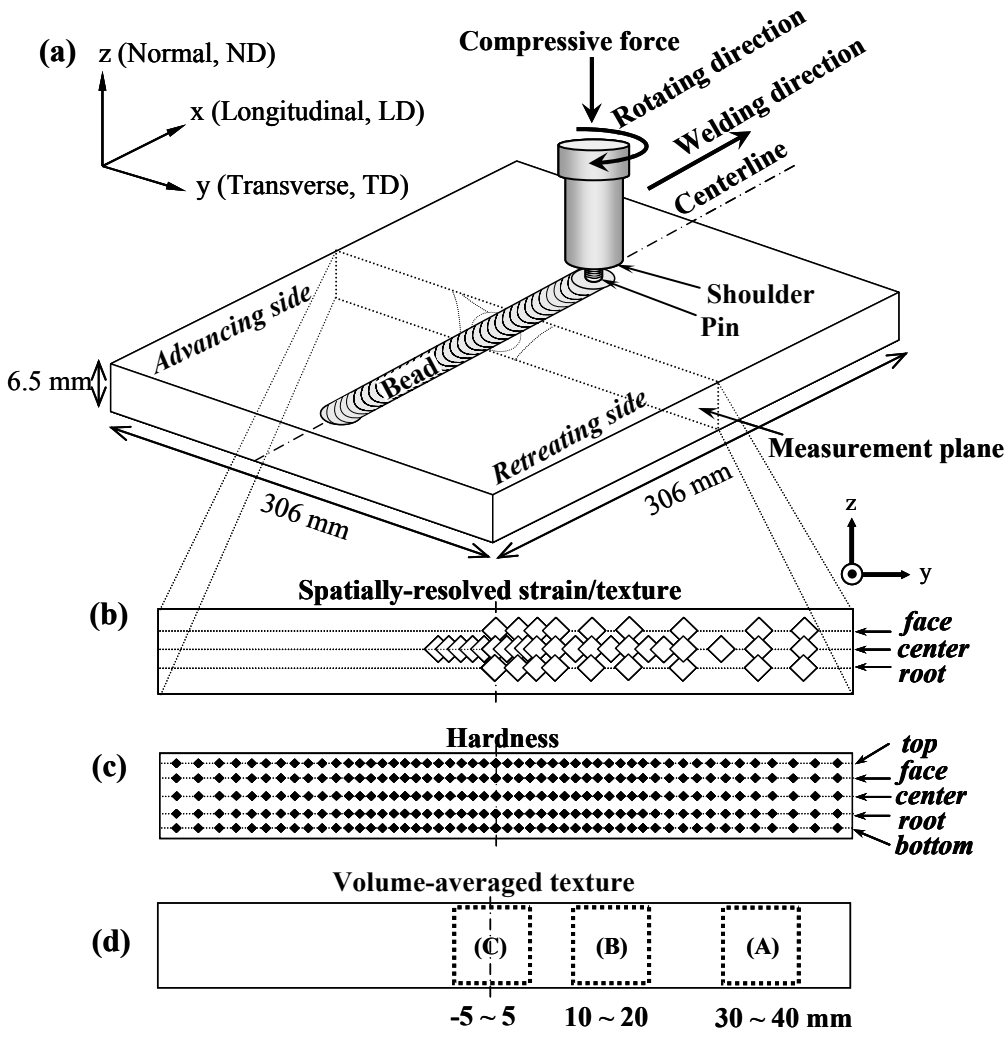

Fig. 3.1. Schematic of (a) the friction-stir processing (FSP), (b) the spatially-resolved neutron-diffraction measurement positions, (c) the hardness measurement positions, and (d) the positions where the coupons were machined out for the volume-averaged texture measurements.

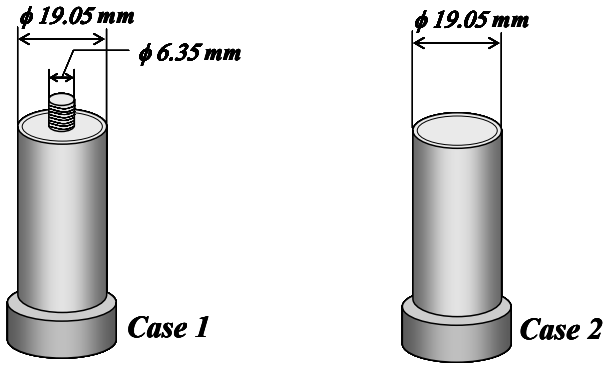

Fig. 3.2. Schematic of the tool design for the *Cases 1* and *2*.

3.2. Residual strain measurements and analyses

Spatially-resolved neutron strain scanning is a well-established technique [22-24]. The determination of residual strains using neutron diffraction is based on the volume-averaged measurement of interplanar spacings (*d*-spacings) in various crystallographic and geometric orientations [15]. The residual strains in the FSP plates were measured using the SMARTS (Spectrometer for MAterials Research at Temperature and Stress) diffractometer at the Los Alamos Neutron Science Center, Fig. 3.3, [17].

The internal strains were measured from FSP 6061-T6 Al plates using neutron diffraction. The two FSP specimens, i.e., *Case 1* subjected to both heating and plastic deformation and *Case 2* subjected mainly to the heating effect, were examined to study the influence of the heat input from the tool shoulder on the internal strains. First, the FSP plate was positioned on the xyz-ω stage of the instrument using two theodolites with an accuracy of 0.05 mm in directions and 0.1 º in angle. The scattering volume was defined by using height and width of incident-beam slits and radial collimators for the diffracted beams. The diffraction patterns were measured at 21 points along the *center* and 9 points each along the *face* and *root* as shown in Fig. 3.1(b).

Two sets of scans were performed at various locations across and through the thickness of the cross section of the FSP plates, Fig. 3.4. The diffraction patterns with their scattering vectors parallel to the LD (x) and ND (z) were measured simultaneously at the middle of the plate length (x) and thickness (z) along the y-direction using 2-mm height (x) and width (z) of incident beam slits and 2-mm radial collimators (y) leading to gauge volumes of a 2 (x) × 2 (y) × 2 (z) mm^3. The diffraction patterns with their

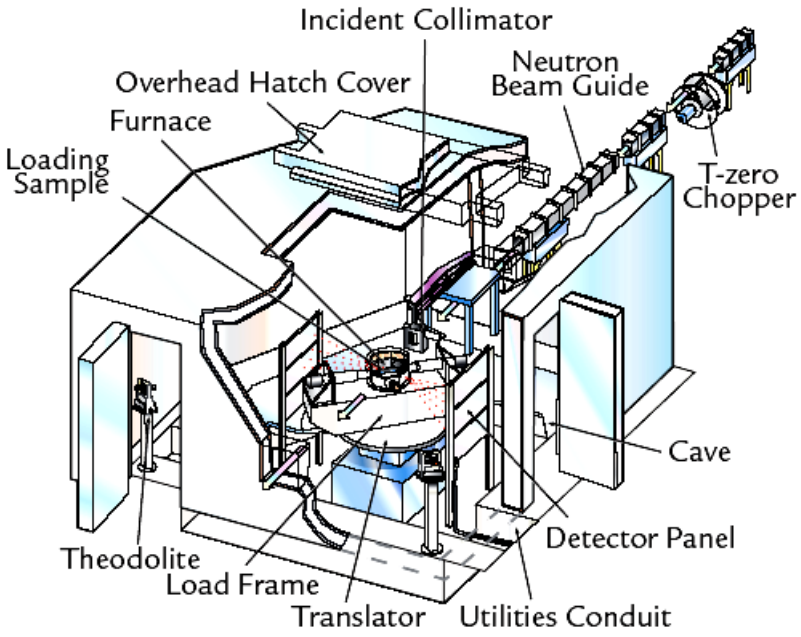

Fig. 3.3. Schematic view of the SMARTS diffractometer.

(Bourke MAM *et al*., Appl Phys A 2002;74;S1707 [17])

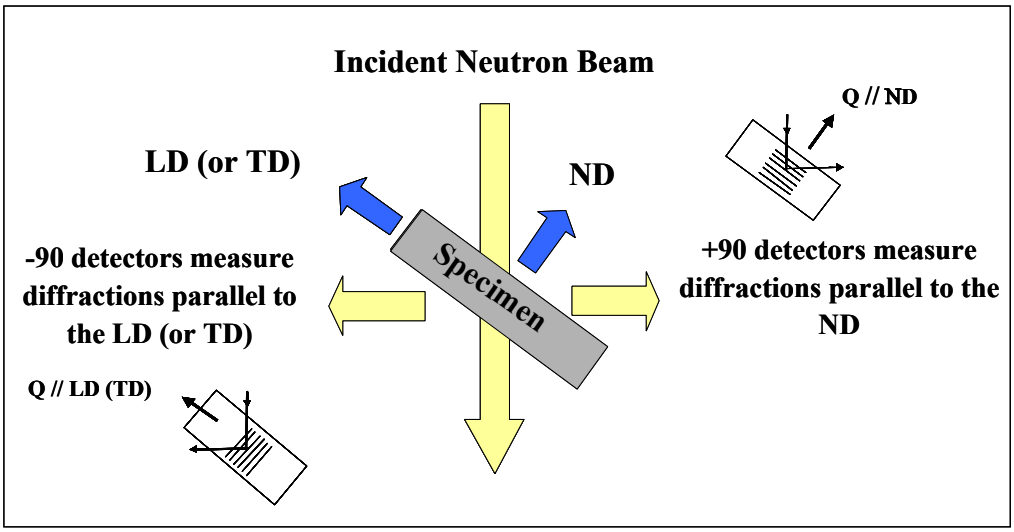

Fig. 3.4. Schematic view of the neutron diffraction measurement geometry.

scattering vectors parallel to the TD (y) and ND (z) were also measured using a scattering volume of 20 (x) × 2 (y) × 2 (z) mm^3 with the long dimension along the LD [67].

Second, the lattice spacing (*a*) was obtained by Rietveld refinement of the diffraction patterns using the General Structure Analysis System (GSAS) [85]. Rietveld method is a method for the whole peak adjustment between the characteristics of the experimental peaks and the calculated diffraction pattern associated with the alumimum crystallographic structure (or atomic positions, space group, and texture) and instrumental parameters (background and peakshape), Fig. 3.5. Residual strains can be calculated using the Eq. (1).

3.3. Residual strain distribution

Figure 3.6 shows the residual-strain profiles (ε_{xx}, ε_{yy}, and ε_{zz}) measured by neutron diffraction from the typical FSP plate. For *Case 1*, the three strain components have a characteristic peak-and-valley shape. For example, ε_{xx} is tensile near the bead, which is 19 mm wide. Following the strain profile on the retreating side, it shows a plateau, which fluctuates between 980 ~ 1,200 με within the bead, increases to about 2,140 με around 11 mm, and drops to small compressive strains about 25 mm away from the centerline. Compressive ε_{yy} near the centerline is balanced by small tensile strains away from the bead. Similarly, ε_{zz} is also in compression with a slightly higher magnitude than ε_{yy}. Overall, the results of *Case 1* are qualitatively consistent with the literature [34,63]. The shoulder-only case (*Case 2*), subjected mainly to the frictional heating, is presented in Fig.

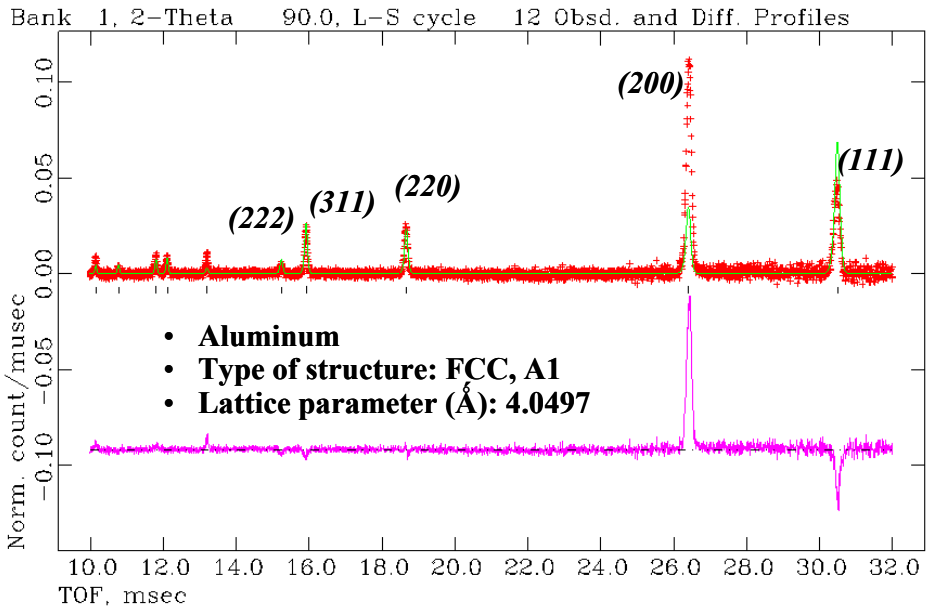

Fig. 3.5. An example of the measured neutron-diffraction pattern in Aluminum (red), the calculated pattern (green), and the difference pattern (purple).

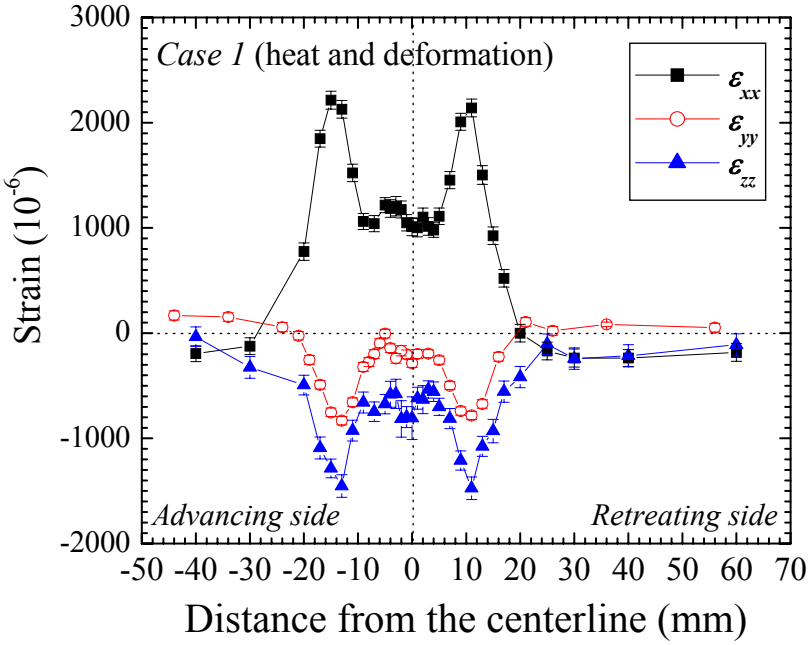

Fig. 3.6. Longitudinal (ε_{xx}), transverse (ε_{yy}), and through-thickness (ε_{zz}) strains measured in the typical FSP (*Case 1*)

3.7. ε_{xx} does not show the plateau region within the bead width; instead it linearly increases from 1,530 με at the centerline to 2,120 με at 9 mm, and then drops to small compressive strains on the retreating side.

3.4. Sources of the residual strains

First, the residual-strain profiles of *Case 2* are compared with well-established results on the conventional fusion welding (e.g., K. Masubuchi [86]). The overall shape of ε_{xx}, shown in Fig. 3.7, is similar to that of a typical arc weld in that maximum tensile appears near the bead. The similarity in the profile is attributed to the fact that ε_{xx} in both processes is generated due to the localized thermal expansion by the moving heat source under the restraint of the base material during welding, followed by a hindered shrinkage during the subsequent cooling. Note that the distance from the centerline to the peaks of the strain profile is around 9 ~ 10 mm, which is similar to the radius of the tool shoulder (9.5 mm). The peaks of all three strain components at around ±9.5 mm are associated with the interplay between gradients of the thermal flux caused by the rotating tool shoulder and a softening caused by the yield-stress reduction [87] due to microstructural changes such as aging [42] and/or grain size changes [63].

Let us now compare *Cases 1* and *2* to discuss the effect of the stirring pin. In Fig. 3.8, comparing ε_{xx} for the two cases, *Case 2* exhibits internal strains comparable to *Case 1* in terms of both magnitude and profile shape. This clearly shows that the frictional heating from the tool shoulder is the major source of internal strains in the FSP, which a

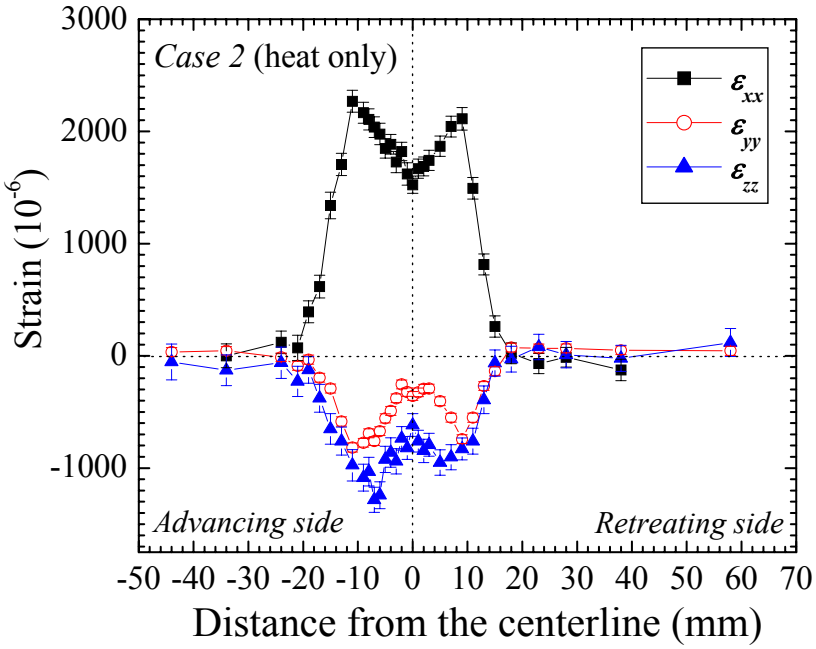

Fig. 3.7. Longitudinal (ε_{xx}), transverse (ε_{yy}), and through-thickness (ε_{zz}) strains measured in the shoulder only case (*Case 2*)

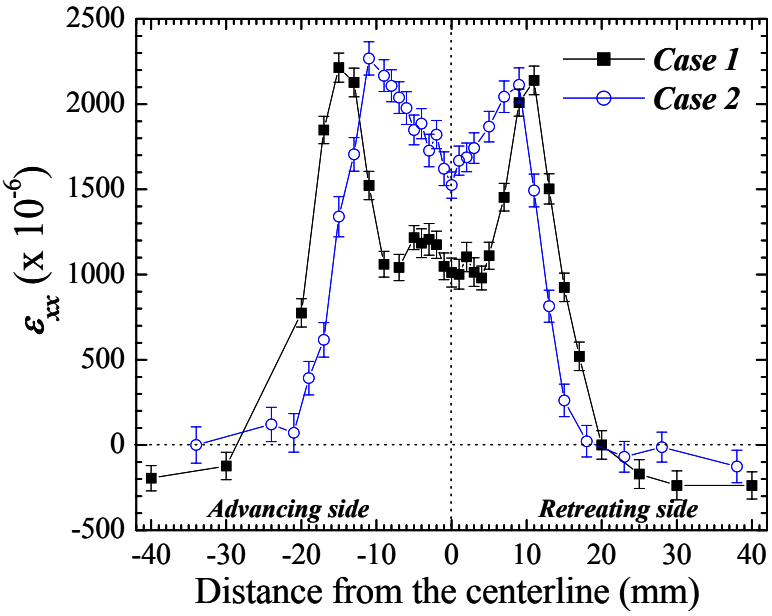

Fig. 3.8. Comparison of the longitudinal strain profiles in *Case 1* (typical FSP) and *Case 2* (the shoulder-only case). It shows the frictional heating affects significant the residual strain profiles and main source of the residual strains.

confirms previous analytical result. Schmidt *et al.* suggested that 86% of heat during FSW is generated by the friction of the shoulder contacting on the surface in a "sticking condition", where frictional shear stress exceeds the yield stress of the material [59]. Another implication is that when the FSP is used to modify the surface microstructure even without using the pin, it should be expected that the materials could have residual strains comparable to a typical FSW part. In addition, there are a few clear differences between *Cases 1* and *2*. Firstly, *Case 1* shows a plateau region, of which the strain magnitude is smaller (980 ~ 1,200 με) compared to that of the minimum in *Case 2* (1,530 με). The plateau in the strain profile is related to the severely-deformed recrystallized zone caused by the pin, resulting in the localized softening of the material and as a consequence strain relief [63]. Secondly, the width of the strain profile (e.g., the peak-to-peak distance) for *Case 1* is about 6 mm wider than that of *Case 2*, which may be related to the flow of material creating the plasticized zones such as thermo-mechanical zones in addition to the heat-affected zone [42,55]. The plateau and broader peak-to-peak distance in the strain profile of *Case 1* are the characteristics of the typical FSW caused by synergistic effects of the pin and shoulder.

In summary, the residual strains were measured from friction-stir processed (FSP) 6061-T6 Al plates using neutron diffraction. The comparison between a regular FSP specimen (subjected to both heating and deformation) and a plate processed only with the tool shoulder (subjected mainly to the heating effect) clearly showed that the heat input from the tool shoulder is a major source of the residual strains.

Chapter IV Residual stresses and angular distortion in a FSP aluminum alloy

4.1. Residual stress analyses

4.1.1. Objectives

Residual stresses generated during FSW/FSP can be detrimental to the integrity and performance of components. Sutton *et al.* reported asymmetric residual stress distributions in the transverse and through-thickness directions of 2024-T3 Al alloy FSW plates measured using neutron-diffraction technique [67]. Furthermore, neutron-diffraction studies of the 304L stainless steel FSW plate by Reynolds *et al.* showed the opposite sign of the transverse residual stress between the upper and the lower parts of the plate suggesting that the residual stress can cause a bending moment around the longitudinal axis, resulting in an angular distortion [34].

The objective of the current chapter is to understand the cause of the asymmetric through-thickness residual stress distribution and its relationship to the non-uniform thermal distributions through the thickness of the plate and the subsequent angular distortion. The results will be useful for the development of more accurate computational simulations and the optimization of processing conditions.

4.1.2. Through-thickness measurement and analysis

Localized residual stresses can be detrimental to the integrity and performance of components due to the effect of the residual stress on deformations including angular distortions [86,87]. To understand the cause of the asymmetric through-thickness residual

stress distribution and its relationship to the angular distortion by the case studies of FSP plates, approximately 40 points were measured along the middle of the plate thickness (z), 1.26 mm above the middle, and 1.26 mm below the middle, namely *center*, *face*, and *root*, respectively, Fig. 3.1(b). Residual strains can be calculated using the Eq. (1) and the residual strain data are converted to the principal residual stresses (i.e., σ_x, σ_y, and σ_z) using Eq. (2), where E, Young's modulus (69 GPa); v, Poissons ratio (0.345) for the Al 6061-T6 alloy. Non-uniform frictional heat distributions through the thickness of the plate followed by the geometric expansion and contraction with constraints are generally considered as the cause of the angular distortion. The direct comparison between *Cases 1* and *2* can provide the relationship between the geometric angular distortion and residual stress distribution through the thickness of the plate generated during the FSW/FSP.

4.1.3. Stress-free lattice parameter (d_o) measurements

For the neutron diffraction measurements, a careful investigation of the stress-free lattice parameter (d_o) is required as a reference to determine accurate residual strains, since the lattice parameter could be significantly altered by the microstructural changes via re-distribution of the chemical compositions introducing large errors in the results. For example, Peel *et al.* suggested that error in residual strain caused by the microstructural changes such as the precipitation or dissolution of precipitates (Mg-Si particles) could be about ±150 με in the AA5083 friction stir welds [63]. To verify the potential influence of chemical composition changes on the d_o changes in the current study, the d_o was carefully determined using coupons (2 x 2 x 2 mm^3) machined from the FSP plate to relieve the macroscopic residual stresses. The variation of the d_o results from

measurements provided the *d*-spacing variations and corresponding the apparent strain of the FSP Al 6061-T6 alloy.

4.2. Macrostructure and through-thickness residual stress distribution

Figures 4.1 and 4.2 show macrostructures of *Cases 1* and *2*, respectively. Figure 4.1 shows the cross-sectional macrostructure of *Case 1*, which reveals characteristic regions of the FSP: the initial base material (BM), the heat-affected zone (HAZ), the thermo-mechanically affected zone (TMAZ), and the dynamic recrystallized zone (DXZ). The DXZ is known to have a refined grain structure caused by the severe plastic deformation due to the stirring tool pin near the centerline [35,42]. Figure 4.2 shows the macrostructure of *Case 2*, which is distinctly different from that of *Case 1*. Clearly, the DXZ is absent in *Case 2*. The dark half-circle region in the upper part of the cross-section is directly affected by the tool shoulder and designated as TMAZ (*face*), since it is subjected to both heating and partial plastic deformation from the pressing tool shoulder. The other parts are designated as the HAZ (*root*), HAZ, and BM similar to *Case 1*. Figure 4.3 shows almost no bending in *Case 1*, while approximately 1-mm concave bending at the edge of the plate and a non-homogeneous macrostructure though the thickness of the plate in *Case 2*.

Figures 4.4 and 4.5 show the residual strain profiles measured through the thickness of the plates using neutron diffraction. Overall, *Case 1* shows relatively little variations in the residual strain profiles between the *face, center,* and *root*, Fig. 4.4, while *Case 2* exhibits significant through-thickness variations as shown in Fig. 4.5. First, for

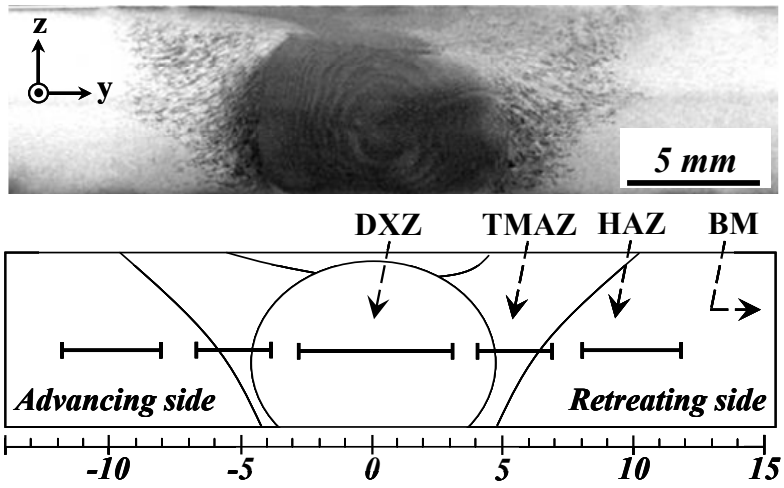

Fig. 4.1. The cross-sectional macrostructure of *Case 1* (typical FSP) showing the base material (BM), heat-affected zone (HAZ), thermo-mechanically affected zone (TMAZ), and dynamic recrystallized zone (DXZ) of the FSP 6061-T6 Al alloy.

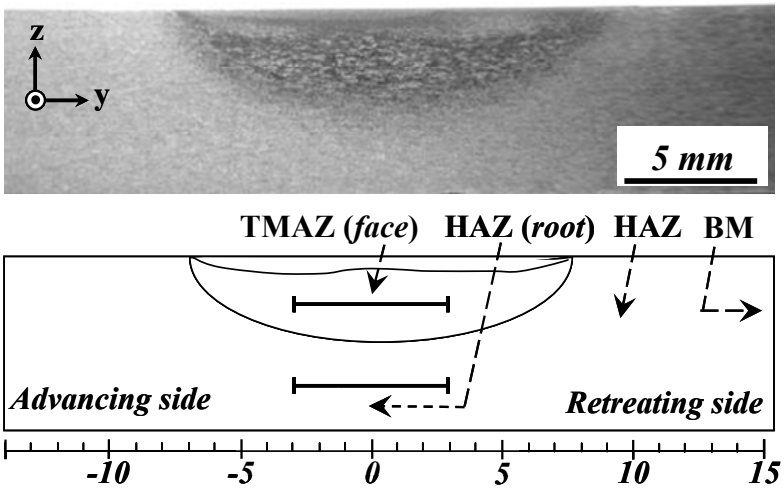

Fig. 4.2. The cross-sectional macrostructure of *Case 2* (the shoulder-only case) showing the base material (BM), heat-affected zone (HAZ-*root* and HAZ), and thermo-mechanically affected zone (TMAZ-*face*).

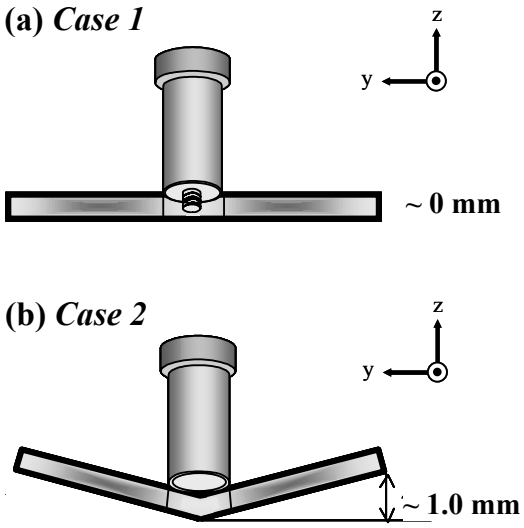

Fig. 4.3. Schematics of the observed angular distortion: (a) *Case 1* (a typical FSP), (b) *Case 2* (the shoulder-only case).

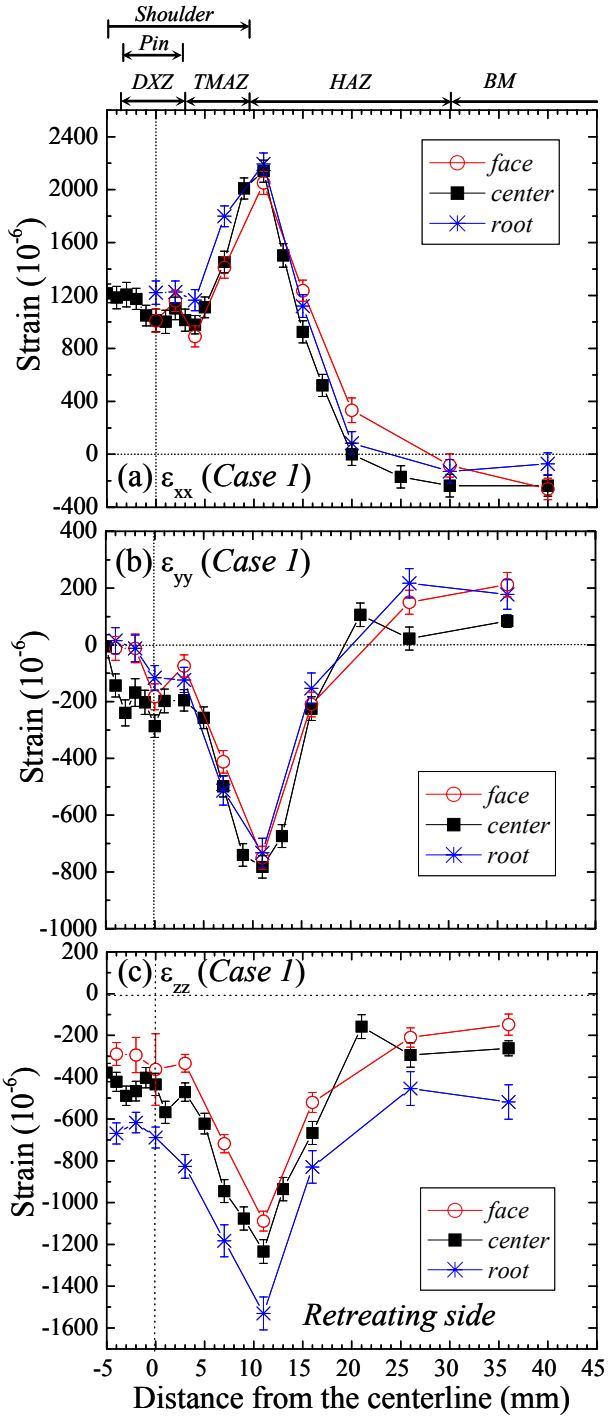

Fig. 4.4. Longitudinal (ε_{xx}), transverse (ε_{yy}), and through-thickness (ε_{zz}) residual strains along the *face*, *center*, and *root* of *Case 1*.

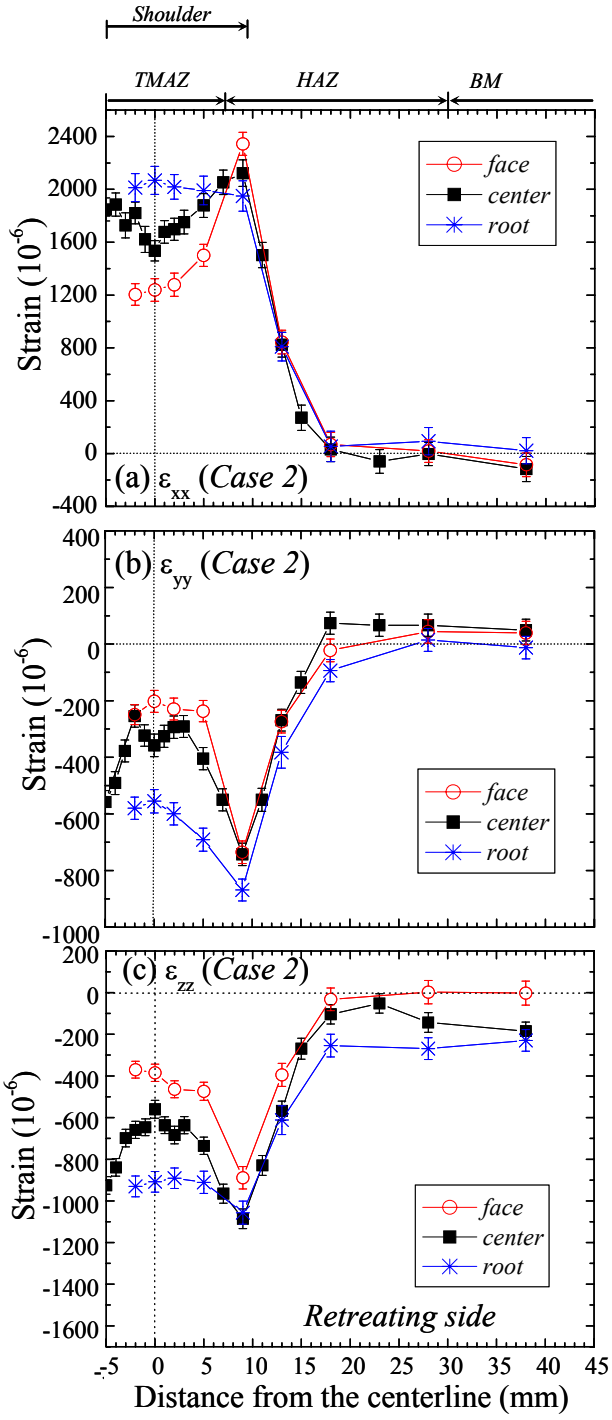

Fig. 4.5. Longitudinal (ε_{xx}), transverse (ε_{yy}), and through-thickness (ε_{zz}) residual strains along the *face*, *center*, and *root* of *Case 2*.

Case 1, the three strain components have the characteristic peak-and-valley shape. For example, the ε_{xx} is tensile, Fig. 4.4(a), and the ε_{yy} is highly compressive near the TMAZ and HAZ boundary, which is balanced by small tensile strains at about 25 mm away, Fig. 4.4(b). Similarly, ε_{zz} is also in compression with a slightly higher magnitude than ε_{yy}, Fig. 4.4(c). The reason of the large tensile strain along LD near the centerline balancing away to the small compression can be explained by the conventional fusion welds. Similarly to the welding, the residual strains in the FSP mainly can be generated by the localized thermal expansion with the moving heat source under the constraints of the surrounding cold base material, followed by a hindered shrinkage during the subsequent cooling [86]. In terms of the through-thickness variations between the *face*, *center*, and *root* in *Case 1* are almost equal to each other under the current measurement conditions.

Secondly, the strain profiles of the shoulder-only case (*Case 2*) also show the peak-and-valley shape, Fig. 4.5. However, through-thickness strain profiles among the *face*, *center*, and *root* in *Case 2* show significant different gradients near the centerline compared to *Case 1*. For example, the ε_{yy} profile of the *root* in *Case 2*, Fig. 4.5, shows a large compression (-550 ~ -870 με) compared to the ε_{yy} of the *face* and the *center* near the centerline. The peak position of the profile at 9 mm is similar to the 9.5-mm radius of the tool shoulder, the different gradients in the profiles could be related to the interplay between non-uniform thermal distributions caused by the tool shoulder and a softening caused by the yield-stress reduction due to microstructural changes such as dissolutions or aging of the precipitates [35,87]. This trend was not seen in *Case 1*, where the pin acting as an additional heat source and also a heat-transfer medium through the thickness

of the plate. Thus, it could be said that the significant effect of the stirring pin is to minimize the through-thickness variations of the residual strains during the FSP.

Figures 4.6 and 4.7 show the residual stress profiles in *Cases 1* and *2* through the thickness of the plate. Overall, two profiles are more complicate than the strain profiles. First of all, comparing σ_y in *Cases 1* and *2*, Figs. 4.6(b) and 4.7(b), the residual stress profiles of the *face* and *root* are widely ranged in *Case 2*. For example, the residual stress along the *face* is mostly tensile while the residual stress at the *root* is compressive in *Case 2* and unlike *Case 1*. Figures 4.8 and 4.9 more clearly show the asymmetric distributions of the residual stress through the thickness of the plate based on the through-thickness profiles of the σ_{yy} component, Figs. 4.6(b) and 4.7(b). Note that white dashed lines, Fig. 4.8, present the boundaries of change in the residual stress from the tension to the compression. *Case 1* exhibits almost vertical contour lines indicating insignificant through-thickness residual stress variations. On the other hand, most of the contour lines in *Case 2* show about a 45º gradients indicating asymmetric residual stress distributions through the thickness of the plate. Note that the edges of the tool shoulder are located at around 9.5 mm from the centerline.

4.3. Residual stresses and angular distortion

The relationship between the through-thickness residual stress variation and angular distortion about the LD axis of the plates will be discussed. The residual stress profiles and mapping in *Case 2* show an asymmetric through-thickness distribution of the residual stress compared to *Case 1*, Fig. 4.8. To know the relationship between measured

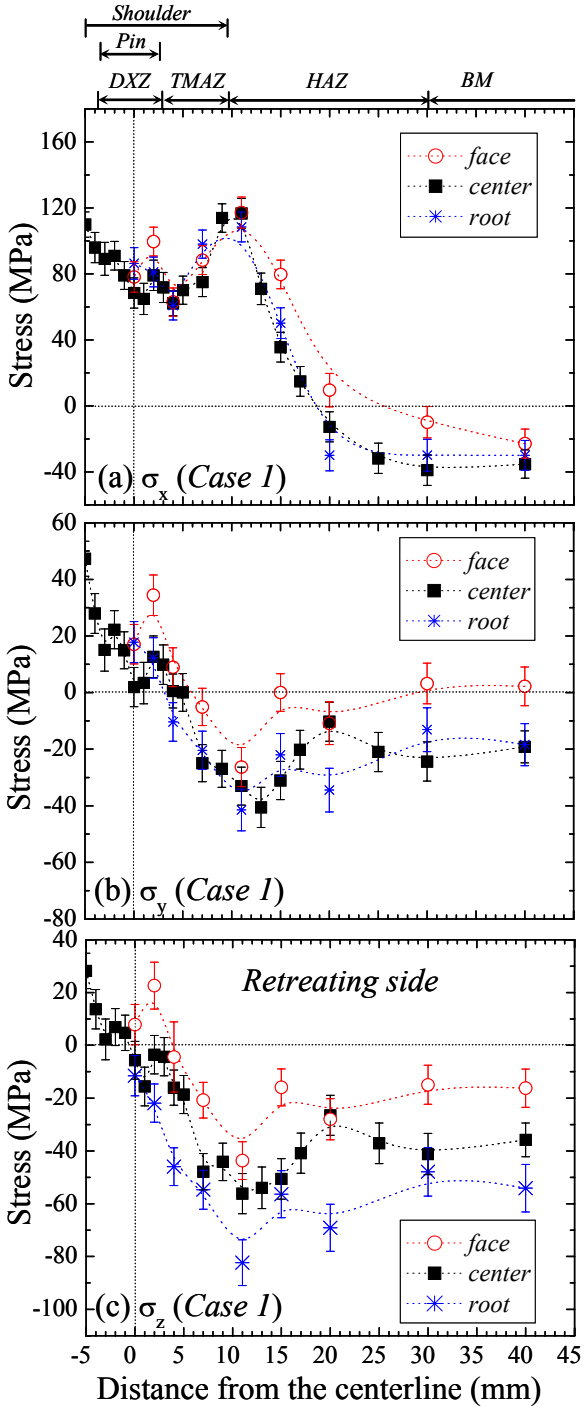

Fig. 4.6. Longitudinal (σ_{xx}), transverse (σ_{yy}), and through-thickness (σ_{zz}) residual stresses in *Case 1*.

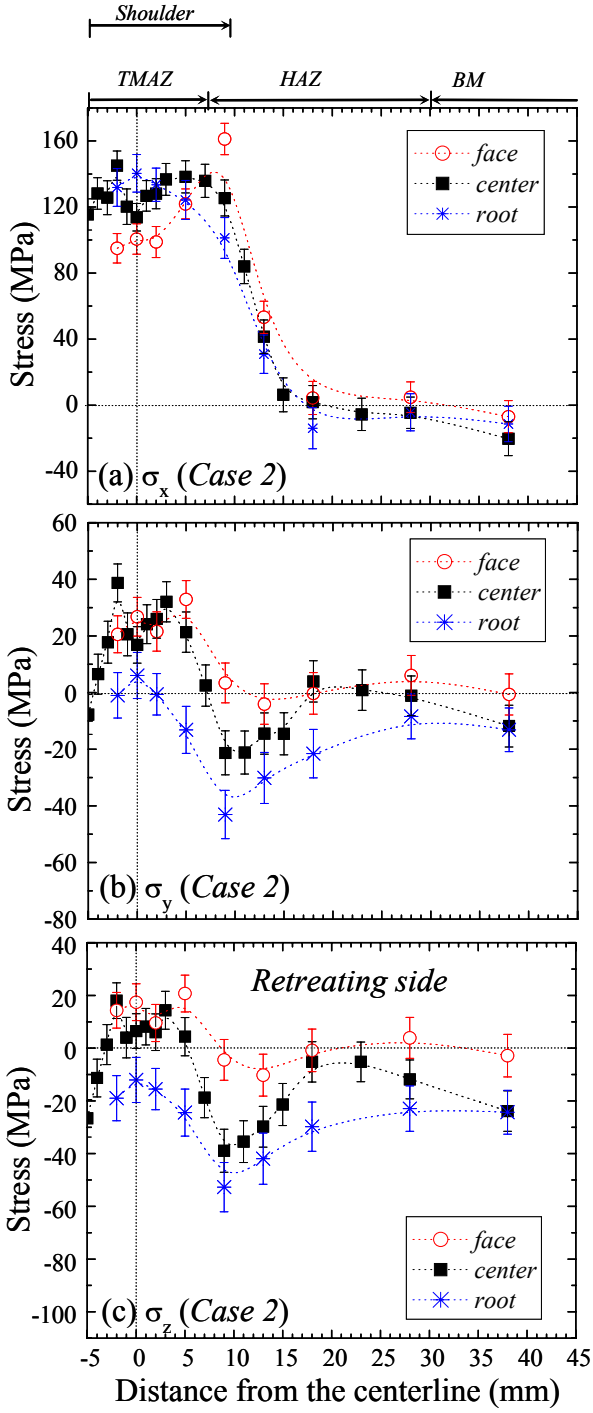

Fig. 4.7. Longitudinal (σ_{xx}), transverse (σ_{yy}), and through-thickness (σ_{zz}) residual stresses in *Case 2*.

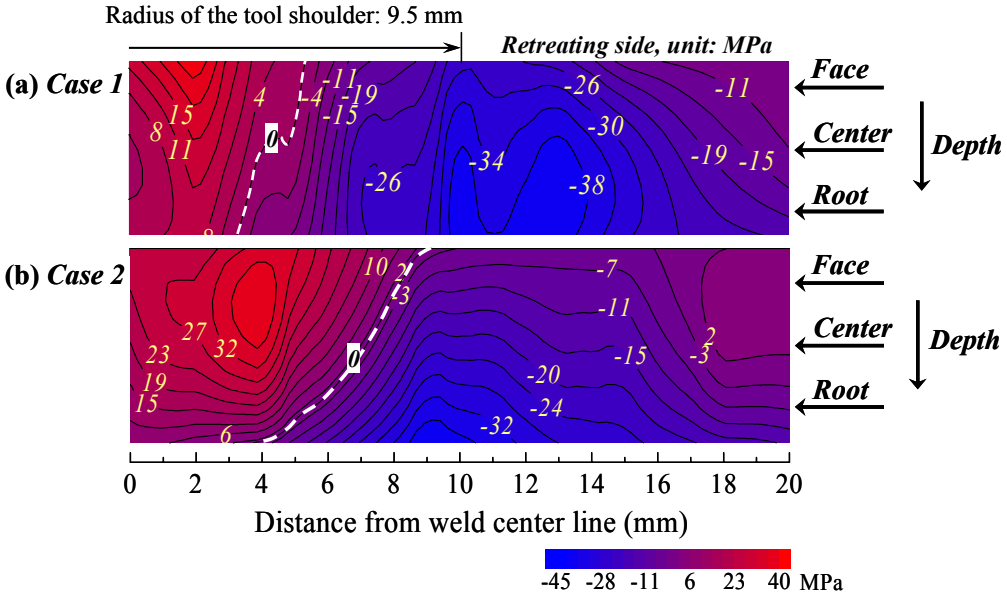

Fig. 4.8. Two dimensional mapping of the transverse residual stress (σ_{yy}) in the FSP plates: (a) *Case 1* and (b) *Case 2*. Note that the dash line indicates the boundary between tension and compression.

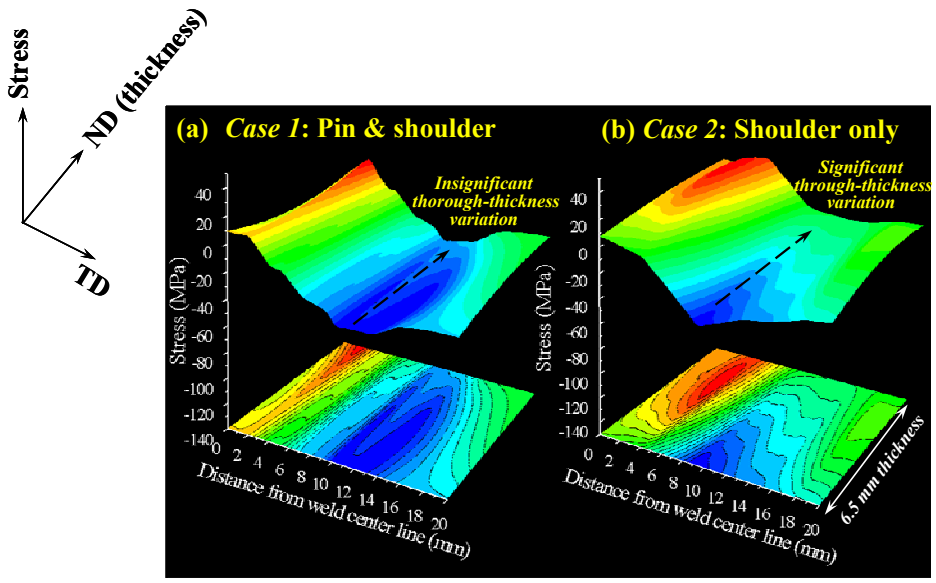

Fig. 4.9. Through thickness variations of the transverse residual stress (σ_{yy}) in *Cases 1* and *2*.

residual stress results and geometric angular distortion, the σ_{yy}, which is considered as the most important component for the angular distortion, was investigated. In fact, the σ_{yy} at *root* of *Case 2* is compressive in the angular distorted plate, Fig. 4.3(b), which does not intuitively agree with the observation of the concave distortion considered as tensile at the *root* of the plate.

The relationship between the residual stress and angular distortion in the FSP could be explained with the aid of the well-known theory by Masubuchi [86]. Figure 4.10 shows the relationship between transient deformations due to the localized heating and transient thermal stresses. Fig. 4.10(a) shows how the heat source on the surface of the plate can cause the angular distortion as a function of time in a rectangular plate without constraints. For example, if all thermal stresses were completely eliminated in an elastic condition, the deflection (δ) follows ABC profile resulting in no angular distortion after the process. However, an inelastic thermal residual stress condition cause a permanent deflection (AB'C' profile) which produces the angular distortion.

For the current FSP, the material expanded during heating (***A*** ~ ***B***) and transient compressive thermal stresses (i.e., thermally-induced residual stresses) could be generated due to the thermal expansion and constraints by the cold material during the FSP, Fig. 4.10(b). It could be noted that the thermal stress can be tensile away from the bead balancing the compression within the bead. Supposing that the *face* of the plate is subjected to a larger thermal flux than the *root*, the magnitude of thermal stress should be nonuniform through the thickness of the plate, which could be the initial source of the angular distortion. During cooling, tensile residual stress could be generated near the centerline (***B*** ~ ***C***) due to the thermal contraction of the bead constrained by the cold

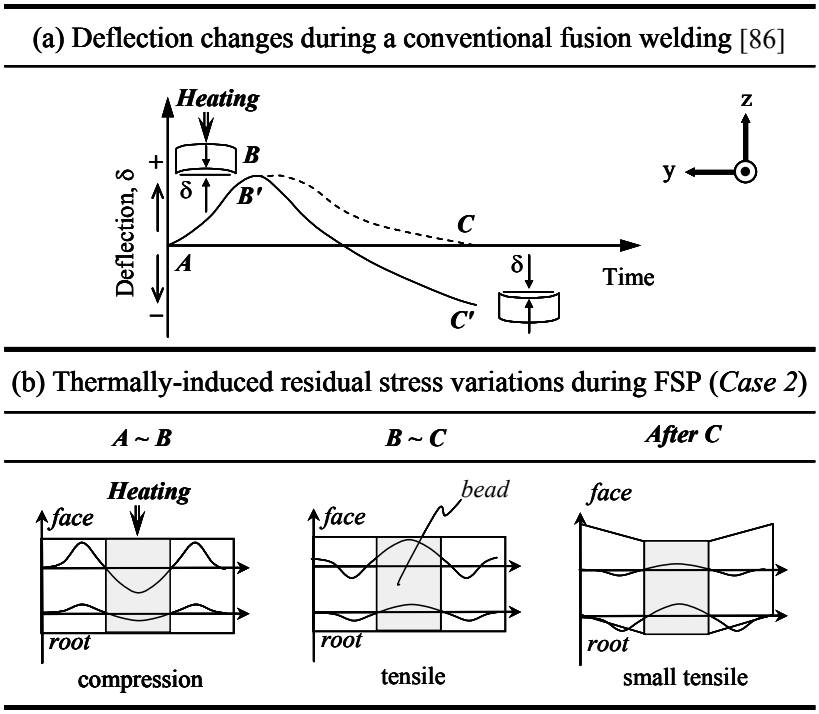

Fig. 4.10. Schematic illustration of the relationship between the transverse residual stresses distribution and angular distortion during FSP.

material again. The asymmetric compressive residual stress distribution through the thickness of the plate in the elastic zone (i.e., outside of the bead) could cause the angular distortion, when the clamps are removed after completely cooling down (after ***C***). In turn, the initial large compressive residual stress at the *face* could be reduced and the compressive residual stress at the *root* enhanced. The final state of the σ_{yy} was measured in Fig. 4.10(b). In summary, the non-uniform thermal distributions in *Case 2* could generate asymmetric through-thickness residual stress variations upon cooling with constraints and distort the plate upon removing the clamps. Finally, the distortion (relaxation) would modify the residual stress in the final components and could be measured by the neutron diffraction experiment.

Chapter V Microstructure, hardness, and natural aging kinetics in a FSP aluminum alloy

5.1. Microstructure and hardness

5.1.1. Objectives

The significant changes in the microstructure, caused by the frictional heat and severe plastic deformation during the FSP, could also be detrimental to the integrity and performance of components [35,36]. One of the most harmful problems could be the residual stress, which has been extensively studied [27-34]. Furthermore, microstructural softening due to the dissolution or growth of strengthening precipitates in FSP-affected regions is a significant and a specific problem for the precipitation-hardenable Al alloys. The reduction of precipitates deteriorates the tensile strength of the FSP-affected region. Sato *et al*. showed the dissolution and growth sequences of precipitates as a function of temperature in 6063 Al alloys subjected to FSW [42,43]. Furthermore, Nelson *et al*. reported that the post weld natural aging can partially restore the tensile strength and alter the failure location due to the change of the location of hardness minimum in an actively-cooled FSW 7075 aluminum alloy [36].

In this chapter, the effects of the stirring pin and the tool shoulder on the microstructural softening during the FSP and the post-FSP natural aging of a 6061-T6 Al alloy will be presented. This includes measurements of the changes in the microstructure and hardness at various locations in the cross-section of the FSP plates as a function of time up to 8 months after the FSP. Furthermore, the effect of the microstructural

softening on the residual strain profiles was examined. Finally, the natural aging kinetics in various regions in the FSP plate was discussed.

5.1.2. Microstructure and hardness analysis

The cross-section of the FSP plate was cut in the middle along the LD for the microstructural characterization, Fig. 3.1(b). The as-received Al plate contains elongated grains having average grain size about 200 μm in the rolling direction with a typical recrystallized rolling texture and precipitate phase. The cross-sectional sample was cold-mounted, ground, polished, and etched with Keller's reagent (150 ml water, 3 ml nitric acid, 6 ml hydrochloric acid, and 6 ml hydrofluoric acid) at room temperature for optical microscopy. In addition, transmission electron microscopy (TEM) observations were performed to investigate precipitates. The disc specimens were prepared by an electrical discharge machining (EDM), mechanical grinding to 100 μm thickness of foil, and electropolishing using a 30% nitric acid solution in methanol, 25 volts for 20 seconds at -30 ℃.

Vickers microhardness (H_v) was measured along the TD on the polished cross-section using 100 gf of applied load. A total of five lines were measured with 0.25 ~ 0.5 mm horizontal spacings and through the thickness of the plate along the middle of the plate thickness (*center*), ±1.26 mm from the middle (*face* and *root*), and ±2.26 mm from the middle (*top* and *bottom*) as shown in Fig. 3.1(c). The changes in Vickers microhardness (H_v) at various locations in the polished cross-section of the FSP plates was examined as a function of time after FSP. In addition, the hardness after fully natural aging was investigated through the thickness of the plate to construct a mapping of the

hardness for *Cases 1* and *2*.

5.1.3. Hardness in *Cases 1* and *2*

Figure 5.1 shows hardness profiles measured along the *face* and *root* in *Case 1*. Also shown in the figure are the contour hardness maps constructed using five hardness measurement lines through the thickness of the cross-section. The hardness profiles were measured after 1 week and 8 months after the FSP. Note that the specimens were kept at the ambient condition after processing. First, the hardness profiles show significant decrease near the bead edge of 60 H_v at 10 mm (FSP-affected zone). It shows a hardness minimum compared to 110 H_v at 20 mm from the centerline (BM), Fig. 5.1(a). The range of the decreased hardness is about ±20 mm from the centerline, which is wider than the bead width (± 10 mm) measured on the surface of the plate. Second, the hardness profiles measured after 8 months, Fig. 5.1(b), show a noticeable change near the centerline compared to the 1-week data from about 70 H_v to 90 H_v. It is important to note that there is little variation through the thickness (i.e., *face* vs. *root*) as shown in Figs. 5.1(a) and 5.1(b). Finally, the hardness contour map shows the two-dimensional variation of the hardness after the FSP. The contour map in Fig. 5.1(a) shows a wider blue region near the bead due to the decreased hardness, and Fig. 5.1(b) shows clear boundaries at the edge of the bead due to the increased hardness within the DXZ after 8 months of the FSP.

Figure 5.2 shows the comparison of hardness profiles measured along the *face* and *root* after 1 week and 8 months of the FSP of *Case 2*. First, the hardness decreases near the bead, Fig. 5.2(a), which is similar to *Case 1*, Fig. 5.1(a). It indicates that heat alone by the tool shoulder (e.g., *root* of *Case 2*) induces the significant decrease of the

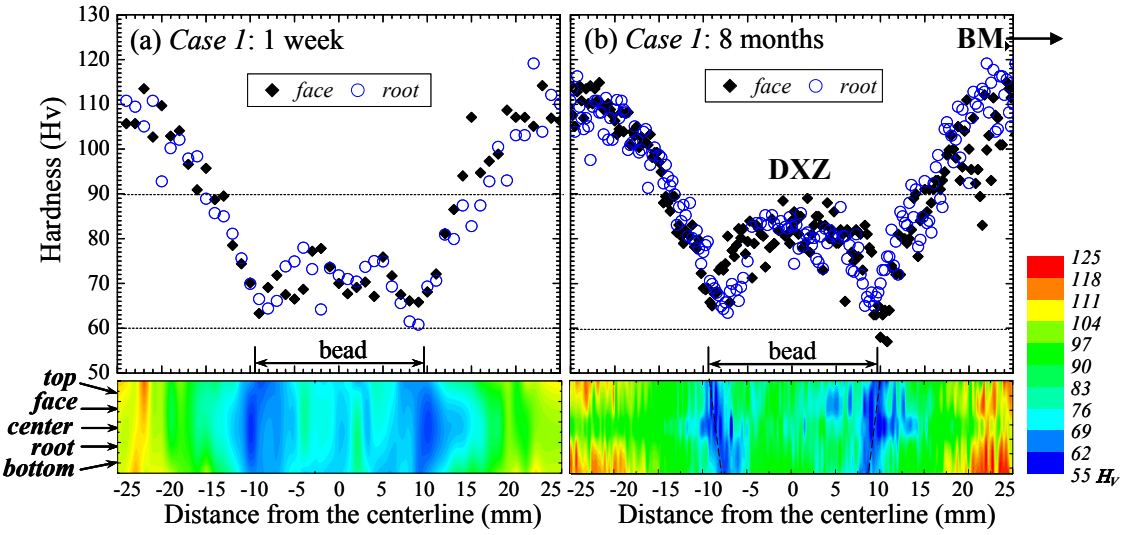

Fig. 5.1. Hardness profiles measured along the *face* and *root* in *Case 1* and hardness contour maps constructed using five hardness profile lines measured throughout the thickness: (a) 1 week and (b) 8 months after the FSP.

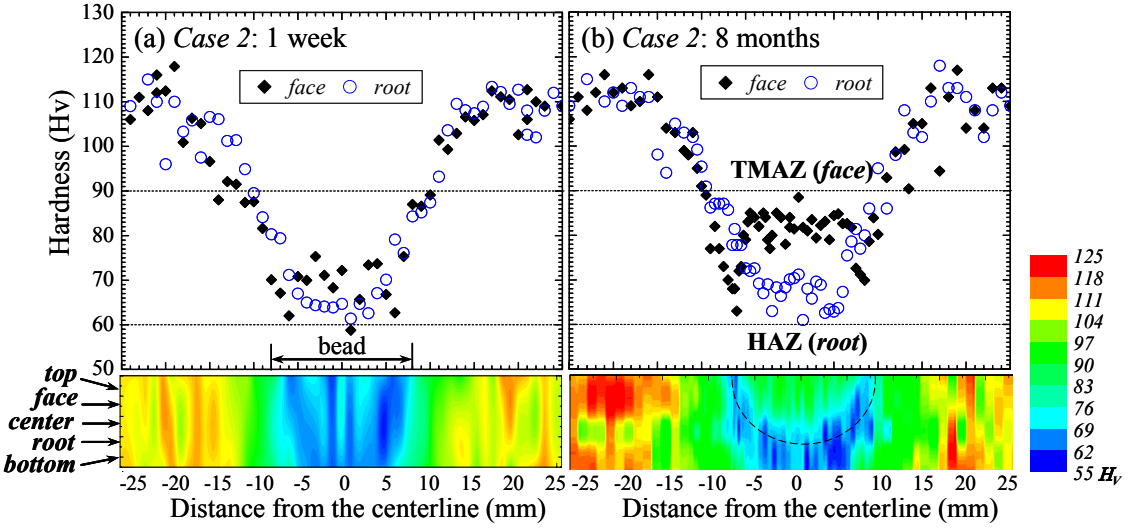

Fig. 5.2. Hardness profiles measured along the *face* and *root* in *Case 2* and hardness contour maps: (a) 1 week and (b) 8 months after the FSP.

hardness in the FSP-affected zone. Second, the increased hardness within the bead area after 8 months, which was observed throughout the thickness in *Case 1*, is only seen near the *face* in *Case 2* causing a significant difference in the hardness profiles between the *face* and *root*. Finally, the contour maps clearly show the decreased hardness in the FSP-affected zone after 1 week, Fig. 5.2(a). The increased hardness at the upper part of the plate creates an apparent bright half-circle boundary, indicating through thickness variation of the hardness after 8 months, Fig. 5.2(b).

5.1.4. Microstructure analyses

Figures 5.3 and 5.4 show TEM bright-field images of *Cases 1* and *2*, which were measured after 8 months after the FSP. Figure 5.3(a) shows TEM bright-field images of *Cases 1* and *2*, which were measured 8 months after the FSP. To understand the aging responses TEM images were investigated in each specific position such as BM, DXZ in *Case 1* and HAZ (*root*), TMAZ (*face*) in *Case 2*. In detail, four types of precipitates are reported in the FSW precipitate-strengthened 6xxx aluminum alloys (Al-Mg-Si system) [42,88]: pin dot-like precipitate (spherical Guinier-Preston-I zone), fine needle-shaped precipitate (β'' or Guinier-Preston-II zone), rod-shaped precipitate (β'), and coarse equilibrium precipitate (platelet or spherical β). Figure 5.3(b) shows the microstructure in the BM of *Case 1*, which was taken 30 mm away from the centerline. It shows a high density of the needle-shaped precipitates (typically about 7 nm Φ × 200 nm L, Widmanstätten structure) effective for the strengthening and the coarse (about 125 nm Φ) spherical precipitates, which is a typical microstructure of an as-received 6061-T6 aluminum alloy [88]. Figure 5.4(a) exhibits the dissolution of the needle-shaped

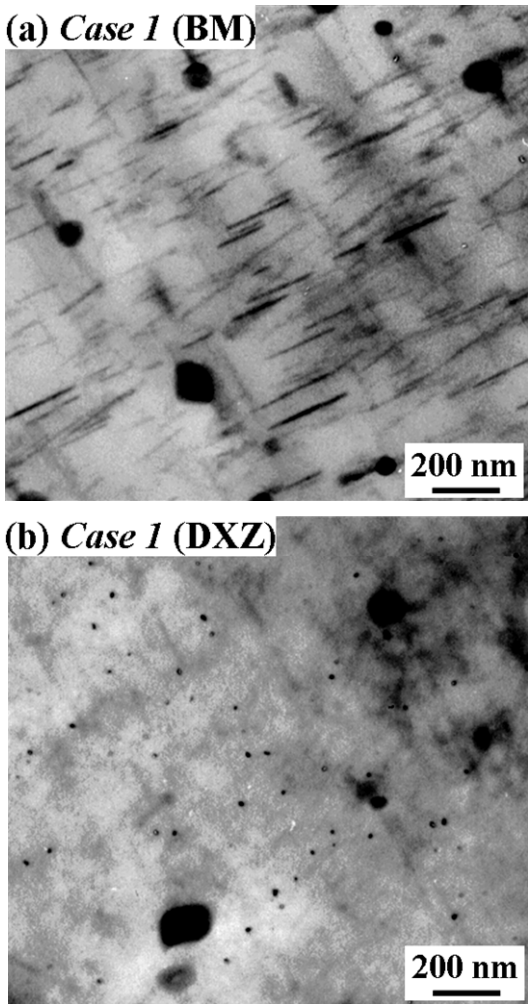

Fig. 5.3. TEM bright-field images measured 8 months after the FSP: (a) BM, (b) DXZ of *Case 1* (as marked in Fig. 5.1b)

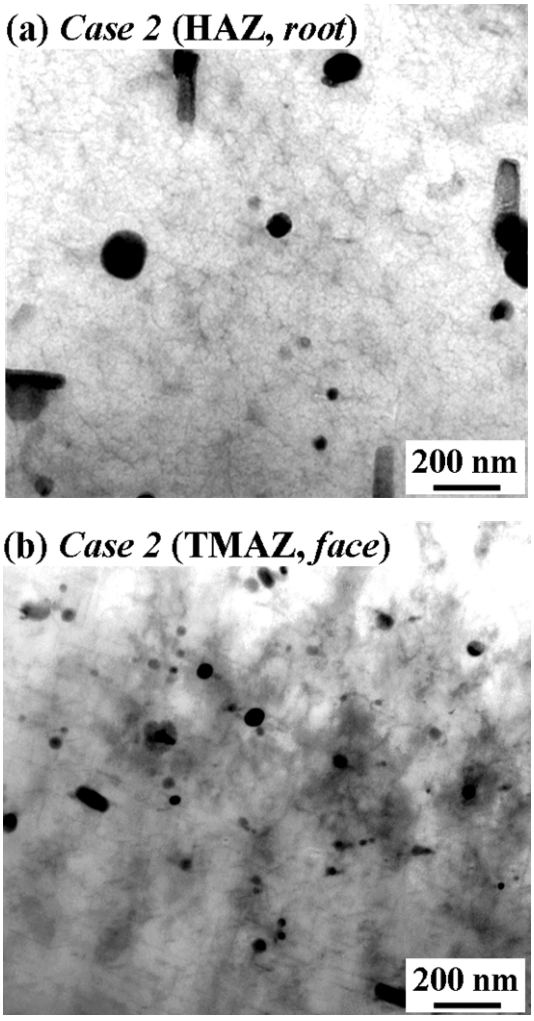

Fig.5.4. TEM bright-field images measured 8 months after the FSP: (a) HAZ (*root*), (b) TMAZ (*face*) of *Case 2* (as marked in Fig. 5.2b).

precipitates but appearance of new fine pin dot-like precipitates (about 5 nm Φ) in the DXZ of *Case 1*, which is also known to increase the hardness [42,89]. Figure 5.4(b) shows dissolution of the needle-shaped precipitates and a growth of thick plates at the interface of the coarse spherical particles in the HAZ (*root*) of *Case 2*. Figure 5.4(b), at the TMAZ (*face*) of *Case 2*, also shows dissolution of the needle-shape precipitates and re-precipitation of particles whose morphology is quite similar to the pin dot-like precipitates in the DXZ of *Case 1*. Overall, the coarse spherical particles did not seem to be affected by the softening and aging process after the FSP. These microstructures are related to the variation of the hardness in *Cases 1* and *2* and discussed in the following sections.

5.2. Microstructural softening

Typically, the size of precipitates in the FSW precipitate-strengthened 6xxx aluminum alloy (Al-Mg-Si system) were reported: pin-dot like precipitate (GP zone), needle-shaped precipitate (β'', 20 ~ 50 nm), and rod-shaped precipitate (β', 50 ~ 700 nm) [42,43]. The dissolution or growth of the precipitates during FSP can cause the microstructural softening since the strength of 6xxx aluminum alloys mainly depends on the density of needle-shape precipitate (β''). Considering the solvus temperature of the β'' (about 353 ºC), the microstructure analyses (the dissolution or growth of β'') under the current processing conditions and the peak temperature during the FSP can provide the possibility of the microstructural softening of the age-hardenable aluminum alloys [35].

The dissolution of β'' was observed under the current processing condition as revealed by comparison of Figs. 5.3(a) and 5.4(a). Note that the peak temperature measured during the FSP using thermocouples attached to the surface of the plate was about 360 ºC. Considering the solvus temperature of the β'' (below 353 ºC), the temperature inside the material during the FSP can be high enough to dissolve the initial strengthening precipitates (β''), resulting in the microstructural softening for the precipitation-hardenable 6061-T6 Al alloys [89]. Furthermore, the microstructural softening due to the precipitate dissolution is clearly manifested by the significant hardness decreases near the FSP-affected zone in both *Cases 1* and *2*, Figs. 5.1(a) and 5.2(a). A maximum decrease of about 50 H_v (about 45% reduction of the hardness) was observed within about ± 20-mm from the centerline after 1 week compared to the as-received state. Comparison of the hardness profiles of *Cases 1* and *2* shows that microstructural softening can be caused by the tool shoulder alone. It is interesting to note that the softening was also found in the *root* of *Case 2*, which was subjected only to the heating caused by the tool shoulder. Thus, the hardness results suggest that the frictional heating by the tool shoulder is sufficient to cause the microstructural softening without the severe plastic deformation (and additional heating) by the stirring pin during the FSP.

5.3. Softening effect on residual strain profile

The longitudinal residual strain component was presented and the influence of microstructural softening was investigated. Figure 5.5 shows longitudinal residual strains

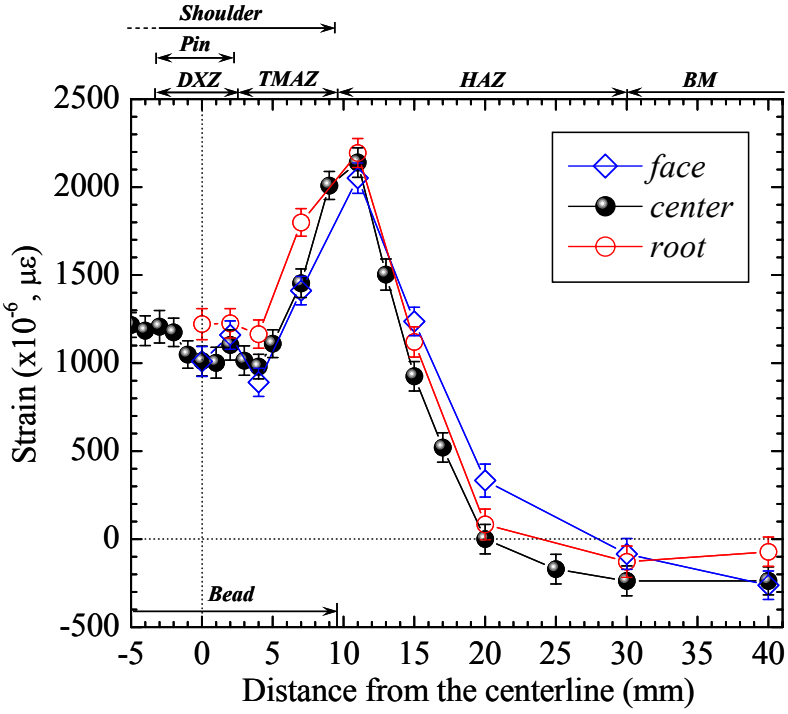

Fig. 5.5. Longitudinal residual strains (ε_{xx}) of *Case 1* measured after 1 week of the FSP. The *face* and *root* profiles were measured at 1.26 mm above and below the *center* on the retreating side as shown in Fig. 3.1(b)

(ε_{xx}) measured along the *face, center,* and *root* on the retreating side of *Case 1*, Fig. 3.1(b), using neutron diffraction, 1 week after the FSP. The ε_{xx} measured along the *center* shows a small compressive strain until 20 mm away from the centerline. The ε_{xx} increases to a maximum tensile strain of about 2,100 x 10^{-6} (or με) near the TMAZ/HAZ interface, drops significantly at the TMAZ boundary, and fluctuates between 980 ~ 1,200 με in the DXZ within the bead. Overall, the characteristic peak-and-valley shape of ε_{xx} profile is consistent with the literature [34,63]. The reduction of residual strain profiles near the bead in *Case 1* was observed in previous neutron-diffraction studies [87] . Such reduction of the residual strains is related to the decreased yield strength (microstructural softening) in the bead area due to the dissolution (or growth) of the strengthening precipitates caused by the frictional heat from the tool shoulder during the FSP. In addition, the ε_{xx} profiles at the *face, center,* and *root* are quite similar, i.e., there are no significant through-thickness variations. Furthermore, the diameter of the shoulder (and the bead) is similar to the width of the reduction in the residual strain profiles, which is consistent with the hardness reduction shown in Fig. 5.1(a). The uniform softening in *Case 1* is due to the stirring pin acting as an additional heat source and heat transfer medium which also causes uniform decrease in hardness and residual strain profiles through the thickness of the plate.

To verify the potential influence of chemical composition changes on the d_o changes in the current study, the d_o was carefully measured using coupons (2 x 2 x 2 mm^3) machined from the FSP plate using EDM to relieve the macroscopic residual stresses. Figure 5.6 shows d_o results from the LD measurements using the Al 200

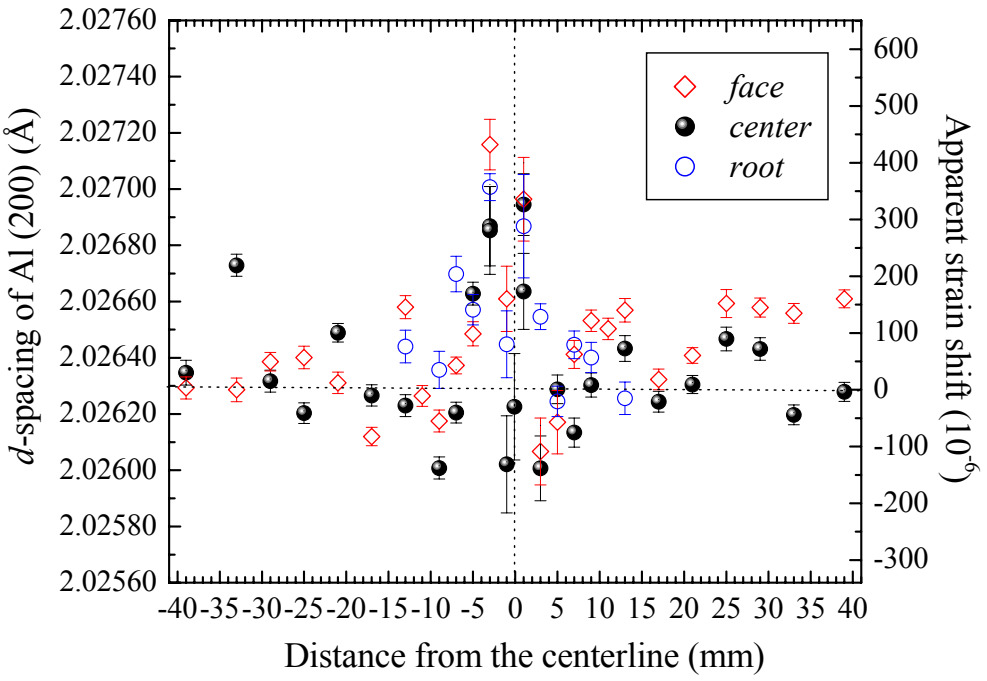

Fig. 5.6. Stress-free *d*-spacing (d_o) variation as a function of distance from the centerline. Longitudinal component of d_o was measured using 2 x 2 x 2 mm^3 coupons machined from the FSP plate and corresponding apparent strain shifts were estimated.

reflection. The d_o changes near the centerline are significant indicating a 0.001 Å variations in the *d*-spacing, which corresponds to about ± 280 με of apparent strain shifts. Note that, for the current study, the residual strain profiles presented in Fig. 5.5 were not noticeably changed when corrected by the measured d_o.

5.4. Natural aging kinetics

5.4.1. Natural aging and kinetics after FSP

Natural aging is known as a precipitation hardening phenomenon at room temperature after solution heat-treatment processing [90-93]. The rapid cooling from a temperature above the solvus temperature creates a supersaturated solid solution and facilitates the re-precipitation with time. The mechanical properties can be significantly altered during the post-FSP natural aging [43]. Nelson *et al*. reported that the post weld natural aging can partially restore the tensile strength and alter the failure location corresponding to the change of the hardness minimum in an actively-cooled FSW 7075 aluminum alloy [36]. Thus, kinetics of the natural aging should be examined by observing the hardness changes as a function of time for a long period. To study the natural aging kinetics of the characteristic regions (i.e., DXZ, TMAZ, and HAZ), the hardness variation during natural aging can be modeled by an equation [91]:

$$H_V = A + B \log t \tag{11}$$

where A is temperature-dependent rate constant (H_v), B is the regression coefficient depending on the solution-heat-treatment temperature (H_v/log hour).

5.4.2. Comparison among the DXZ, TMAZ, and HAZ in *Case 1*

Figure 5.7 shows the kinetics of the natural aging, which was examined by observing the hardness changes as a function of time. The hardness was measured 4 hours, 1 week, 2 weeks, 3 weeks, and 8 months after the FSP for *Case 1*, Fig. 5.1. Note that the hardness was measured within ± 3, ± 4~7, ± 8~12-mm positions along the *center* (marked as short horizontal lines in Fig. 4.1) to study the natural aging kinetics of the DXZ, TMAZ, and HAZ, respectively. The hardness values were averaged for a given time and fitted to a linear model using the least squares method. The hardness variation during natural aging can be modeled by an equation Eq. (11). The coefficients of the hardness evolution during the natural aging of the FSP 6061-T6 Al alloy (*Case 1*) is summarized in Table 5.1.

The aging behavior of the DXZ is similar to the TMAZ exhibiting a significant increase in hardness with time, but is clearly different from the HAZ, Fig. 5.7. First, more significant softening was found in the DXZ and TMAZ than the HAZ after 4 hours of the FSP. It has been reported in the literature [36,43] that the softening in the DXZ and TMAZ is mainly related to the complete dissolution of needle-shape precipitates (β''), while the softening in the HAZ is due to the partial dissolution of β'' and the growth of the rod-shape precipitates (β'). Subsequently, the natural aging (hardness increases with time) observed in the DXZ and TMAZ is due to the re-precipitation of the pin-dot like precipitates observed in Fig. 5.3(b), while the HAZ remained unchanged. The slopes of the kinetic equation were estimated as 4.3 (DXZ), 3.0 (TMAZ), and ~0 (HAZ) H_v/log hour, Table 5.1. The reasons for the (faster) aging in the DXZ and TMAZ than in the HAZ of *Case 1* may be due to the partially solution-heat-treated condition at the higher

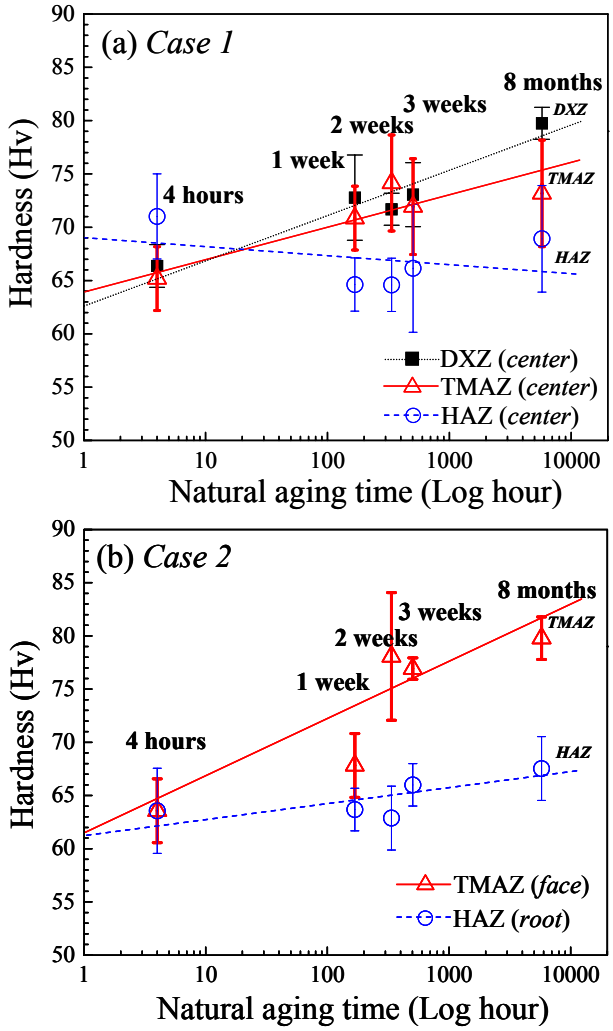

Fig. 5.7. Hardness evolution during the natural aging: (a) DXZ, TMAZ, and HAZ in *Case 1* (typical FSW) and (b) TMAZ (*face*) and HAZ (*root*) in *Case 2* (shoulder only) after 4 hours, 1 week, 2 weeks, 3 weeks, and 8 months of the FSP 6061-T6 Al alloy. The precise positions of the hardness measurements are marked as short lines in Figs. 4.1 and 4.2. The error bars in the hardness data represent the spread of the hardness values within each zone.

Table 5.1. Natural aging kinetics of various regions in the FSP. *A* (intercept constant in H_v) and *B* (slope coefficient in H_v/log hour) were obtained by the linear fitting of the measured hardness data.

Zone	***Case 1*** **A / B**	**Zone**	***Case 2*** **A / B**
DXZ	63 / 4.3	DXZ	-
TMAZ	64 / 3.0	TMAZ	61 / 5.4
HAZ	69 / - 0.9	HAZ	61 / 1.5

peak temperature in the DXZ and TMAZ than in the HAZ [90]. Furthermore, the refined grains (increased grain boundaries) caused by the recrystallization in the DXZ and the increased dislocation density in the TMAZ during the FSP may result in high diffusivity paths for the solute atoms facilitating faster re-precipitation [93]. In addition, supposing the higher peak temperature in the DXZ and TMAZ than in the HAZ during the FSP, more excess vacancy concentration may have been provided during the rapid cooling, resulting in a faster diffusion [36,92].

5.4.3. Comparison between *Case 1* and *Case 2*

Figure 5.7(b) shows the natural aging kinetics of the TMAZ (*face*) and HAZ (*root*) in *Case 2*. Note that the hardness measurement positions for the aging kinetics studies are marked with short horizontal lines in Fig. 4.2. Figure 5.7(b) shows faster hardness increases in the TMAZ (*face*) than in the HAZ (*root*) with the slopes of 5.4 and 1.5 H_v/log hour, respectively, Table 5.1. The aging kinetics of the TMAZ (*face*) in *Case 2* is similar to the DXZ and TMAZ in *Case 1*, which is due to the re-precipitation of the fine pin-dot like particles as shown in Fig. 5.3(b). On the other hand, the absence of the re-precipitation of needle-shape precipitates and pin dot-like precipitates in the HAZ (*root*) in *Case 2*, Fig. 5.4(a), is consistent with the marginal natural aging observed in Fig. 5.7(b). The results show that the frictional heating from the tool shoulder causes significant natural aging only near the top surface of the FSP plate in *Case 2*, while the combination of the tool pin and the tool shoulder in *Case 1* results in a more uniform aging behavior through the thickness of the FSP plate. In summary, as schematically shown in Fig. 5.8, the results in the present study provide the softening and aging

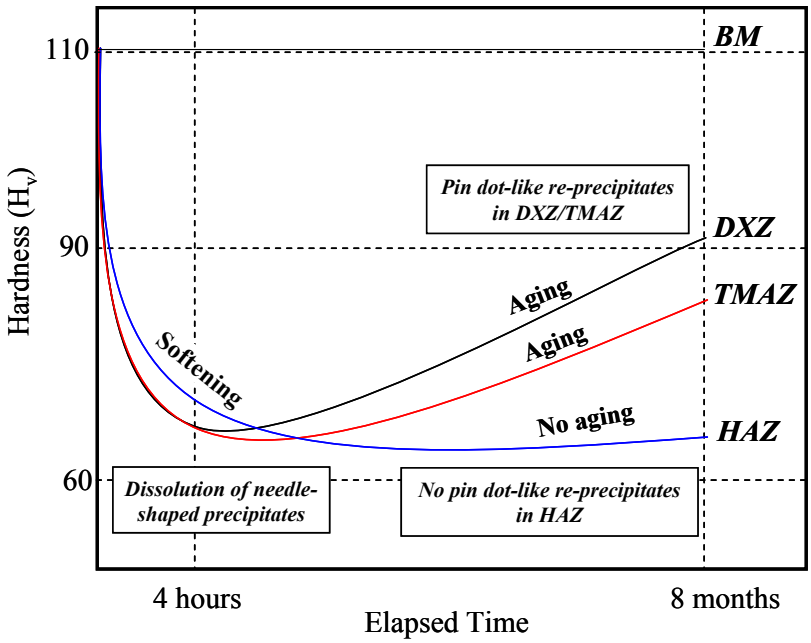

Fig. 5.8. Schematic illustration of the softening and natural aging sequence in the characteristic regions of the friction-stir processed 6061-T6 Al alloy.

sequence in the DXZ, TMAZ, HAZ, and BM of the FSP. Hardness variation as a function of elapsed time after the FSP can suggest the microstructural softening and natural aging behavior. Furthermore, it was verified by the dissolution and re-precipitations of strengthening precipitates in each characteristic region of the FSP Al alloy.

Chapter VI Texture in a FSP aluminum alloy

6.1. Texture measurements and analyses

6.1.1. Objectives

The frictional heating and severe plastic deformation necessary for the joining also generate significant residual stresses. The influence of the frictional heating and severe plastic deformation on the residual strains in a FSP 6061-T6 aluminum alloy was reported previously [62]. Furthermore, during FSW the crystallographic texture can be significantly altered from the original rolling texture in aluminum-alloy [46-50] or magnesium-alloy [51,52] plates, which could significantly affect the physical and mechanical properties. Fonda *et al.* showed, based on the crystallographic texture analysis of a Al 2519 FSW, that the texture variation is significant across the boundary between the TMAZ and HAZ due to macroscopic rigid-body rotations of the grains around the stirring pin of the FSW tool [46,47]. Sato *et al*. reported about 40-degree rotation of the <111> texture in the weld center after a postweld heat treatment [48]. They suggested that the texture variation during the FSW is due to the dynamic recrystallization of the thermally-unstable center region. Using electron backscattered diffraction (EBSD), Field *et al.* showed that severe gradients in crystallographic texture exist through the thickness and across the width of FSW [49]. Finally, Park *et al.* reported that the texture variation can strongly affect the tensile properties in FSW AZ61 magnesium alloy [51,52]. In the current literature, severe plastic deformation is considered as the main source of texture alteration during the FSW. However, direct experimental evidence is not available to date.

Neutron diffraction is well suited for spatially-resolved measurements of the strain and texture in the bulk material due to the deep penetration of neutrons into most engineering materials (e.g., a 7 cm thick aluminum plate will reduce the transmitted intensity of the incident beam by 50 %) and the capability to distinguish phases and crystal planes. Bulk texture measurements using the neutron time-of-flight technique and multiple detector system proved to be very efficient [94,95]. For example, Carr *et al.* recently reported quantitative texture variations in a zircaloy-4 weld using neutron diffraction [24].

In this chapter, neutron diffraction results are presented: (1) volume-averaged textures measured from the base material, HAZ, and TMAZ/dynamic recrystallized zone (DXZ); and (2) spatially-resolved texture measurements using the changes in the reduced peak intensity at various locations across the centerline and through the thickness of the FSP 6061-T6 aluminum alloy plate. Finally, the main cause of the changes in the initial recrystallized rolling texture of the plate during the FSP was identified.

6.1.2. Orientation distribution functions (ODFs) and Pole figure texture analyses

Texture measurements using neutron time-of-flight (TOF) diffraction [15] is a well-established technique [94-98]. Neutron diffraction measurements were performed using the HIPPO (High Pressure Preferred Orientation) diffractometer [94,95] at Los Alamos National Laboratory, Fig. 6.1. A total of three coupons were cut out from each plate with the dimensions of 10 (x) × 10 (y) × 6.5 (z) mm^3. The center positions of the three coupons are at 0, 15, and 35 mm away from the centerline on the retreating side, marked ***C***, ***B***, and ***A*** coupons, respectively, as shown in Fig. 3.1(d). The measurement

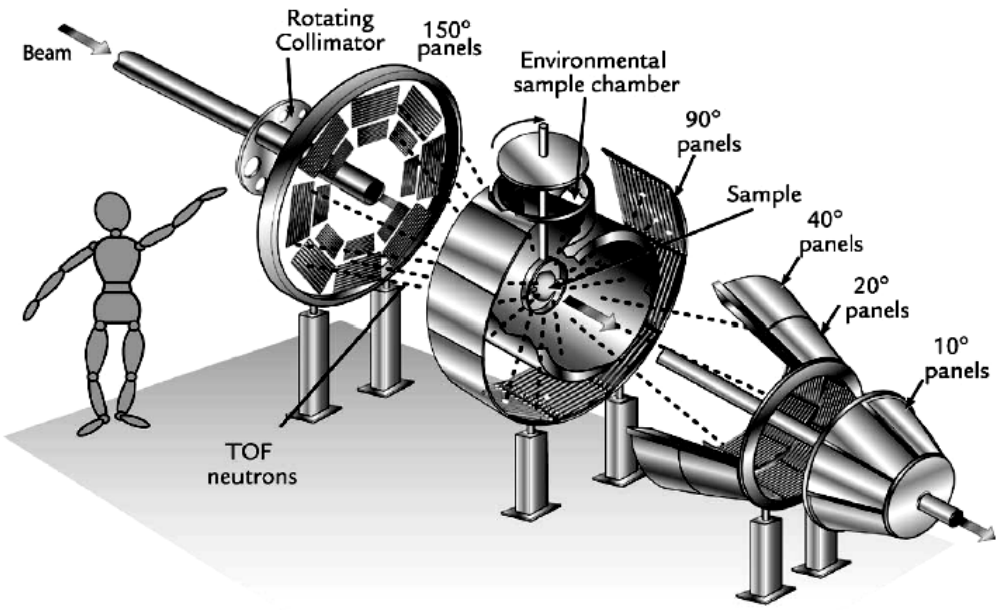

Fig. 6.1. Schematic view of the HIPPO diffractometer

(Wenk HR *et al*., Nuc Instrum Meth A 2003;515:575 [94])

time for each coupon was 16 minutes due to the high count rates with three banks of a total of 30 detector panels arranged on rings in the HIPPO instrument. Details of the HIPPO instrument and texture measurement schemes can be found elsewhere [94,95]. Each coupon was rotated into four different orientations (0º, 45º, 67.5º, and 90º) to enhance the coverage of the pole figures, providing 120 histograms. Note that the coordinate axes of pole figures are the same as those of the plate sample (i.e., LD, TD, and ND of the plate) shown in Fig 3.1(a).

For the texture analysis, the TOF diffraction data was analyzed using the Rietveld structure refinement method, which is a method for the whole pattern adjustment between the intensities of the peaks in the measured pattern and calculated intensities based on the crystallographic space group [96]. To perform the Rietveld texture analysis, the GSAS software package was used to analyze 98 selected histograms from each specimen [85]. A precise fitting of the peak positions and widths was achieved using the spherical harmonics model during the Rietveld refinement [97]. Three individual complete pole figures at an interval of 5º x 5º along the polar and azimuthal angles are generated from the time-of-flight spectra. The orientation distribution functions (ODFs), presented by the three Euler angles (i.e., ϕ_1, ϕ, ϕ_2) in Bunge's notation, are obtained from the three pole figures by using popLA software [99].

6.1.3. ODFs and Pole figure texture measurements

Figure 6.2 shows the ODF sections measured using the HIPPO instrument from the three coupons prepared from *Cases 1* and *2*. First, the textures were analyzed with the help of ODF determined by the series expansion method, since the ODF exhibits the

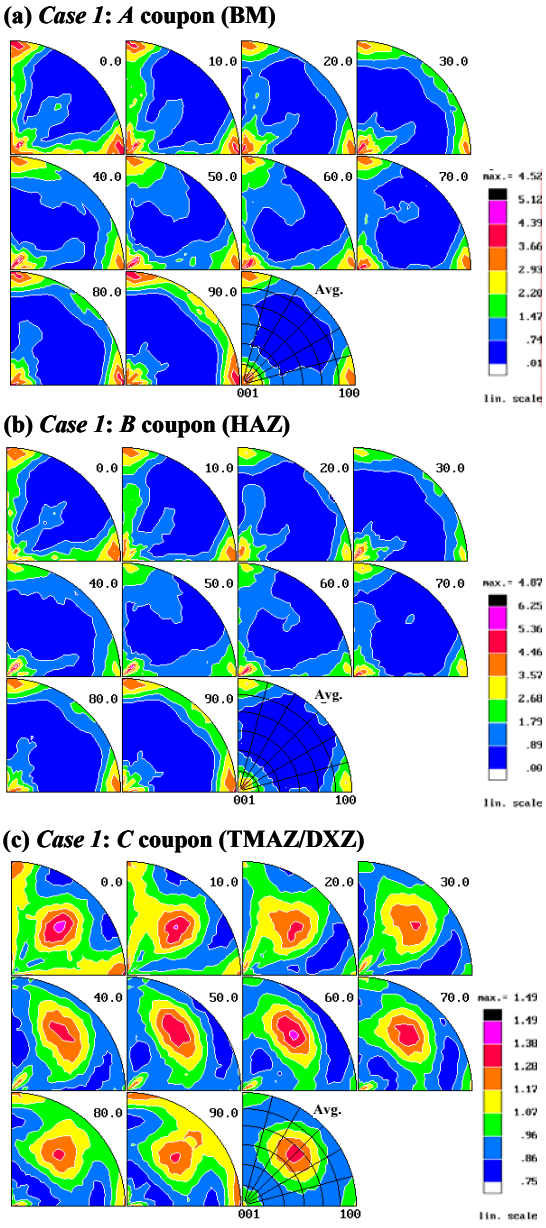

Fig.6.2. ODFs of *Case 1*: (a) ***A*** coupon (BM: base material), (b) ***B*** coupon (HAZ: heat-affected zone), (c) ***C*** coupon (TMAZ/DXZ: thermo-mechanically affected zone and dynamic recrystallized zone)

higher resolution than the pole figure for the interpretation of the texture [98]. Note that the ***A***, ***B***, and ***C*** coupons are marked with dotted squares in Fig. 3.1(d) and mainly cover the BM, HAZ, and TMAZ/DXZ, respectively. The texture can be usually labeled as {*hkl*}<*uvw*>, where {*hkl*} is crystallographic plane perpendicular to the LD and <*uvw*> is the crystallographic direction parallel to the ND. Figure 6.2 shows the ODFs of *Case 1*. The texture from the ***A*** coupon (BM) and ***B*** coupon (HAZ), Figs. 6.2(a) and 6.2(b), shows the strong cube or mixed cube and Goss texture, which is known as a typical recrystallized rolling texture of Al alloy plates, Fig. 6.3, [48,98]. On the other hand, the ODF of the ***C*** coupon (TMAZ/DXZ) shows a significantly different texture, Fig. 6.2(c). It shows a shear texture in the DXZ of the FSP, also known as the rotated ideal simple-shear texture in the fcc metals [46,98]. For *Case 2* Figs. 6.4 show the cube, Goss, and weak shear textures in the ODFs of the three coupons. Overall, the texture results of *Case 2* show little qualitative changes at the three different regions unlike *Case 1*.

Figure 6.5 shows the (200), (220), and (111) pole figures from *Case 1*. The texture from the ***A*** coupon (BM) shows a strong (200) preferred orientation along the LD and ND. Note that pole densities are given in multiples of random distribution (m.r.d.) for LD, TD, and ND in Fig. 6.5. The (200) pole figure of the ***B*** coupon (HAZ) is similar to the ***A*** coupon. For example, the maximum 3.8 m.r.d. of (200) pole figure in the ***B*** coupon (HAZ) is comparable to the ***A*** coupon (BM). On the other hand, the pole figures of the ***C*** coupon (TMAZ/DXZ) show a different texture compared ***A*** coupon (BM). The texture of (200) pole figure is significantly weaker compared to the other coupons and is rotated about 40 degrees to the counter-clockwise direction around the LD axis. It should be noted that a weak texture appears along the ND in the (111) pole figure of the ***C*** coupon

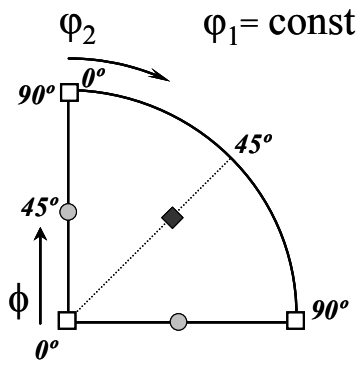

		hkl	*uvw*
□	cube	{001}	<100>
○	Goss	{011}	<100>
◆	Shear {111}	{223}	<1-10>

Fig. 6.3 A diagram for the texture interpretation of the ODFs

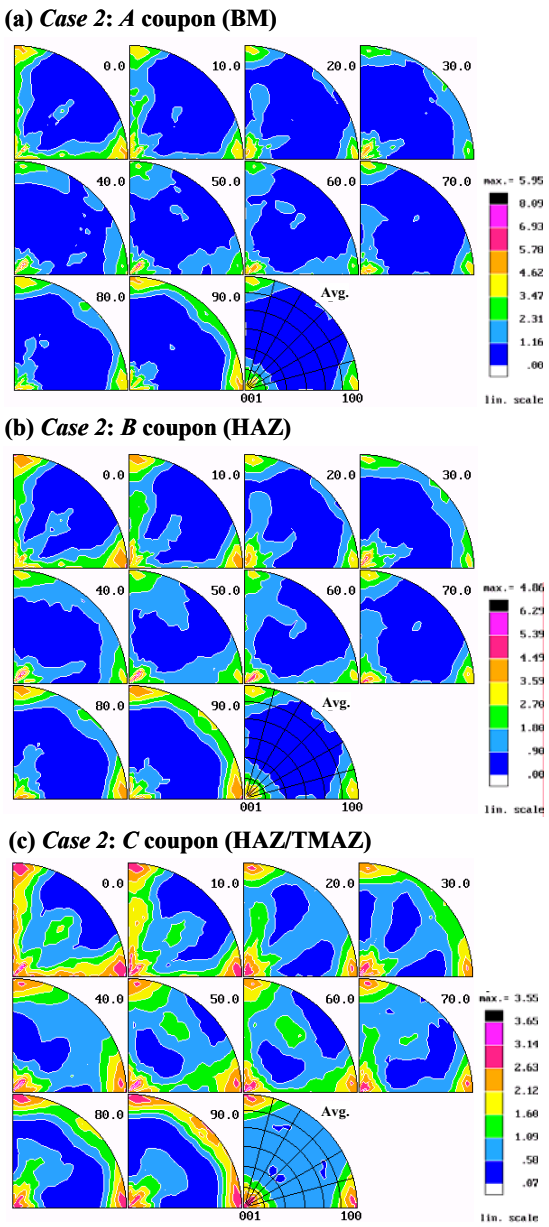

Fig. 6.4. ODFs of Case 2: (a) ***A*** coupon (BM), (b) ***B*** coupon (HAZ), (c) ***C*** coupon (HAZ/TMAZ)

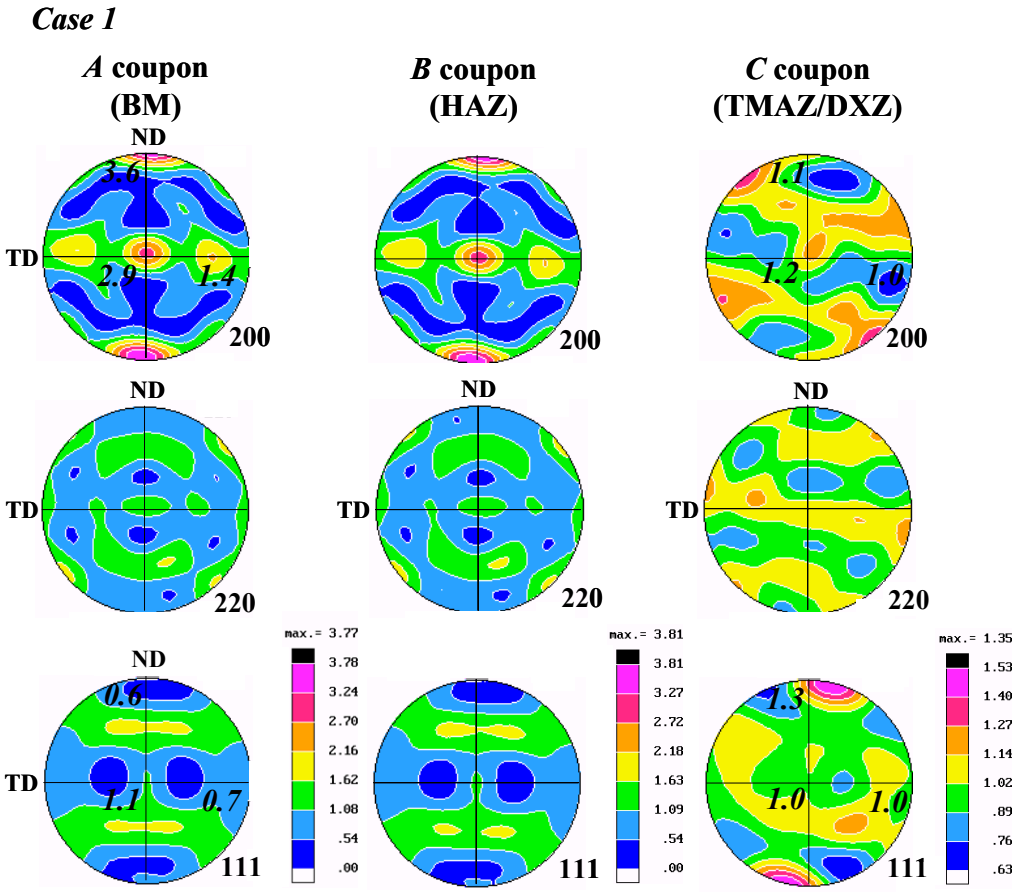

Fig. 6.5. (200), (220), and (111) pole figures measured in *Case 1*, from ***A*** coupon (BM: base material), ***B*** coupon (HAZ: heat-affected zone), and ***C*** coupon (TMAZ/DXZ: thermo-mechanically affected zone and dynamic recrystallized zone). Note that all pole figures are drawn on a common scale of multiples of random distribution (m.r.d).

with the maximum of 1.4 m.r.d., which is rotated approximately 10 degrees clockwise around the LD axis.

Figure 6.6 shows the (200), (220), and (111) pole figures of *Case 2*. First, in both ***A*** and ***B*** coupons, a strong (200) preferred orientation was observed along the LD and ND, which is qualitatively similar to the results of *Case 1*. However, the ***C*** coupon of *Case 2* shows almost no variation in the texture unlike the ***C*** coupon of *Case 1*, which showed considerable changes in the texture. It should be pointed out that the ***C*** coupon of *Case 2* partially include the TMAZ at the upper part (*face*) of the specimen as shown in the macrostructure, Fig. 4.2. Indeed, the maximum (200) pole density weakens from 4.1 m.r.d. in the A coupon to 2.9 m.r.d. in the ***C*** coupon due to the volume averaging of the *face* (TMAZ) and *root* (HAZ) regions data in *Case 2*.

6.2. Reduced intensity

6.2.1. Diffraction measurement and analysis

Spatially-resolved neutron-diffraction measurements can also provide quantitative insights to the texture variations [24]. The SMARTS instrument was used to measure diffraction from the grain set with their reflecting *hkl* lattice plane normal oriented parallel to LD, TD, and ND [17]. Note that the intensity values are corrected for the unequal background intensity measured from different positions to present on a common scale. In each scan set, approximately 40 locations were measured along the middle of the plate thickness, 1.26 mm above the middle, and 1.26 mm below the middle, namely *center*, *face*, and *root* scans, respectively, Fig. 3.1(b). The integrated intensities of multiple reflections were obtained using the single peak fitting method in the

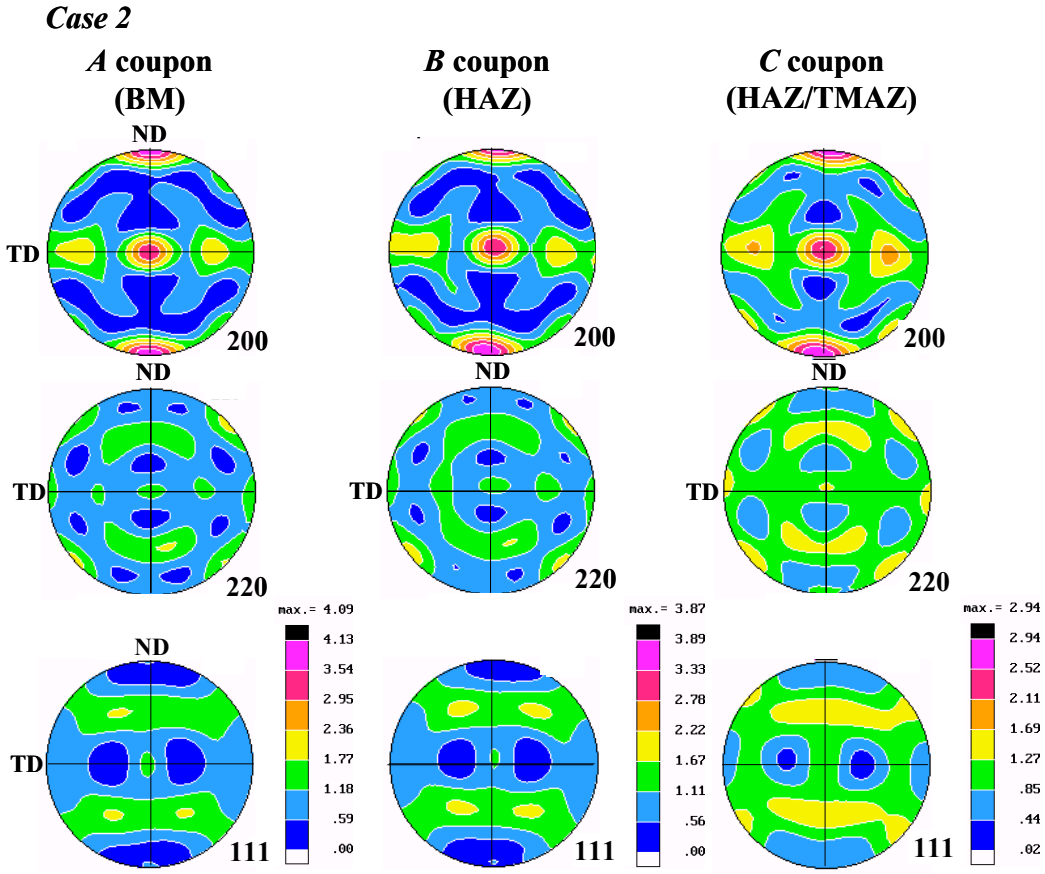

Fig. 6.6. (200), (220), and (111) pole figures measured in *Case 2* from ***A*** coupon (BM), ***B*** coupon (HAZ), and ***C*** coupon (HAZ/TMAZ).

GSAS [85] and (200), (220), and (111) results are presented here.

The intensity of a diffraction peak is related to the texture. The height of the peak is not a reliable intensity and the integrated intensity (I_τ) is used in this study. Specifically, the "reduced intensity" is proportional to the number of unit cells oriented to satisfy Bragg's law within the scattering volume. First, the I_τ of a diffraction peak observed in the TOF diffraction pattern is given by [15]:

$$I_\tau(\delta t) = n_L(\lambda)\delta\lambda N_s\left(\frac{d\sigma}{d\Omega}\right)\Delta\Omega^* \tag{12}$$

where δt is the time channel, $n_L(\lambda)$ is the incident intensity per unit wavelength range, $\delta\lambda$ is the wavelength interval, N_s is the number of scattering unit cells, and $\Delta\Omega^*$ is the counter solid angle corresponding to $2\pi sin\theta\Delta 2\theta f$, ($2\theta$ is the scattering angle, $\Delta 2\theta$ is the spread scattering angle, and f is the fraction of the Debye-Scherrer cone intercepted by the counter). Finally, ($d\sigma/d\Omega$) is the differential cross-section integrated over the reflection of the total cross-section:

$$\left(\frac{d\sigma}{d\Omega}\right) = \frac{1}{32\pi}\frac{\lambda^4 Z_\tau}{V_{cell}\sin^3\theta}\frac{1}{\delta\lambda}\left|F(\tau)\right|^2 \tag{13}$$

where λ is the wavelength, Z_τ is the multiplicity of the reflection, V_{cell} is the volume of scattering unit cell, $\delta\lambda$ is the wavelength interval, and $F(\tau)$ is the structure factor. Combining the equations (12) and (13) yields:

$$I_{red} \propto \left(\frac{1}{\sin^2\theta}\right)\left(\frac{N_s}{V_{cell}}\right) \tag{14}$$

Here, I_{red} is proportional to the number of the scattering unit cells (N_s). The reduced intensity can be obtained for each reflection by dividing the measured intensities by the

proper terms, i.e., λ^4, Z_τ, and $F(\tau)^2$ that vary for each reflection in Eq. (14). In summary, the reduced intensities of a specific (*hkl*) reflection measured in LD, TD, and ND of the plate are proportional to the number of unit cells in the scattering volume with their (*hkl*)-plane normal and the scattering vector parallel to these three directions. Therefore, the concept of reduced intensity can be used to analyze the preferred orientation. Note that if the texture is random, the reduced intensities are the same for all reflections.

6.2.2. Peak intensity variation

Figure 6.7 shows the diffraction patterns (cross symbols) measured with the scattering vector parallel to the ND (z-direction) in the BM, HAZ, TMAZ and DXZ in *Case 1*. The lines shown with the data represent the calculated results using Rietveld refinement without considering the texture. Thus, the discrepancy between the measured (crosses) and calculated (lines) data qualitatively illustrates the presence of texture in the specimen. In the BM, the measured (200) peak is much stronger than the calculated intensity assuming a random texture, which reveals the initial recrystallized rolling texture in the as-received Al plate. Accordingly, the measured intensity of the (111) reflection is slightly weaker than the random texture case. The intensities in the HAZ are similar to those observed in the BM. Note that the TMAZ shows a noticeable increase of the measured (111) reflection. Finally, in the DXZ, the measured peak intensity of (111) reflection is higher than the calculated intensity. Such considerable change indicates the texture variation in the DXZ.

Figure 6.8 shows the diffraction patterns measured at the BM, HAZ, HAZ at *root*, and TMAZ at *face* in *Case 2*. First, the diffraction patterns of the BM and HAZ do not

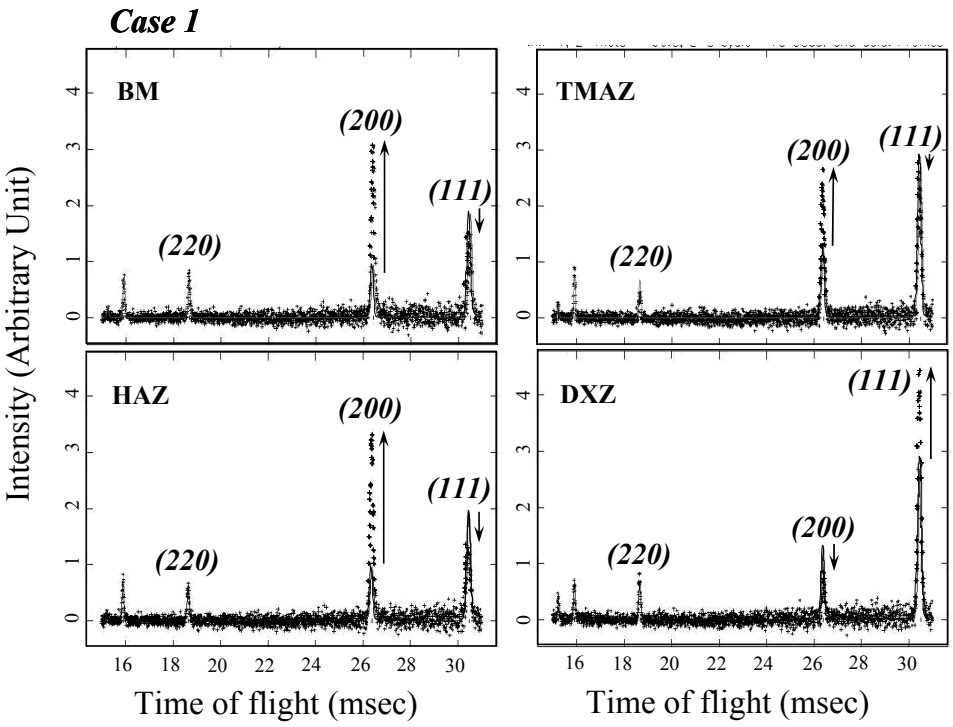

Fig. 6.7. The diffraction patterns of *Case 1* measured with the scattering vector parallel to ND at various positions along TD: base material (BM), heat-affected zone (HAZ), thermo-mechanically affected zone (TMAZ), and dynamic recrystallized zone (DXZ). The symbols (crosses) are the measured data and the lines overlapping the crosses are the calculated data using Rietveld refinement without considering the texture. Thus, the discrepancy between the measured and calculated data (shown with the arrows for the (111) and (200) reflections) indicates the texture in the specimen.

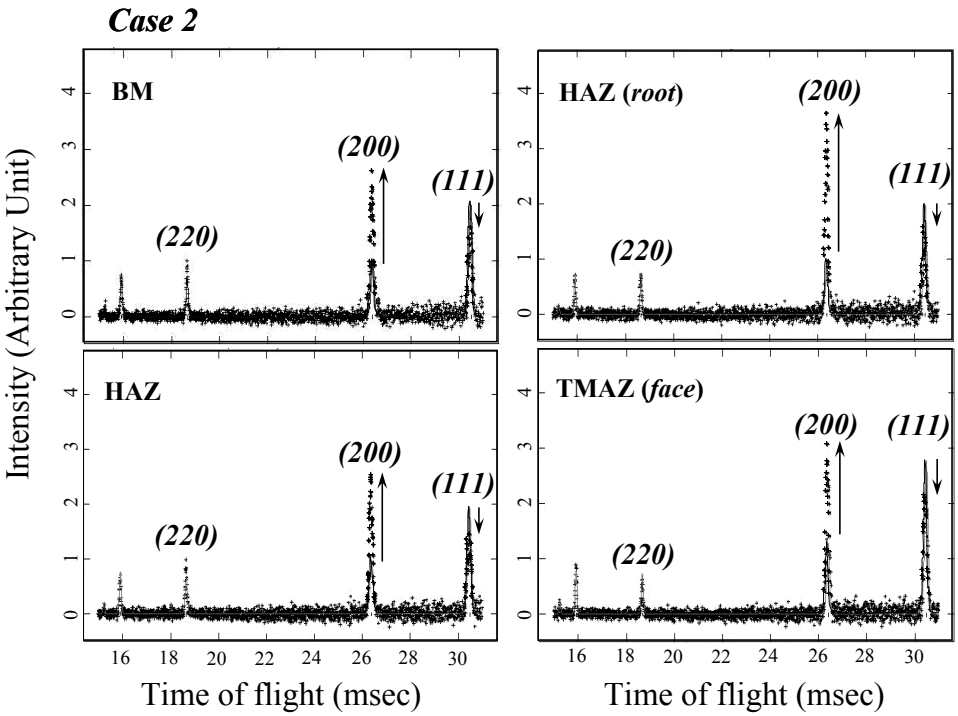

Fig. 6.8. The diffraction patterns of *Case 2* at BM, HAZ, HAZ at the *root*, and TMAZ at the *face*.

show significant differences in the peak intensities. In both regions the intensity of the (200) peak is higher than that predicted by the Rietveld refinement without texture consideration, showing the preservation of the initial recrystallized rolling texture. For the diffraction pattern of HAZ measured at *root*, it shows an increase in (200) peak intensity, which may be attributed to the variation in the recrystallized rolling texture through the thickness of the as-received plate. Finally, the (200) and (111) peak intensities measured in the TMAZ (*face*) of *Case 2* are similar to those of the TMAZ in *Case 1*.

6.2.3. Texture analysis using the reduced intensity

Figures 6.9 and 6.10 show the variations of the reduced intensities across the centerline in *Cases 1* and *2* along the middle of the thickness of the plates (*center*). The reduced intensity of a particular (*hkl*) reflection is proportional to the number of unit cells in the scattering volume with its [*hkl*] parallel to the scattering vector. Therefore, the reduced intensities provides quantitative insights to the texture variation obtained by observing the intensity ratio among various (*hkl*) reflections.

Figure 6.9(a)-(c) show the LD, TD, and ND components of the (200), (220), and (111) reduced intensities in *Case 1*, respectively. Firstly, the reduced intensities exhibit 2.3 for (200) and 0.9 for (220) at the -30 mm position in Fig. 6.9(a). It indicates that there are approximately 2.6 times more unit cells oriented with (200) normal to LD than (220) oriented normal to LD. The relative ratio among the three reflections in a given measurement direction is comparable to the volume-averaged pole density in the pole

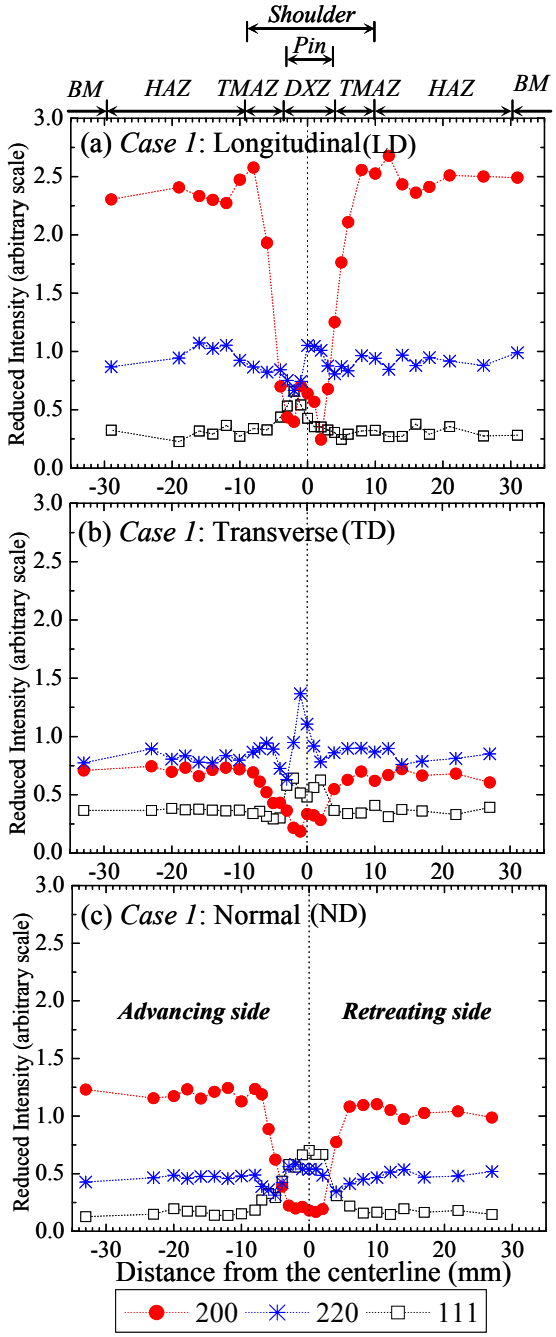

Fig. 6.9. The reduced intensities of the (200), (220), and (111) reflections measured along the middle of the plate thickness (*center*) with their scattering vectors parallel to the longitudinal, transverse, and normal directions as a function of the distance from the centerline. (a) LD, (b) TD, and (c) ND of *Case 1*.

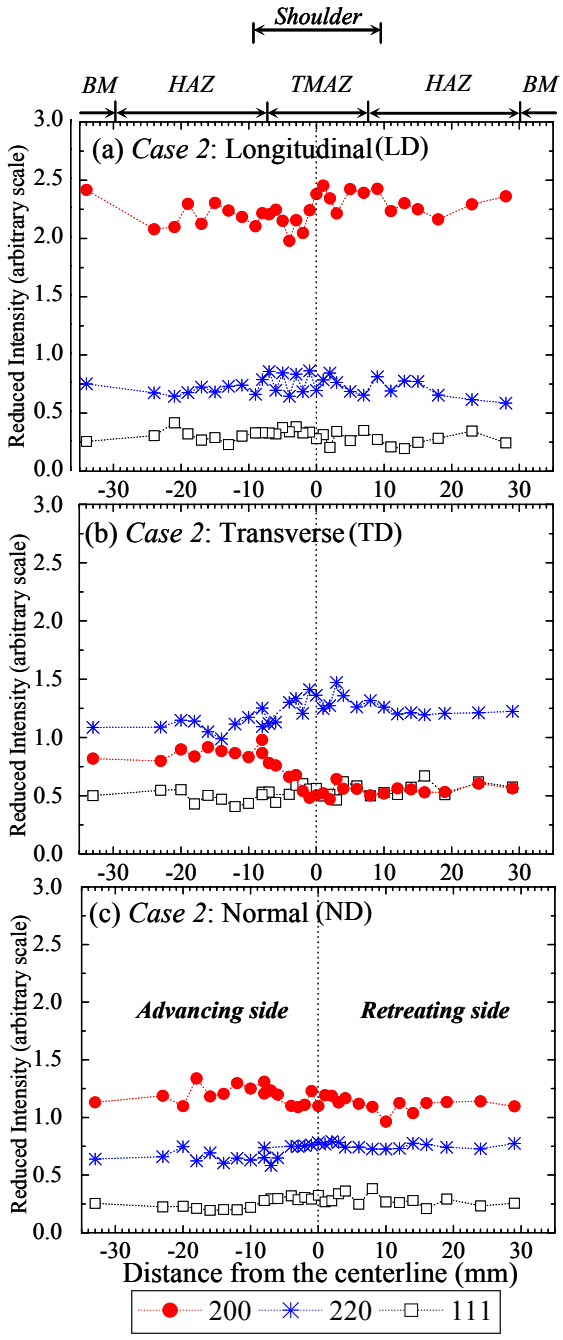

Fig. 6.10. The reduced intensities of the (200), (220), and (111) reflections measured along the middle of the plate thickness (*center*) with their scattering vectors parallel to the longitudinal, transverse, and normal directions as a function of the distance from the centerline. (a) LD, (b) TD, and (c) ND of *Case 2*.

figure results measured by the HIPPO instrument. For example, in the BM (***A*** coupon), the m.r.d. parallel to the LD in the (200) pole figure is 2.9 and the m.r.d. parallel to the (220) pole figure is 1.3 resulting in the m.r.d. ratio of 2.2, Fig. 6.9(a). Hirsch *et al*. reported that the texture of recrystallized pure (99.99%) aluminum plate, which was subjected to a cold rolling with the 95% thickness reduction followed by heating for 10 seconds at 500 ºC, was composed of 56% of cube (200) grains and 17% of Goss (220) grains (approximately a ratio of 3) along the LD [50]. Secondly, in the HAZ the reduced intensities are similar to the BM. Finally, in the DXZ/TMAZ the reduced intensities show considerable variations in all three directions in *Case 1*. For example, the reduced intensities of (200) significantly decreased, while the (111) intensities increases near the DXZ, which experienced the severe plastic deformation during FSP.

Figure 6.10 shows the reduced intensities in *Case 2*. The reduced intensity profiles of *Case 2* do not show significant variations near the centerline, which is consistent with the pole figure results near the centerline. The reduced intensity results for both *Cases 1* and *2* in all orientations show consistent results in the BM region indicating a good reproducibility in measurements and data analyses. For example, the reduced intensities of the (200) reflections vary in the range of about 2.0 ~ 2.5 in the LD measurements in the BM in both cases, Figs. 6.9(a) and 6.10(a).

6.2.4. Reduced intensity variations through the thickness of the plate

Figures 6.11 and 6.12 show the reduced intensity variations through the thickness of the plates, which were measured along the *face, center*, and *root* on the retreating side of *Cases 1* and *2*. The reduced intensities through the thickness are shown here with the

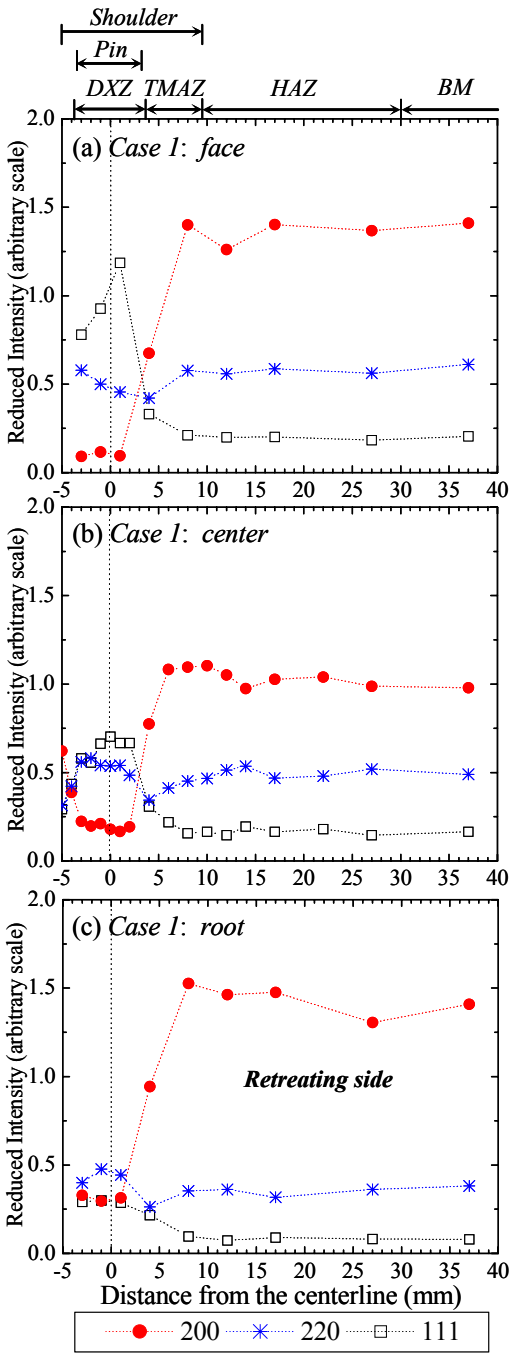

Fig. 6.11. The reduced intensities of the (200), (220), and (111) reflections measured through the thickness of the plates (*face*, *center,* and *root*) on the retreating side with their scattering vector parallel to ND as a function of the distance from the centerline. (a) *face*, (b) *center*, and (c) *root* of *Case 1*.

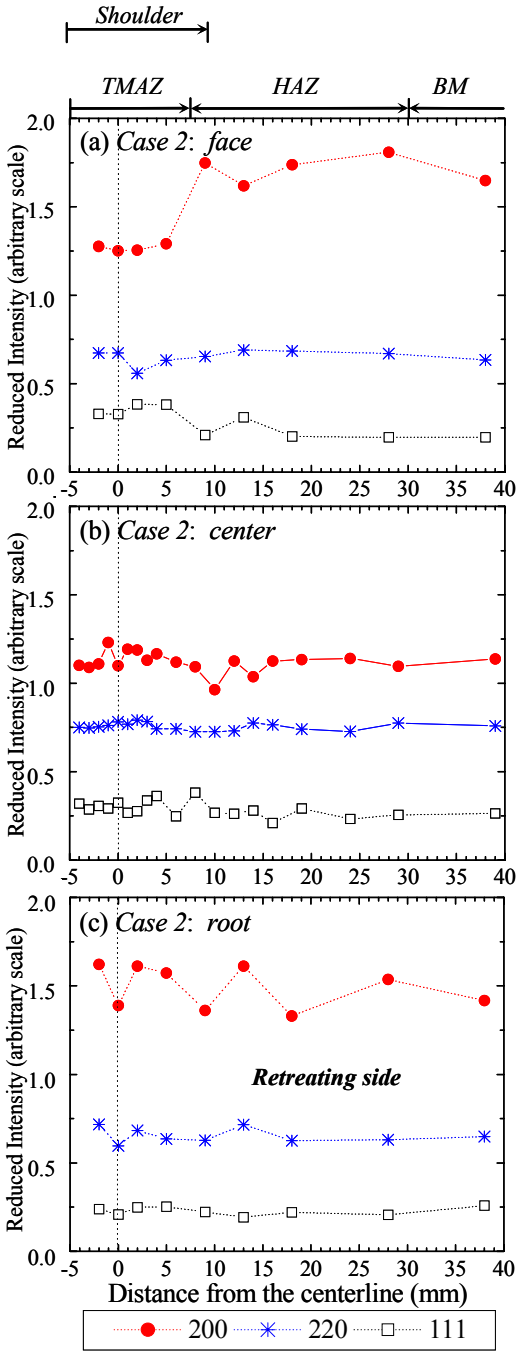

Fig. 6.12. The reduced intensities of the (200), (220), and (111) reflections measured through the thickness of the plates (*face*, *center,* and *root*) on the retreating side with their scattering vector parallel to ND as a function of the distance from the centerline. (a) *face*, (b) *center*, and (c) *root* of *Case 2*.

scattering vector parallel to the ND only. Note that measurements were performed along all three directions and show similar results. In the BM and HAZ of both *Cases 1* and *2*, the reduced intensity of all reflections spread wider at the *face* and *root* compared to the *center* scan. This trend indicates that the top and bottom surfaces of the plate have stronger initial recrystallized rolling texture.

In *Case 1*, approaching near the centerline towards TMAZ and DXZ, the (200) reduced intensities decreased sharply, while the (111) reduced intensities increased. The changes are more significant at the *face* as shown in Fig. 6.11(a) compared to the *center* and *root* in Figs. 6.11(b) and (c). Comparing the (111) reduced intensities between the *face* and *root,* Figs. 6.11(a) and (c), the *face* has up to about 5 times more (111) unit cells than the *root* in the DXZ region. On the other hand, the *Case 2*, Figs. 6.12(a)-(c), shows little differences among the *face, center*, and *root* except a small decrease of the (200) reduced intensities near the centerline at the *face* in Fig. 6.12(a). This observation indeed suggests that the dark upper region in *Case 2* shown in Fig. 4.2 is the TMAZ where the compressing tool shoulder caused the partial plastic deformation. Also note that the width of the variation in the profile is similar to the width of the TMAZ caused by the pressing tool shoulder.

6.2.5. Pole figure and reduced intensity

The reduced intensity results are consistent with the pole figure results. For example, in the BM, Figs. 6.9(a) and (c) show the significantly decreased (200) reduced intensities in *Case 1* along LD and ND, which is consistent with the strong initial recrystallized rolling texture observed in the (200) pole figure of the ***A*** coupon (BM) as

shown in Fig. 6.5. Similarly, in the HAZ, the strong texture could be found in both the (200) reduced intensity and pole figure results. For the DXZ/TMAZ, the significant decrease in (200) reduced intensities accompanied by the increase in (111) reduced intensity shown in Figs. 6.9(a)-(c) is similar to the results of the weak (200) pole figure and the relatively strong (111) pole figure as shown in Fig. 6.5. Both the pole figure and reduced intensity results for *Case 2* clearly show the absence of the significant texture variation. One discrepancy could be found in the pole figure of the ***C*** coupon, Fig. 6.5, where the (200) texture in the pole figure is remaining at 40° from the ND. It could be due to the volume-averaged measurements performed on the relatively large coupon used in the current study ($10 \times 10 \times 6.5$ mm^3).

6.3. Dynamic recrystallization

Previous texture studies suggested that the DXZ could be caused by the dynamic recrystallization that forms the new strain-free recrystallized fine grains in the severely deformed zone during and after the FSW [92]. In the present study the presence of the DXZ in *Case 1* and the absence of the DXZ in *Case 2* clearly show that the dynamic recrystallization is due to the severe plastic deformation caused by the rotating tool pin. Furthermore, the current neutron-diffraction observation is consistent with the literature in that there is a dramatic texture variation in the DXZ in *Case 1* [46-50]. Thus, the comparison of ODFs, pole figures, and reduced intensities between *Cases 1* and *2* reveals that the cause of the texture variation can be related to the dynamic recrysyallization associated with the severe plastic deformation due to the stirring tool pin, which is

evident from the significant increase in the {111} shear texture from the initial cube and mixed cube/Goss texture in *Case 1* [46,48]. Furthermore, the absence of the texture variation in *Case 2*, which was subjected to little plastic deformation, shows that the frictional heating alone does not cause a texture variation.

It was previously reported that the dominant source of the residual stress in FSP aluminum alloys is the frictional heating rather than the plastic deformation from the tool pin [62,63]. Thus, the microstructure and mechanical properties of the FSP Al, in general, could be affected by both the pin and tool shoulder. More specifically, the severe plastic deformation and the frictional heating affect the mechanical properties of the FSP Al through the variation of the texture and through the increase in the residual stress, respectively. In addition, the combination of the plastic deformation and heat also modifies other microstructural features such as precipitates (aging), grain sizes, etc, which also affect the mechanical behavior of the FSP Al alloy.

6.4. Material flow and the shear texture

The texture variation within about the 19 mm around the centerline in *Case 1* is similar to the size of the DXZ/TMAZ, Fig. 6.9(a). The 7-mm-wide DXZ is similar to the 6.35-mm pin diameter; while the 19-mm-wide DXZ/TMAZ is close to the 19.05-mm shoulder diameter. Such similarity between the tool geometry and the extent of texture variation is, in turn, related to the material flow pattern during the FSP. Seidel and Reynolds revealed using a marker insert technique that material transportation during the FSP follows the streamlines surrounding the rotating pin [100].

Figure 6.13(a) illustrates the material flow associated with the rotation and travel of the tool during the FSP. Note that the flow is a solid-state material transportation within the region contacting the rotating tool with the other stationary body (i.e., cold base material) known as a quasi-hydrodynamic bearing zone. In the contacting region that may roughly surround the tool pin surface the frictional force could cause the shear stress to generate the severe shear slip during the FSP. Sato *et al*. suggested that the {111} slip planes sliding along the <110> directions can alter the texture during the FSP [48]. The shear stress can cause easy gliding on {111} slip planes along the <110> slip directions, which is parallel to the rotating pin's surface. It constructs a trace of {111} planes around the rotating pin. The texture (reduced intensities) variations observed in this study are in good agreement with the relationship between the material flow during the FSP and the slip system of aluminum alloys, in that the intensity of (200) along the LD and ND significantly decreases, while the (111) intensity increases along the LD and ND in the DXZ/TMAZ, Figs. 6.9(a) and (c).

The through-thickness texture variation also could be related to the characteristic material flow associated with the geometry of the tool. The reason for the through-thickness variations in the texture can be the strong frictional force (shear stress) on the surface of the plate by the direct contact of the tool shoulder, resulting in the relatively stronger (111) intensity along ND at *face* as shown in Fig. 6.11(a). Field *et al*. showed the existence of strong shearing planes beneath the tool shoulder along the ND, which suggested severe texture gradient through the thickness of FSW plate [49]. Seidel and Reynolds also suggested vertical circular flow of material behind the traveling tool pin [100]. It was shown that the circular flow of the material is downwards on the advancing

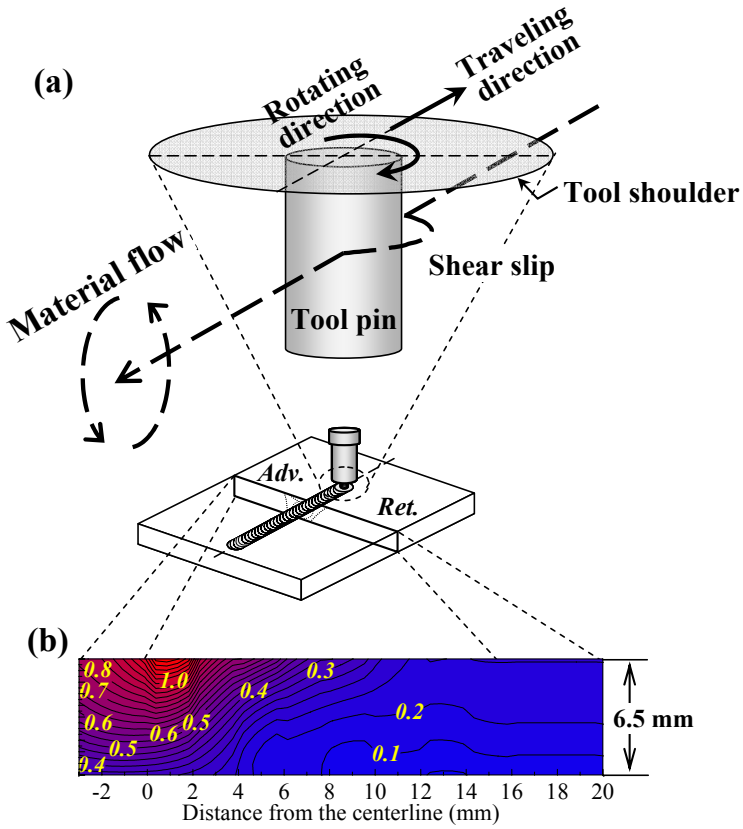

Fig. 6.13. The relationship between the material flow during FSP and the texture variation. (a) Material flow (dashed line) during the FSP and (b) through-thickness contour plot of the reduced intensities of (111) along the ND in *Case 1*

side and upwards on the retreating side followed by the material transportation from the retreating side to the advancing side to occupy the empty space on the advancing side as illustrated in Fig. 6.13(a). Such material flow may cause the observed texture gradient through the thickness. The precise material flow should be dependent on the exact tool geometry and the processing parameters used. However, the screw type and weld pitch used in their study are similar to the current experimental condition. Finally, Fig. 6.13(b) shows the through-thickness contour plot of the reduced intensities of (111) along the ND in *Case 1*. Note that the plot was constructed using the through-thickness data using the bilinear interpolation method. The contour plot shows that (111) texture is stronger near the tool pin and under the tool shoulder. The investigation of the overall texture variations as a function of distance from the centerline clearly shows that the shear texture is mainly caused by the severe shear deformation from the stirring tool pin during FSP.

Chapter VII On-going/future work: FSP of magnesium alloys

7.1. Microstructure and tensile properties

7.1.1. Objectives

Recently, various studies have been reported on the FSW/FSP of magnesium alloys [101-105] that includes microstructural evolutions of wrought Mg alloy AZ31B [101], heat-resistant Mg-Al-Ca alloy [102], and fabrication of highly formable AZ91D magnesium plates via the grain refinement and homogenization after the multi-pass FSP [103]. Tailoring of microstructure could facilitate localized superplasticity at specific locations that are subjected to severe plastic deformation during the FSP.

Magnesium alloy is one of the lightest metals in use for structural applications [106]. However, poor workability, due to the limited number of available slip systems in the hexagonal close packed (hcp) structure, imposes manufacturing limitations [107]. To enhance and control mechanical properties (e.g., tensile strength and elongation) of magnesium alloys, extensive research efforts have been focusing on microstructural modifications including equal channel angular processing (ECAP) [108-111]. It has been reported that texture of the Mg alloy significantly influences mechanical properties, such as tensile elongation at room temperature, after ECAP [108,109].

Likewise, the integrity and performance of magnesium alloys can be significantly influenced due to the changes in the texture during the FSP [112]. Recently, Park *et al.* observed the fractured surface of a FSW AZ61 Mg alloy tensile specimen and found a strong texture (i.e., basal plane was tilted 45º from the fracture surface normal) [52].

Other examples include: micro-texture evolutions in AZ61 [51], tensile properties of AZ31B-H24 [104], and grain size/orientation of AZ31 [105] after the FSW/FSP. However, direct correlation of the spatially-resolved texture variation to tensile strength/elongations and to the resulting fracture locations of FSP magnesium alloys is not available in the literature to date.

In this chapter, tensile properties were investigated using specimens prepared from various locations in the FSP AZ-31B plate with the gage length cut parallel and perpendicular to the processing direction. Furthermore, the diffraction peak-intensity changes were measured using the neutron diffraction technique and analyzed to present texture variations as a function of distance from the centerline after the processing. The results provide the relationship between texture distributions and tensile properties that include enhanced elongation, decreased tensile strength, and the location of the fracture.

7.1.2. Sample preparation and tensile test

Commercial AZ31B magnesium-alloy rolled plates were used in the annealed condition (O tempering). The nominal chemical composition in weight percent is 3.0 Al, 1.0 Zn, 0.2 Mn, and balance Mg. The dimension of the FSP specimen was 306 x 306 x 6.5 mm, Fig. 7.1. The plate was processed using the following parameters: 0.97 mm/sec traveling speed, 600 rpm clockwise rotating speed, and 12.4 MPa compressive pressure using a tool with a 19.05-mm shoulder diameter and a 6.35-mm pin diameter with a 5.72-mm pin height. The tool was tilted 3 degrees opposite to the processing direction, which coincides with the rolling direction of the plate. Note that LD, TD, and ND denote longitudinal, transverse, and normal directions of the plate, Fig. 7.1.

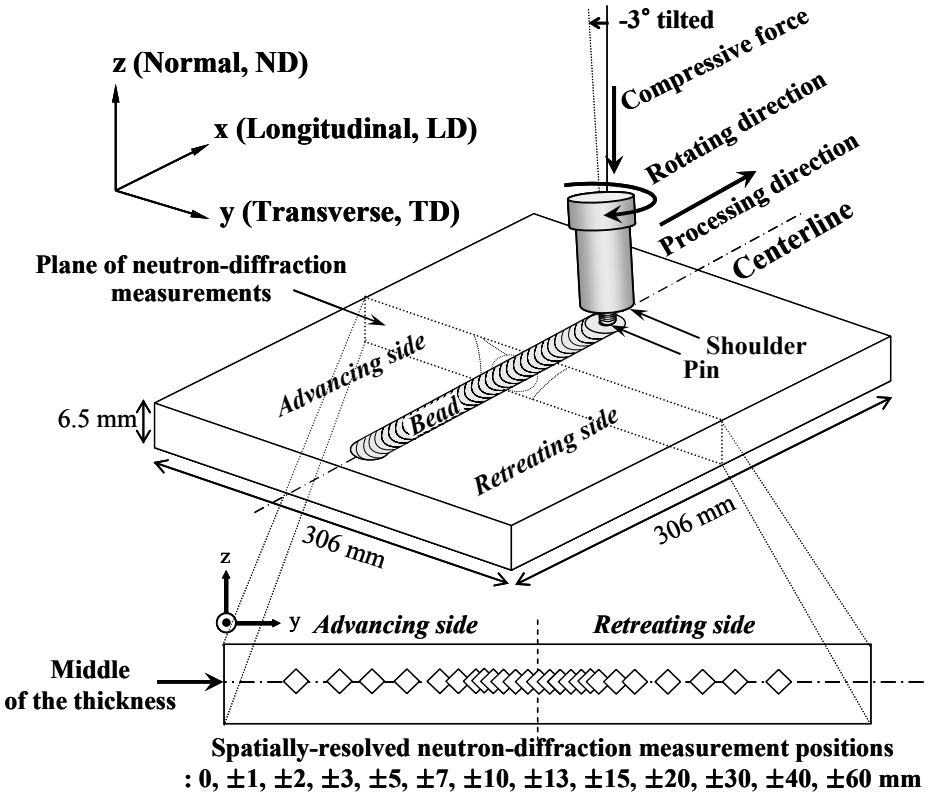

Fig. 7.1. Schematic of the friction-stir processing and spatially-resolved neutron-diffraction measurement positions across the centerline of the AZ-31B magnesium alloy plate.

A number of tensile specimens were prepared from the FSP plates. First, TD tensile specimens (gage length normal to the processing direction) were cut from the base material and FSP plates at the middle of the plate length, Fig. 7.2(a). In addition, a total of six (one from base material and five from the FSP plate) LD tensile specimens (gage length parallel to the processing direction) were prepared, Fig. 7.2(b). Note that LD specimens were cut parallel to the processing and rolling direction to present the various zones in the FSP plate. In particular, the LD tensile specimen prepared from "0" mm will illustrate the tensile behavior of the "stir zone". All tensile specimens were prepared using electrical-discharge machining with the subsize dimension (i.e., 25-mm gage length and the 6-mm width) following ASTM E 8M-04, Fig. 7.2(b). Tensile tests were performed using the Material Test System using hydraulic wedge-grips at a constant crosshead velocity providing an initial strain rate of about 6.68×10^{-4} s^{-1} at room temperature. Microstructural characterization was performed at the yz-plane cross-sections, of the base material and FSP plates. The samples were cold-mounted, ground, polished, and etched by a mixture of 4.2 g picric acid, 10 ml acetic acid, 70 ml ethanol, and 10 ml diluted water solution for about 10 s.

7.1.3. Tensile properties and microstructure

Figure 7.3 shows the results of TD tensile tests of a sample taken from the base material and one across FSP region. The base material shows a 230 MPa tensile strength and 28% total elongation, which is consistent with the literature [52]. Compared to the base material, the FSP plate has decreased tensile strength of about 180 MPa and elongation of about 12 %.

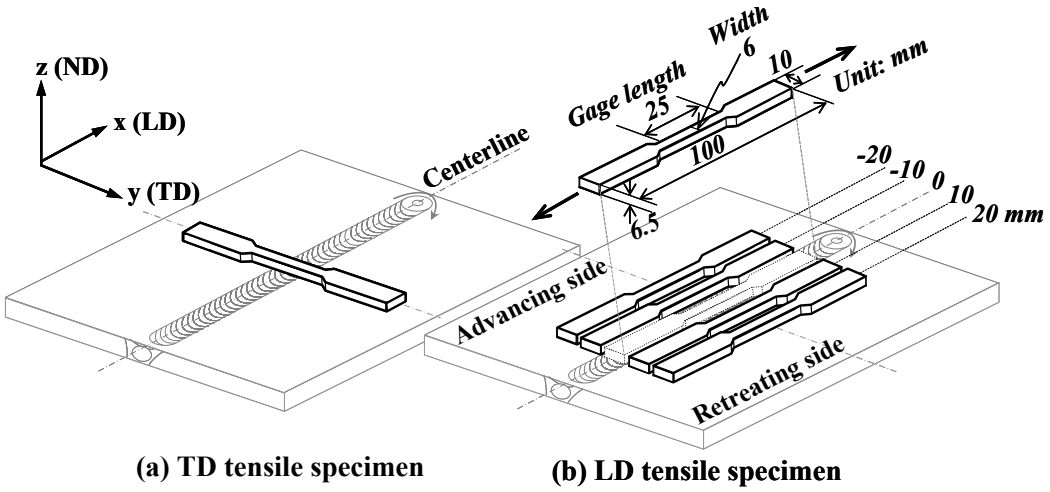

Fig. 7.2. Tensile test specimens were cut along (a) the transverse and (b) longitudinal directions. Specimens were prepared from both base material and various locations in the friction-stir processed plates based on ASTM E 8M-04.

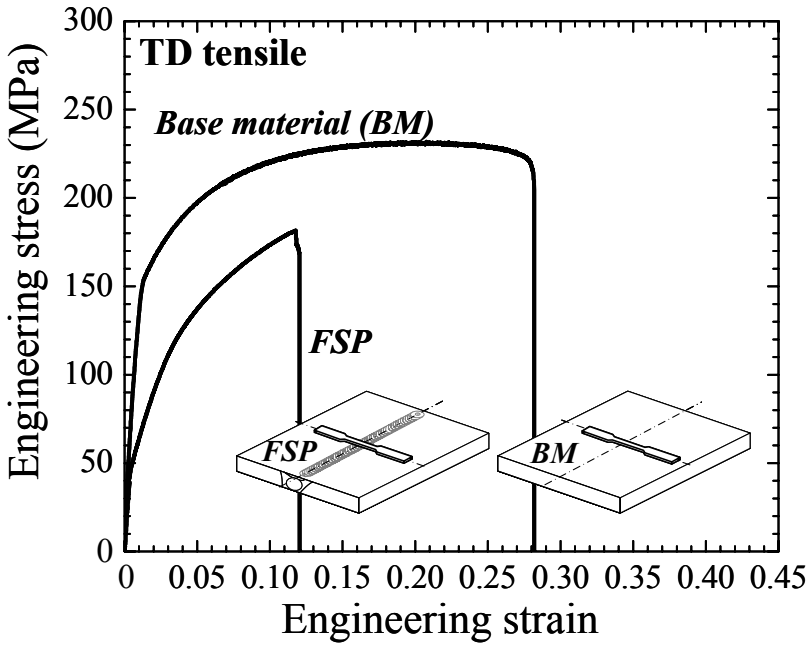

Fig. 7.3. Tensile test results of AZ-31B magnesium alloy. Transverse tensile properties of base material and friction-stir processed (FSP) specimens

Figure 7.4 shows the results of LD tensile tests on samples taken from the base material and at several positions in the FSP plates. Specifically samples were cut at ±20 mm, ±10 mm, and 0 mm from the processing centerline. Approximately, 250 MPa tensile strength and 32 % elongation were measured for the base material along the LD, which is similar to the TD results. However, the results of LD FSP tensile specimens show quite different behavior depending on the location from which the tensile specimen was machined. First, the tensile behavior of the FSP specimen, which was cut out from the centerline (i.e., at 0 mm), shows 41 % elongation and about 200 MPa tensile strength. Note that the width of the LD specimen covers -3 ~ 3 mm from the centerline due to the 6 mm width of the specimen, Fig. 7.4, which is corresponding to the severe plastic deformed region (also known as the dynamically recrystallized zone) during the FSP [51,101]. On the other hand, the LD tensile results of the other specimens show slightly decreased elongation and tensile strength compared to the base material. The mechanical properties between the advancing side and retreating side seem to be different, which may be due to the asymmetric flow of plasticized materials during the FSP [100]. For example, the elongation of specimens in the advancing side is relatively lower than that of the retreating side.

Figure 7.5 shows microstructure and texture of the base material (AZ31B-O rolled plate). The pole figure, Fig. 7.5(a), presents a strong texture (the maximum pole density of 10.3 multiples of random) where the (0002) basal plane normal is parallel to the ND, which is the well-known hot-rolling texture of Mg alloys [51]. Figure 7.5(b) shows the optical microscopy investigated about 50 μm of the average grain size (based on the linear intercept method) for the as-received condition. Figure 7.6 shows the

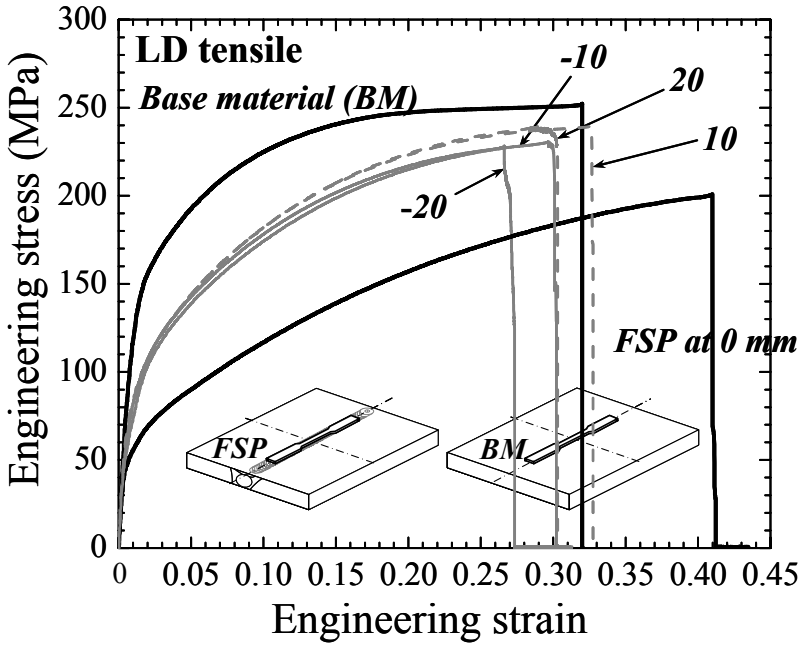

Fig. 7.4. Tensile test results of AZ-31B magnesium alloy. Longitudinal tensile properties of the base material (BM) and five specimens prepared from various positions in FSP plate as shown in Fig. 7.2(b).

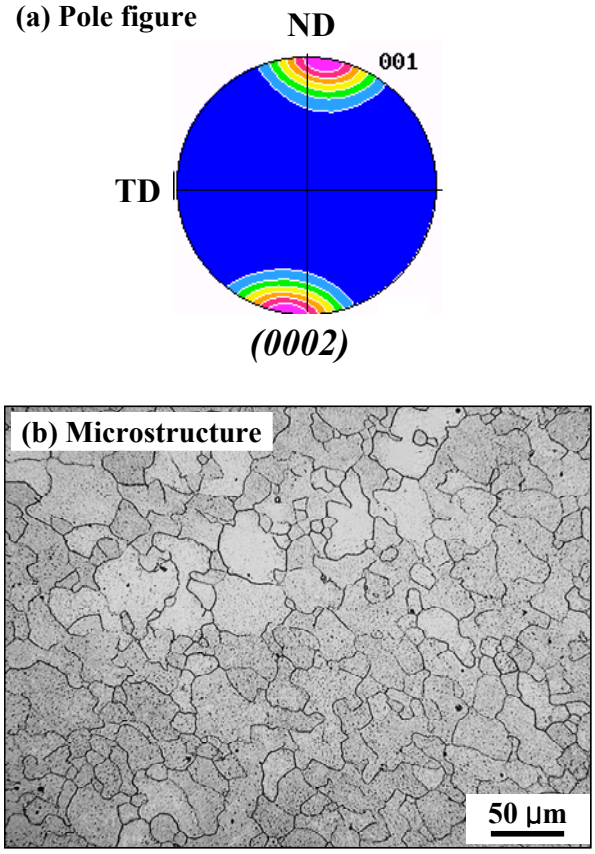

Fig. 7.5. Texture and microstructure of base material. Note that the strong initial texture of the base material shows the (0002) basal plane normal parallel to the plate thickness direction (ND).

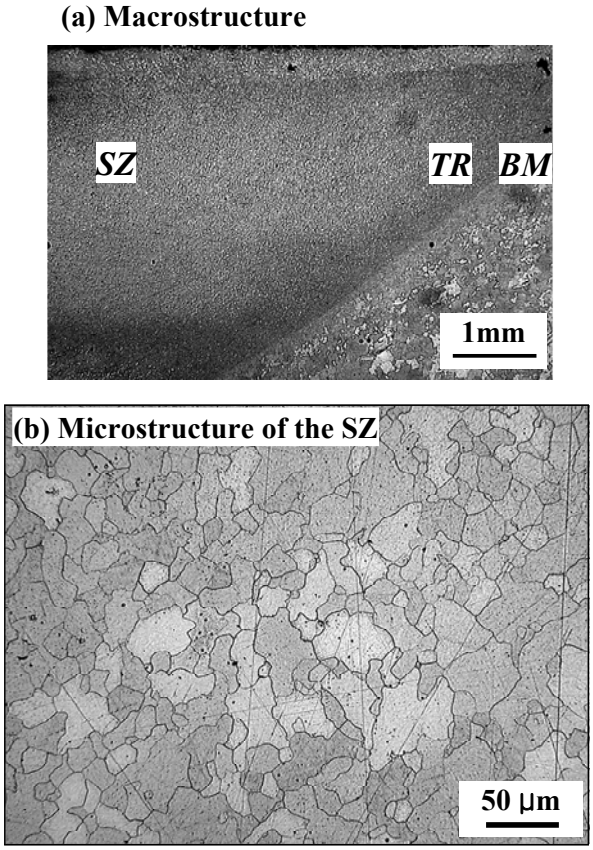

Fig. 7.6. Macrostructure and microstructure of the FSP Mg; (a) the base material (BM), transition region (TR), and stir zone (SZ) are marked, (b) microstructure of the SZ.

macrostructure and microstructure of the stir zone in the FSP. The macrostructure designated as the base material (BM), transition region (TR), and stir zone (SZ), Fig. 7.6(a). Note that no significant difference in the average grain size could be found in the stir zone compared to the base material under the current processing conditions.

7.2. Texture measurements

Spatially-resolved neutron-diffraction measurements were performed to obtain texture variations [15]. The SMARTS instrument [17] was used to measure the diffraction from grains with their reflecting *hkl* lattice plane normal oriented parallel to LD, TD, and ND [24]. Note that the peak intensities from each plane were obtained using the single peak fitting method in the GSAS [85]. Only results of (0002) basal plane are presented here because it is the primary slip plane of Mg at the relatively high strain rates and high temperatures (e.g., about 400ºC) associated with the FSP [51,105]. The peak intensities were measured at various locations (a total of 25 positions) along the middle of the plate thickness, Fig. 7.1. A complete orientation distribution function of the base material was determined on the HIPPO diffractometer.

The integrated intensity (I_τ) measured using neutron diffraction is proportionally related to the number of the scattering unit cells (N_s) [15]. The integrated intensity can be converted to the reduced intensity, presented on a common scale, can provide the quantitative comparison among the various orientations. Figure 7.7 shows reduced intensity variations of the (0002) basal plane as a function of distance from the centerline. In the base material (at - 60 mm), the basal plane intensity along the ND is about 6 times

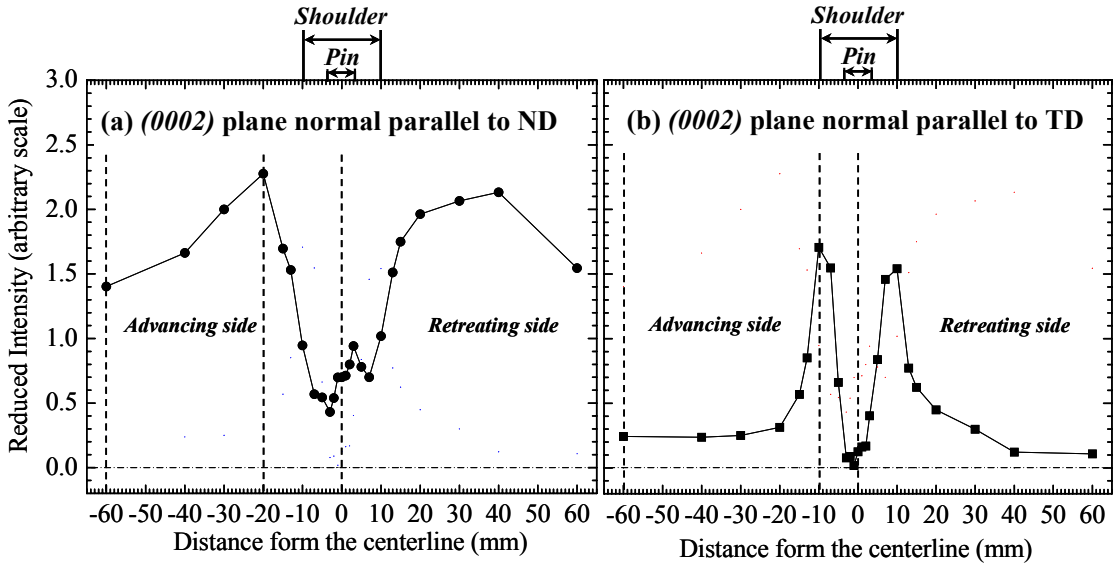

Fig. 7.7. Reduced intensities of (0002) reflection measured along the middle of the plate thickness with their scattering vectors parallel to (a) the normal direction (ND) and (b) the transverse directions (TD) as a function of distance from the centerline of the FSP plate. No intensity data is available along the longitudinal direction due to the very weak intensity of the basal plane.

stronger than that along the TD, which reflects a strong rolling texture of the as-received Mg plate. The result is consistent with the pole figure shown in Fig. 7.5(a). Moreover, Fig. 7.7(a) shows that 1.4 scale of the basal plane normal was parallel to the ND at -60 mm on the advancing side. It increased to 2.3 at -20 mm and significantly decreased to 0.7 near 0 mm (the stir zone). On the other hand, the TD intensity, Fig. 7.7(b), was only about 0.2 at -60 mm, maximized at -10 mm, and decreased near the centerline. The reduced intensity results suggest that the basal plane normal is parallel to the ND at base material, but is parallel to the TD near the transition region. Finally, the strong texture of the (0002) basal plane can be significantly weakened in the stir zone due to severe plastic deformation.

7.3. Tensile properties

The texture variations suggest that shear plastic flow during the FSP causes about 90 º rotation of the basal plane near the processing zone so that its normal is parallel to the TD in the transition region. In addition, the severe plastic deformation destroys the texture in the stir zone via dynamic recrystallization and results in a texture in which the basal plane normal is roughly surrounding the rotating pin surface [51]. Figure 7.8 shows a schematic illustration for dominant textures in the base material, transition region, and stir zone. Due to the shear deformation of the hcp magnesium alloy during the FSP, the basal plane rotated and rearranged to crystallographically characteristic directions in each region.

Based on the texture characterization, the nature of the tensile behavior could be related to the slip system and associated Schmid factor. Table 7.1 summarizes the Schmid

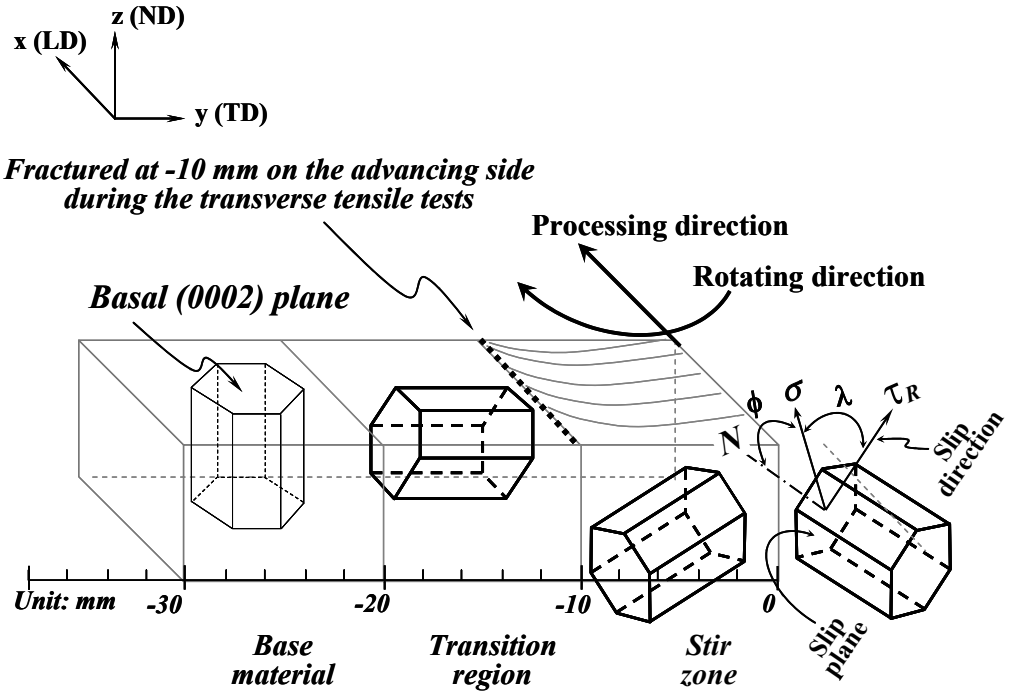

Fig. 7.8. Schematic of basal plane tracing from the base material, transition region, to stir zone on the advancing side of the FSP Mg plate. Note that fracture occurred at -10 mm on the advancing side during the transverse tensile tests, Fig. 7.2. Note that λ is the angle between the slip direction and the tensile axis, Φ is the angle between the normal to the slip plane and the tensile axis, σ is the applied tensile stress, N is the direction normal to the slip plane, and τ_R is the critical resolved shear stress.

Table. 7.1. Schmid factors ($m = cos\ \Phi\ cos\ \lambda$) for the longitudinal tensile test in characteristic regions of the FSP with the dominant texture, slip system, and simplified angles. Note that λ is the angle between the slip direction and the tensile axis and Φ is the angle between the normal to the slip plane and the tensile axis.

	Dominant texture	**Slip system**	λ	Φ	**Schmid factor (m) (= $cos\ \Phi\ cos\ \lambda$)**
Base material	**<0001> // ND**	**{0002} <11-20>**	**0º**	**90º**	**0**
Transition region	**<0001> // TD**		**0º**	**90º**	**0**
Stir zone	**<0001> ⊁ ND, TD**		**45º**	**45º**	**0.5**

factor using the dominant texture and slip system of the three regions. The calculated results show that the preferred orientation of the basal planes in the stir zone of FSP results in a maximum (~ 0.5) Schmid factor due to about 45 º angle between the applied stress and slip directions. The texture variation and the resulting high Schmid factor value for the basal slip are consistent with the enhanced elongation and lower tensile strength observed in the LD tensile specimen cut from the stir zone as shown in Fig. 7.4.

An interesting observation is the fracture location in the TD tensile test of the FSP. The fracture occurred at about -10 mm on the advancing side of the plate, Fig. 7.8. The amount of grains that have their basal plane normal parallel to TD are maximum near the ±10 mm of the plate resulting in significant texture variation and minimized Schmid factor, Fig. 7.7(b). Furthermore, considering lower elongations of tensile specimens at -20 mm and -10 mm on advancing side compared to those at 10 mm and 20 mm on the retreating side, Fig. 7.4, the fracture location on the advancing side is reasonable. The specific fracture location is close to the boundary between the transition region and stir zone on advancing side. The incompatibility between the plasticity in the stir zone and transition region may have caused the fracture near the -10 mm location.

Chapter VIII Summary and Conclusions

1. Neutron diffraction was used to investigate the residual stress changes in the friction-stir processed (FSPed) 6061-T6 aluminum alloy plates. Two FSP specimens were prepared with a purpose of separating the effects of frictional heating and severe plastic deformation on the changes of the as-received rolled and recrystallized 6061-T6 aluminum-alloy plates: (*Case 1*) a plate processed with both stirring pin and tool shoulder, i.e., a regular friction-stir processing plate subjected to both plastic deformation and frictional heating, and (*Case 2*) a plate processed only with the tool shoulder, i.e., subjected mainly to the frictional heating.

The comparison between a regular FSP specimen (subjected to both heating and deformation) and a plate processed only with the tool shoulder (subjected mainly to the heating effect) clearly showed that the heat input from the tool shoulder is a major source of the internal strains.

This portion of the study also focused on the residual stresses distributions through the thickness of the FSP plates and its effect on the angular distortion. Residual strain profiles were measured through the thickness of the FSP 6061-T6 aluminum-alloy plates using neutron diffraction. A regular FSP (*Case 1*) and the "shoulder-only" (*Case 2*) studies show that the tool pin acting as a heat-transfer medium in *Case 1* and the tool shoulder as a non-uniform heat distributor in *Case 2*. The results of the through-thickness residual stress variations in the "shoulder-only" case show that non-uniform (asymmetric) residual stress distributions can be related to the angular distortion. The current study suggests that an optimal combination of the effects from the stirring pin and the tool

shoulder could minimize the through-thickness variations of residual stress and angular distortions in the FSP.

2. Furthermore, the reduction of the longitudinal residual strain profiles within the bead area measured by the neutron diffraction was correlated to the microstructural softening and the reduction of the hardness. The presence of the dynamic recrystallized zone (DXZ) in *Case 1* and the absence of the DXZ in *Case 2* is a direct evidence that the DXZ is a result of the severe plastic deformation caused by the stirring tool pin during the FSP. Microstructure and hardness profiles of *Cases 1* and *2* show that the microstructural softening was mainly caused by the frictional heating from the tool shoulder during the FSP. In *Case 1*, the softening in the DXZ and thermo-mechanically affected zone (TMAZ) is related to the dissolution of fine needle-shape precipitates (β'') due to the frictional heating, which reduced the microhardness (H_v) from the initial 110 H_v to 70 H_v. On the other hand, in the heat-affected zone (HAZ), the softening is related to the dissolution of β'' and growth of the coarse precipitate phase, which reduced the initial hardness to 60 H_v. In *Case 2*, the TMAZ (near the top surface) and the HAZ show similar softening behavior as in *Case 1*.

3. Natural aging behavior was investigated by observing the changes in the microhardness values as a function of time (t=hour) over a period of 8 months after the FSP. In *Case 1*, the natural aging kinetics of the FSP-affected regions was quantified as follows: $H_v = 63 + 4.3 \log (t)$ for the DXZ and $H_v = 64 + 3.0 \log (t)$ for the TMAZ of *Case 1* under the current processing conditions. On the other hand, little or no natural

aging was observed in the HAZ in both *Cases 1* and *2*. In Case 2, natural aging was observed in the TMAZ (*face*); where $H_v = 61 + 5.4 \log (t)$. The results suggest that the frictional heating from the tool shoulder facilitates the natural aging only near the top surface, while the presence of the tool pin results in a more homogeneous aging process though the thickness of the FSP plate.

4. Neutron diffraction was used to investigate the texture variations in the FSP aluminum alloy plates. Two FSP specimens were prepared with a purpose of separating the effects of frictional heating and severe plastic deformation on the texture changes of the as-received rolled and recrystallized 6061-T6 aluminum-alloy plates. The results of the ODFs show that the base material has the strong cube or mixed cube and Goss texture, which is known as a typical recrystallized rolling texture of Al alloy plates. On the other hand, the ODF of the recrystallized region shows the shear texture in the FSP.

Comparison of the pole figures of the two cases shows that the variations of the preferred orientation are significant near the centerline in *Case 1*, which experienced severe plastic deformation. On the other hand, *Case 2* shows little texture variations across the centerline. The profiles of the reduced intensities reveal the quantitative texture variations at various positions across the centerline and through the thickness of the bulk FSP plates non-destructively. In *Case 1*, the number of the unit cells with the (200) plane normal parallel to the normal direction of the plate (i.e., reduced intensity along the through-thickness direction) was significantly decreased near the centerline, while the number of the unit cells with the (111) plane normal parallel to the normal direction of the plate was increased. On the other hand, *Case 2* does not show significant variations in

the reduced intensities. The current results from both pole-figure and reduced-intensity measurements clearly show that the severe plastic deformation from the stirring pin affects the preferred orientation during the FSP, while heating alone from the tool shoulder has little effects.

5. Finally, *hkl* specific diffraction peak intensities were measured using spatially-resolved neutron-diffraction technique to investigate the texture changes across the processing line in the FSP AZ-31B magnesium-alloy plate. The results showed that the texture variations are significant between the transition region and stir zone of the plate. The tensile behavior of the longitudinal specimen including mainly the stir zone shows significant increase in elongation and decrease in tensile strength compared to the base material. The correlation between the texture and tensile test results suggests that the drastic texture variation during the FSP significantly affects tensile behavior of the FSP Mg alloy plate. The incompatible boundary between the transition region and stir zone of FSP causes a fracture in the anisotropic hcp magnesium alloy.

References

[1] Thomas WM, Nicholas ED, Needham JC, Murch MG, Templesmith P, Dawes CJ. GB Patent Application No. 9125978.8; Dec 1991.

[2] Maddox SJ. Inter. J. Fat. 2003;25:1357.

[3] Mahoney MW, Rhodes CG, Flintoff JG, Spurling RA, Bingle WH. Mater Trans A 1998;29A;1955.

[4] Liu G, Murr LE, Niou CS, Mcclure JC, Vega FR. Scripta Mater 1997;37:355.

[5] Thomas WM, Nicholas ED. Mater Design 1997;18;269.

[6] Reynolds AP, Tang W, Posada M. J Sci Tech Weld Join 2003;8:455.

[7] Mishra RS, Mahoney MW, McFadden SX, Mara NA, Mukherjee AK. Scripta Mater 2000;42;163.

[8] Berbon PB, Bingel WH, Mishra RS, Bampton CC, Mahoney MW. Scripta Mater 2001;44;61.

[9] Ma ZY, Mishra RS, Mahoney MW, Acta Materialia, 2002;50;4419.

[10] Wert JA. Scripta Materialia 2003;49:607.

[11] Salem HG a, Reynolds AP, Lyons JS. Scripta Materialia 2002;46:337.

[12] Su JQ, Nelson TW, Sterling CJ. J Mater Res, 2003;18;1757.

[13] Su JQ, Nelson TW, Sterling CJ. Scripta Mater 2005;52;135.

[14] Valiev RZ, Islamgaliev RK, Alexandrov IV. Prog Matel Sci 2000;45;103.

[15] Windsor CG, Pulsed Neutron Scattering, Taylor and Francis, London;1981.

[16] Stone HJ, Withers PJ, Holden TM, Roberts SM, Reed RC. Metall Mater Trans A 1999;30;1797.

[17] Bourke MAM, Dunand DC, Ustundag E. Appl Phys A 2002;74;S1707.

[18] Wang X-L, Hoffman CM, Heueh CH, Sarma G, Hubbard CR, Keiser JR. Appl Phys Lett 1999;75;3294.

[19] Choo H, Bourke MAM, Daymond MR. Composites Sci Tech 2001;61;1757.

[20] Pang JWL, Holden TM, Mason TE. Acta Mater 1998;46;1503.

[21] Oliver EC, Mori T, Daymond MR, Withers PJ. Acta Mater. 2003;51;6453.

[22] Albertini G, Bruno G, Dunn BD, Fiori F, Reimers W, Wright JS. Mat Sci Eng 1997;A224;157.

[23] Albertini G, Bruno G, Carrado A, Fiori F, Rogante M, Rustichelli F. Meas Sci Technol 1999;10;R56.

[24] Carr DG, Ripley MI, Holden TM, Brown DW, Vogel SC. Acta Mater 2004;52;4083.

[25] Thomas WM, Johnson, K, Wiesner C. Adv Eng Mat 2003;5:485.

[26] Bussu. G, Irving PE, Inter. J Fatigue 2003;25;77.

[27] Webster PJ, Hughes DJ, Mills G, Preston RV, Shercliff HR, Withers PJ. Appl Phys 2002;A 74:S1421.

[28] Daymond MR, Bonner NW. Physica 2003;B325:130.

[29] Behnken H, Hauk V. Mater Sci Eng 2000;A289:60.

[30] Owen RA, Preston RV, Withers PJ, Shercliff HR, Webster PJ. Mat. Sci. & Eng. 2003;A346:159

[31] Webster GA, Ezeilo AN. Inter J Fat 2001;23:S375.

[32] Webster PJ, Oosterkamp LD, Browne PA, Hughes DJ, Kang WP, Withers PJ, Vaughan GBM. J strain analysis 2001;36:61.

[33] Staron P, Koçak M, Williams S. Appl Phys 2002;A 74:S1161.

[34] Reynolds AP, Tang W, Gnaupel-Herold T, Prask H. Scripta Mater. 2003;48;1289.

[35] Genevois C, Deschamps A, Denquin A, Doisneau-cottignies B. Acta Materialia 2005;53;2447.

[36] Nelson TW, Steel RJ, Arbegast WJ. Sci Tech Weld Joining 2003;8;283.

[37] Jata KV, Semiatin SL. Scripta Mater.2000;43:743.

[38] Krishnan KN. Materials Science and Engineering 2002;A327:246.

[39] Hassan KAA, Norman AF, Price DA, Prangnell PB. Acta Materialia 2003;51:1923.

[40] Murr LE, Liu G, Mcclure JC. Journal of Materials Science Letters 1997;16:1801.

[41] Sato YS, Yamashita F, Sugiura Y, Park SHC, Kokawa H. Scripta Mater 2004;50:365.

[42] Sato YS, Kokawa H, Enomoto M, Jogan S. Metall Mater Trans A 1999;30;2429.

[43] Sato YS, Kokawa H, Enomoto M, Jogan S, Hasimoto T. Metall Mater Trans A 1999;30;3125.

[44] Charit I, Mishra RS, Mahoney MW. Scripta Materialia 2002;47:631.

[45] Sutton MA, Reynolds AP, Yang B, Taylor B. Materials Science and Engineering 2003;A354:6.

[46] Fonda RW, Bingert JF, Colligan KJ. Scripta Mat 2004;51;243.

[47] Fonda RW, Bingert JF. Metal Mater Trans A 2004;35A;1487.

[48] Sato YS, Kokawa H, Ikeda K, Enomoto M, Jogan S, Hashimoto T. Metal Mater Trans A 2001;32A;941.

[49] Field DP, Nelson TW, Hovanski Y, Jata K. Metal Mater Trans A 2001;32A;2869.

[50] Hirsch J, Nes E, Lücke K. Acta Metall 1984;35;427.

[51] Park SHC, Sato YS, Kokawa H. Metal Mater Trans A 2003;34A;987.

[52] Park SHC, Sato YS, Kokawa H. Scripta Mat 2003;49;161.

[53] Ulysse P. Inter J Machine Tools & Manufacture 2002;42:1549.

[54] Chen CM, Kovacevic R. Intern J Machine Tools & Manufacture 2003;43:1319.

[55] Guerra M, Schmidt C, McClure JC, Murr LE, Nunes AC. Mater Char 2003;49:95.

[56] Chao YJ, Qi X, Tang W. Transactions of the ASME 2003;125:138.

[57] Lockwood WD, Tomaz B, Reynolds AP. Mater Sci Eng 2002;A323:348.

[58] Song M, Kovacevic R. Proc. Instn Mech. Engrs Part. B, J. Eng Manufacture 2003;217:73.

[59] Schmidt H, Hattel J, Wert J. Modelling Simul Mater Sci Eng 2004;12;143.

[60] Shindo DJ, Rivera AR, Murr LE. J mat sci 2002;37:4999.

[61] James MN, Hattingh DG, Bradley GR. Inter J Fatigue 2003;25:1389.

[62] Woo W, Choo H, Brown DW, Feng Z, Liaw PK, David SA, Hubbard CR, Bourke MAM. Appl Phys Letters;2005;86;231902.

[63] Peel M, Steuwer A, Preuss M, Withers PJ. Acta Mater 2003;51;4791.

[64] Shigematsu I, Kwon YJ, Suzuki K, Imai T, Saito N. J Mater Sci Lett 2003;22:353.

[65] Lee WB, Jung SB. Mater Lett 2004;58:1041.

[66] Krishnan KN. J Mater Sci 2002;37:473.

[67] Sutton MA, Reynolds AP, Wang DQ, Hubbard CR. J Eng Mater Tech 2002;124:215.

[68] Pao SP. Scripta Mate 2001;45:605.

[69] Rhodes CG, Mahoney MW, Bingel MH, Spurling RA, Bampton CC. Scrpta Mater 1997;36:69.

[70] Li Y, Murr LE, McClure JC. Scripta Mater, 1999;40:1041.

[71] Corral J, Trillo EA, Li Y, Murr LE. J Mater Sci Lett 2000;19:2117.

[72] Sutton MA, Reynolds AP, Yang B, Taylor R. Eng Frac Mech 2003;70:2215.

[73] Sutton MA, Reynolds AP, Yang B, Taylor B. Mater Sci Eng 2003;A354:6.

[74] Liu HJ, Fujii H, Maeda M, Nogi K. J Mater Sci lett 2003;22:441.

[75] Liu HJ, Fujii H, Maeda M, Nogi K. Sci Tech Weld Joining 2003;8:450.

[76] Sato YS, Kurihara Y, Park SHC, Kokawa H, Tsuji H. Scripta Mater 2004;50:57.

[77] Sanderson A, Punshon CS, Russell JD. Fusion Eng Design 2000;49:77.

[78] Thomas WM. Advanced Eng Mat 2003;5:485

[79] John R, Jata KV, Sadananda K. Inter J Fat 2003;25:939.

[80] Bussu G, Irving PE. Inter J Fat 2003;25:77.

[81] Albertini G, Bruno G, Fiori F, Girardin E, Giuliani A, Quadrini E. Physica B 2000;276:876.

[82] Ya M, Dai F, Lu J. J Pressure Vessel Tech 2003;125:201.

[83] Chao YJ, Wang Y, Miller KW. Weld Res Supp 2001;197s

[84] Song M, Kovacevic R. Inter J Machine Tools and Manufacture 2003;43:605.

[85] Larsen AC, Von Dreele RB. General Structure Analysis System, GSAS, LAUR 86-748. Los Alamos National Laboratory;2004.

[86] Masubuchi K, Analysis of Welded Structures, 1st ed. Pergamon, New York;1980

[87] Preston RV, Shercliff HR, Withers PJ, Smith S. Acta Mater. 2004;52;4973.

[88] Murr LE, Liu G, Mcclure JC. J Mater Sci 1998;33;1243.

[89] Edwards G, Stiller K, Dunlop GL, Couper MJ, Acta Mater 1998;46;3893.

[90] Esmaelil S, Lloyd DJ, Poole WJ. Acta Mater 2003;51;3467.

[91] Mrówka-Nowotnik G, Sieniawski J. J Mater Proc Tech 2005;162;367.

[92] Humphreys FJ, Hatherly M. Recrystallization and related annealing phenomena, Oxford, Elsevier Science;1995.

[93] Frigaard Ø, Grong Ø, Midling O.T, Metall Mater Trans A 2001;32;1797.

[94] Wenk HR, Lutterotti L, Vogel SC. Nuc Instrum Meth A 2003;515:575.

[95] Vogel SC, Hartig C, Lutterotti L, Von Dreele RB, Wenk HR, Williams DJ. Powder Diff 2004;19(1);65.

[96] Rietveld HM. Acta Cryst 1967;22;151.

[97] McCusker LB, Von Dreele RB, Cox DE, Louër D, Scardie P. J Appl Cryst, 1999;32;36.

[98] Kocks UF, Tomé CN, Wenk HR. Texture and anisotropy, Cambridge, U.K., Cambridge University Press;1998.

[99] Kocks UF, Kallend JS, Wenk H-R, Rollett AD, Wright SI. Preperred Orientation Package, popLA, Los Alamos National Laboratory;1995.

[100] Seidel TU, Reynolds AP. Metal Mater Trans A 2001;32;2879.

[101] Esparza JA, Davis WC, Trillo EA, Murr LE. J Mater Sci Lett 2002;21:917.

[102] Zhang D, Suzuki M, Maruyama K. Scripta Mater 2005;52;899.

[103] Sato YS, Park SHC, Matusunaga A, Honda A, Kokawa H. J Mat Sci 2005;40;637.

[104] Lee WB, Kim JW, Yeon YM, Jung SB. Mater Trans 2004;44:917.

[105] Chang CI, Lee CJ, Huang JC. Scripta Mater 2004;51;509.

[106] ASM Speciality Handbook. (1999). Magnesium and Magnesium Alloys. Materials Park, Ohio: ASM international.

[107] Agnew SR, Tomé CN, Brown DW, Holden TM, Vogel SC. Scripta Mater;2003;48;1003.

[108] Mukai T, Yamanoi M, Watanabe H, Higashi K. Scripta Mater 2001;45;89.

[109] Agnew SR, Horton JA, Lillo TM, Brown DW. Scripta Mater;2004;50;377.

[110] Lin HK, Huang JC, Langdon TG, Mat Sci Eng A 2005;402;250.

[111] Watanabe H, Takara A, Somekawa H, Mukai T, Higashi K. Scripta Mater;2005;52;449.

[112] Woo W, Choo H, Brown DW, Feng Z, Liaw P. K. Scripta Mater 2006;54;1859.

Vita

Wanchuck Woo was born in Busan, South Korea in 1970 and received the B.S. degree in Metallurgical Engineering in 1994 and the M.S. degree in Materials Science and Engineering in 1996 both from Korea University, Seoul, South Korea. His undergraduate work focused on design, synthesis, and processing of alloys using powder metallurgy and his graduate study for M.S. focused on the characterization of microstructure and nucleation behaviors in Sn-Bi alloy. From 1996, he worked at the R&D Center, SAMSUNG Heavy Industries, Daejon, South Korea as a research engineer, who was in charge of the joining/welding/coating processing, the evaluation of mechanical properties, and materials development for constructive equipments and shipbuilding. In 2002, he was admitted to study as a Ph.D. student and took the course work in the Department of Industrial, Welding, and System Engineering at the Ohio State University, Columbus, Ohio. In 2003, he transferred to Dr. Hahn Choo's research group at the University of Tennessee in pursuit of a Ph.D. in Materials Science & Engineering. From 2004, he collaborated with scientists in the Diffraction Group and Joining Research Group at the Oak Ridge National Laboratory as a graduate research assistant (supervisors at ORNL: Dr. Camden R. Hubbard and Dr. Stan A. David). During his Ph. D. program, he published (including accepted/in-press articles) nine journal/referred-proceeding papers and presented seven times at international conferences. He is a member of the Minerals, Metals & Materials Society, American Welding Society, and Materials Research Society.